Quadrotor Collision Dynamics and Fuzzy Logic Characterization

Fiona Chui

Master of Engineering

Mechanical Engineering

McGill University

Montreal,Quebec

December 2016

A thesis submitted to McGill University in partial fulfilment of the requirements of the degree of Master of Engineering

DEDICATION

For my family and friends.

And caffeine.

Who have all supported me throughout the years.

ACKNOWLEDGEMENTS

Foremost, I would like to thank my supervisor Dr. Inna Sharf for all her support and guidance throughout my tenure at McGill University. The opportunities and experiences she has provided me were exciting, interesting, and will always be invaluable to me.

Also foremost, I would like to thank my 'dynamics duo' Gareth Dicker, without whom this work would not be complete. His work developing the Navi custom quadrotor and piloting skills made the experimental validations in this thesis possible. Our collaboration has shaped a new direction for quadrotor recovery control, and will be missed.

I also wish to thank my fellow members of the Aerospace Mechatronics Laboratory for their help in realizing this thesis, and for their companionship. Special thanks go to Sebastian Schell for integrating Navi's electrical system, Linus Lehnert for designing Navi's bumpers, Thomas Fuehrer for his help with experimental tests, and Adrian Battiston for his state estimation expertise. The knowledge of Waqas Khan, Khoi Tran, Adam Harmat, Mingfeng Zhang, Patrick Abouzakhm, and Pierre-Yves Brèves have increased my understanding of the robotics world. Thanks are also given to Luc Sagnières, Josh Levin, Eitan Bulka, and Bassam Ul Haq for distracting me from my research.

Special thanks are given to Michael Coté and Justine Gagnepain for proofreading the French abstract.

Funding for this research was provided by the National Sciences and Engineering Research Council (NSERC) and the NSERC Canadian Field Robotics Network (NCFRN).

ABSTRACT

As quadrotor unmanned aerial vehicles (UAVs) become more commonplace, the inherent safety risks that these vehicles pose must be addressed. Focus is placed on the risk of losing flight control after a quadrotor UAV collides with an obstacle, which is a danger for anyone in proximity of the vehicle. A collision dynamics model of a quadrotor UAV with bumpers (i.e., propeller protection) is developed for the purpose of developing a collision recovery strategy to return the quadrotor to a hovering configuration after colliding with a wall, using only on-board sensors. The model includes forces and moments from the standard quadrotor rigid-body dynamics formulation, combined with contact forces applied at contact points on the bumpers. The model is simulated under an array of different incoming impact velocities and attitudes for model verification and studying the quadrotor post-collision response. Validation is provided by comparing the simulated post-collision response to experimental results with the same pre-impact conditions, to show the model is a suitable tool for collision recovery development. An overall recovery strategy is presented: the Collision Recovery Pipeline (CRP), comprising of three phases. The first two phases, Collision Identification and Collision Characterization, are formulated. The first phase detects the collision and estimates the contact surface normal direction with accelerometer measurements. The second phase uses a fuzzy logic process (FLP) to identify the difficulty of recovery. Monte Carlo simulation and experimental data demonstrate that the two phases provide useful information to the final CRP phase. Simulations and experiments of the complete recovery solution demonstrate successful quadrotor recovery for initial collision velocities up to 3 m/s, and the effect of the first two phases on the recovery control performance.

RÉSUMÉ

À mesure que les quadrirotors, petits véhicules aériens sans pilote (UAV), deviennent de plus en plus courants, les risques de sécurité inhérents à ces véhicules doivent être résolus. L'accent est mis sur le risque de perdre le contrôle du vol après qu'un quadrirotor soit entré en collision avec un obstacle, ce qui est un danger pour les personnes qui se retrouvent à proximité du véhicule. Un modèle de collision dynamique de quadrirotor avec des pare-chocs a été développé afin de développer une stratégie de récupération de collision. Avec des capteurs embarqués, cette stratégie permet de ramener le quadrirotor à une configuration de vol stationnaire après être entré en collision avec un mur. Le modèle tient compte des forces et des moments qui proviennent de la formulation dynamique du corps rigide standard d'un quadrirotor, combinés aux forces de contact appliquées aux points de contact sur les pare-chocs. Le modèle est simulé sous une multitude de vitesses et d'attitudes d'impacts différents. Cela permet la vérification du modèle ainsi que l'étude de la réponse de collision du quadrirotor. La validation est faite en comparant la réponse de collision simulée aux résultats expérimentaux avec les mêmes conditions de collision. On peut ainsi démontrer que le modèle est un outil approprié pour le développement d'une stratégie de récupération des collisions. Une stratégie globale de rétablissement est présentée : le pipeline de récupération de collision (CRP), qui compte trois phases. La première phase détecte la collision et estime la direction de la normale de la surface de contact grâce aux mesures de l'accéléromètre. La deuxième phase utilise un processus de logique floue (FLP) pour identifier la difficulté de la récupération. La simulation Monte Carlo et les données expérimentales démontrent que les deux phases fournissent des informations utiles à la dernière phase du CRP. Des simulations et des essais de la solution de récupération complète démontrent des récupérations réussies pour des collisions du quadrirotor avec des vitesses allant jusqu'à 3 m/s ainsi que l'effet des deux premières phases sur la performance du contrôle de récupération.

TABLE OF CONTENTS

LIST OF TABLES

LIST OF FIGURES

CHAPTER 1
Introduction

1.1 Background and Motivation

The past few years have seen a rapid increase in the use of quadrotor unmanned aerial vehicles (UAVs) for consumer, commercial, and military applications. The global consumer market alone has risen from 630 000 units to 4 300 000 units sold between 2013 and 2015 [1]. Numerous industries have taken advantage of these highly maneuverable UAVs, with broad commercial applications such as aerial photography, infrastructure inspection, aerial surveying and mapping, and disaster response [1]. These applications can all require the quadrotor to fly in close proximity to solid, stationary obstacles such as buildings, windows, and poles. In these environments, mid-air collisions with a stationary surface are a common hazard whether flying the quadrotor indoors or outdoors, piloted manually or autonomously. Example situations include a pilot losing perspective of distance between the quadrotor and an obstacle during manual flight control, flying in a disaster reconnaissance environment with unpredictable debris and rubble, and using a GPS-based position controller that is unaware of the obstacle.

Collisions between quadrotors and solid obstacles pose a critical safety concern: if the quadrotor is destabilized by the collision and loses flight control, it will 'drop out of the sky', and be a danger to anyone below it. While there has been substantial research focused on UAV obstacle avoidance, and purposeful interactions between UAVs and the environment, there has been little study on inevitable, unplanned contact with obstacles, or regaining flight control after a destabilizing collision. The ability to regain stable control after a collision would increase safety for humans in the vicinity of the thousands of currently active units.

More recent designs of quadrotor platforms have emerged which incorporate bumpers (otherwise known as ribbons, shrouds, airframes, or protective frames) that protect humans from the spinning propellers. Examples of such platforms include the Parrot AR Drone 2.0, the UDI U818A, and Spiri from Pleiades Robotics Inc., seen in Figures 1–1 and 1–2b. In the event of a collision, these bumpers also protect the fragile propellers, but do not prevent loss of flight control.

(a) Parrot AR Drone 2.0 (b) UDI U818A

Figure 1–1: Consumer drones with bumpers [2, 3].

Recent work in quadrotor aerobatics under external motion tracking [4, 5] and automatic recovery from arbitrary initial conditions using only on-board sensing [6] show promise for the development of collision recovery control in general. Although the quadrotor maneuvers in these works occur in unconstrained space, they nevertheless provide a good starting point for the aerobatic maneuvers needed for collision recovery control.

The availability of platforms that can protect the quadrotor propellers, which are vital to maintain vehicle flightworthiness, combined with experimentally validated aerobatic controllers, provide the necessary building blocks to address the safety concern caused by collisions between quadrotors and obstacles. This research becomes increasingly relevant and crucial as aviation safety regulators begin to implement UAV-specific regulations (e.g., FAA Small Unmanned Aircraft Regulations (Part 107), EASA regulatory framework for the operation of drones) [7, 8], and investigate the danger of UAV collisions [9, 10]. A successful quadrotor collision recovery strategy would increase vehicle autonomy, human safety, and potentially lead to greater acceptance of UAVs among government regulators.

1.2 Literature Review

This thesis incorporates topics from several research areas, from which relevant literature has been selected and reviewed below. First, modelling and control of a quadrotor in free-flight are presented. Then, previous work on UAV interactions with the environment are summarized. The contact dynamics modelling necessary to augment the standard quadrotor model to allow for collisions is then reviewed. Finally, fuzzy logic, which is used for quadrotor collision characterization in this thesis, is presented.

1.2.1 Quadrotor Dynamics Modelling and Control

Quadrotor UAVs are under-actuated aircraft with four uni-directional rotors (also called thrusters) that make the vehicle motion non-holonomic [11]. The rotors spin two pairs of counter-rotating propellers, generating uni-directional thrusting forces. There are two standard quadrotor configurations: the '+' configuration and the 'x' configuration, differentiated by whether the body-fixed axes are aligned with, or bisecting the quadrotor arms (i.e., motor supports) respectively. In both configurations, the motors are positioned to be symmetrical about the vehicle's geometric centre. Usually the configuration selection is a matter of preference, but flying in the 'x' configuration does provide more rotational acceleration for less thrusting force, and is more stable [12], when purely rolling or pitching: four thrusters generate moments about the roll or pitch axes, as opposed to only two in the '+' configuration.

Many authors have modelled the non-linear dynamics of the two standard quadrotor configurations to varying degrees of accuracy, depending on the control application. The basic model consists of a Newton-Euler formulation of the equations of motion for a rigid body, with the moments and forces due to thrusts applied at the rotor locations. Additional dynamic effects in this model include the gyroscopic torque [11, 13], the ground effect [13], and blade flapping during translational flight [14]. The aerodynamic effect of airflow disruption from bumpers in close proximity to the propeller was found to be significant and resulted in yaw tracking inconsistencies, but was not modelled in [14].

At any time, only four degrees of freedom can be tracked on a quadrotor; commonly, the three position degrees of freedom and the quadrotor heading (a.k.a, yaw angle) are chosen to be tracked during normal flight [11, 13, 15]. A standard trajectory control loop has the high level trajectory controller feeding into a position (and heading) controller, which in turn provides control inputs to the low level attitude controller that outputs four rotor speeds. Since a vehicle tilt in any direction causes the thruster forces to have components pointing in that direction, any attitude command deviating from hover in turn commands accelerations in the horizontal plane [14]. PID-based position and attitude controllers have proven to be effective with external vision or GPS feedback [11, 14], and are used in commercial and open-source flightstacks (i.e., software for UAVs) such as the PX4 and ArduPilot [16, 17]. Other control approaches for free-flight include integral backstepping control [13], sliding mode control [18], geometric tracking control [15], and minimum snap trajectory generation combined with PD attitude control [4].

1.2.2 UAV Interactions with the Environment

Several works study and present controllers for purposeful interaction between UAVs and their environment, to be used in inspection applications. In [19, 20], a model and controller for a Ducted-Fan Miniature UAV (DFMAV) interacting with a fixed vertical surface are presented. The impact force at a specified point of contact on the body is modelled using the linear Kevin-Voigt model. The controller uses a hybrid automaton to manoeuvre the DFMAV from free-flight to dock with the wall at the contact point, slide along the wall, and undock to free-flight. The simulation is able to capture the undesired 'rebound' dynamics of the DFMAV that may occur when trying to dock from free-flight. Another hybrid automaton controller of note allows for a quadrotor with a wire airframe to perform docking and sliding manoeuvres on walls at specified contact points [21]. During its development, it was found that a contact point above the quadrotor's center of gravity will reduce external moments and the tendency for the quadrotor to flip during docking. The collision is also modelled using the Kevin-Voigt model, while the sliding motion resistance is modelled with viscous friction. In experiments, the collision was detected with force sensors at the docking points and the controller successfully minimized rebounds due to impact before entering the sliding mode.

External wrench estimation is used in [22] to control 'collision reflexes' of a quadrotor. The external force is estimated using accelerometer measurements and knowledge of the actual thruster forces. A model based observer of the rotational states uses gyroscope measurements to estimate the external moment. A collision is detected when the estimated external force magnitude reaches a threshold, after which one of three collision reflex strategies is engaged: 1) the trajectory stops at the current setpoint position, 2) a new position setpoint along the direction of the collision normal is prescribed, with its distance from the obstacle being proportional to the estimated external force, and 3) an 'energy dissipation reflex' is produced by impedance damping control. In experimental collisions between a quadrotor with an airframe, and a polystyrene block, the last collision reflex strategy provided the fastest and smoothest recovery response, with a successful recovery from an impact at 1.5 m/s and level attitude. The external wrench estimation data is also used to estimate the obstacle position to provide new map information for trajectory planning.

1.2.3 Contact Dynamics Modelling

The contact dynamics research field is mature, and there exists a rich body of knowledge in the fundamentals of contact mechanics and different contact models. A literature survey of contact dynamics modelling is provided in [23], with focus on discrete and continuous normal contact force formulations. The survey concludes that situations involving flexible bodies and multiple contacts and/or impacts are best modelled with a continuous formulation combined with an *implicit* contact force solution. The implicit solution requires discretizing the contact region, and therefore typically requires finite element analysis. The continuous formulation combined with an *explicit* solution to relate the normal contact force to generalized coordinates and their derivatives is still preferential over the discrete formulation for the given contact situation; the latter formulation assumes a contact is between two rigid bodies, is an instantaneous event, and generates an impulsive contact force. The most common explicit non-linear compliant formulation for normal contact force is the Hunt and Crossley model [24]. Different approximations for relating the coefficient of restitution e, to the damping coefficient λ, in the Hunt and Crossley model are reviewed and ranked by the coefficient of restitution errors they produce in [25]. The evaluation shows the Herbert and McWhannell model [26] has the highest accuracy of the studied models.

Another advantage of the continuous normal force approach is that it can be easily combined with any continuous friction model. Surveys of friction models, along with explanations of friction mechanics can be found in [27, 28, 29]. Static friction models include the classical models (i.e., Coulomb friction, viscous friction, and stiction) and the Karnopp model, while dynamic friction models include the LuGre model, the Bristle model, and the Reset Integrator model. Friction compensation methods for controlling machines with friction are also reviewed in [27, 28], while [29] moves on to propose an optimization-based parameter identification method to obtain friction force model parameters from experimental data.

The above normal and friction force modelling approaches have been used for simulation and control in many diverse applications. These include biomechanics [30, 31], automotive vehicles [32, 33], and robotics [34, 35]. Works reviewed in Section 1.2.2 also use contact dynamics models to capture interaction between the UAV and a wall at specified vehicle locations [19, 20, 21].

1.2.4 Fuzzy Logic Processes and Control

The fuzzy logic process (FLP) used in this thesis, and fuzzy logic control (FLC), are based on type-2 Mamdani fuzzy set theory [36, 37], an approach to analysing complex systems and decision processes. The FLP and FLC are differentiated in that the FLC directly outputs a control signal, while the FLP outputs a value that can be mapped to a control signal through additional processing. Their general methodologies are identical, and are presented in [38, 39, 40]. FLPs/FLCs are used when the system is ill defined, or availability of decision making information is restricted. Control rules are expressed linguistically, allowing for expert human knowledge to be captured by an automatic control strategy [38, 41]. Complex logic can easily be put into a FLP/FLC, providing robust control to system uncertainties [39]. These characteristics make using fuzzy logic a good first approach for characterizing quadrotor collisions, to provide intuitive and interpretable information for recovery control.

Since the introduction of fuzzy control research by Mamdani [37] in 1975, the use of fuzzy set theory for generating control inputs has been developed for many research and industrial applications. Engines, reactors, plant processes, and automobiles were all controlled with fuzzy logic from its introduction in 1965 until 1985 [41]. Modern applications include robotic manipulators [42], wheeled mobile robots [43], and quadrotor normal flight control [44, 45, 46].

1.3 Objectives

This thesis aims to make significant contributions toward successful quadrotor post-collision recovery using only on-board sensors, in order to eventually operate in 'out-of-the-lab' environments. A successful recovery will move the quadrotor to a safe distance away from the obstacle in a stable orientation. Given this is a first attempt at a recovery strategy, the problem is simplified to assume the collision:

1. occurs indoors, with no wind disturbance.

2. is between a propeller-protected quadrotor and a flat vertical wall, a surface which serves as a good representation of many indoor and outdoor collision hazards, and also allows for experimentally reproducible testing and validation in the lab.
3. occurs in an environment that only consists of one wall and open space, such that the quadrotor has at least a 3.5 m $\times$ 3.5 m horizontal area to regain flight control, and the height allowed for recovery is only constrained by the collision height.
4. is 'non-destructive', in that operation of the vehicle is not compromised, and all four thrusters remain functional.

Even though assumption 3 gives the quadrotor a sizeable recovery area, this area is still constrained to exclude any space beyond the wall. Since quadrotor motion is non-holonomic, the wall constraint poses a challenge to recovery control, especially in situations where the quadrotor is flipped into a nearly vertical orientation as a result of impact, with the thrusters directed into the wall: under standard free-flight control, the quadrotor would be able to re-orient itself to an upright configuration only by moving in the direction of the wall. Without the ability to re-orient itself, the quadrotor can only generate thrust to continue forcing itself into the wall.

Toward the ultimate goal of recovery control, a simulator incorporating contact dynamics into the quadrotor rigid-body dynamics model must first be developed as a tool for developing and validating collision recovery. Direct development on a live platform would be dangerous, and accrue many costs due to quadrotor damage. This simulator must be validated, to ensure it is indeed an accurate tool. An overall recovery strategy will then be generated, to address the scope of collisions between those that are trivial to recover from, and those that damage the quadrotor (see assumption 4 above). The overall strategy is composed of three phases: Collision Identification, Collision Characterization, and Re-orientation Control. The first two phases provide information to the final phase, and are addressed in this thesis. The third phase is the focus of the M.Eng. thesis concurrently submitted by Mr. Gareth Dicker [47].

Both the contact dynamics model and the three recovery control phases developed are to be validated with experimental testing. The quadrotor platforms used for these experiments are Spiri by Pleiades Robotics Inc., and Navi — a custom built platform sharing Spiri's frame. Both quadrotors have 3-D printed bumpers to provide propeller protection, and are shown in Figure 1–2.

(a) (b)

Figure 1–2: (a) Navi and (b) Spiri [48] experimental quadrotors. In experiments, the Spiri platform propellers were identical to the white, 8 inch, 2 bladed propellers seen on Navi.

1.4 Thesis Outline

The thesis begins with Chapter 1, which introduces the background and motivation for this work, provides a review of relevant literature, and presents the thesis objectives. Chapter 2 formulates the contact dynamics model of a quadrotor with bumpers. This model is simulated and evaluated in Chapter 3 for a range of initial quadrotor collision conditions. Then, the model is validated with experimental testing in Chapter 4. Chapter 5 introduces the overall quadrotor collision recovery strategy, then formulates and verifies the Collision Identification and Collision Characterization phases of the overall strategy. The effect of these two phases on the overall strategy is also evaluated through simulation and experiment. Finally, Chapter 6 concludes the thesis and recommends future work to further advance quadrotor collision recovery.

CHAPTER 2
Contact Dynamics Model of Quadrotor with Bumpers

The quadrotor contact dynamics model captures the vehicle motion due to a 'collision' with the wall, where a collision is defined as a series of successive random contacts that occur between the protective bumpers and the wall. These contacts can be short and impulsive impacts, or continuous sliding interactions.

2.1 Quadrotor Model

A simplified quadrotor dynamics model is sufficient to accurately capture the vehicle's motion under normal flight conditions, and was therefore the basis of the quadrotor contact dynamics model presented here. This simplified model assumes that:

1. The quadrotor is a single rigid body. During collisions, the bumper deflections result in external forces and moments transmitted to the single rigid body.
2. The propellers are rigid.
3. All motors and propellers are identical.

The model's inertial frame $\mathcal{F}_I = \{\mathbf{e}_X \ \mathbf{e}_Y \ \mathbf{e}_Z\}$ is centred at an arbitrary position O_I, and follows the ENU (East, North, Up) convention. The body-fixed quadrotor frame $\mathcal{F}_Q = \{\mathbf{e}_x \ \mathbf{e}_y \ \mathbf{e}_z\}$ with origin O_Q centred at the vehicle center of mass (CM), is defined such that $\mathbf{e}_z$ points downwards from the vehicle body, following the standard convention used in aerospace literature. The standard 'x' quadrotor configuration was chosen over the '+' configuration to allow for more stable flight control. Consequently, $\mathbf{e}_x$ is defined as pointing outwards from the front, bisecting the front two quadrotor arms, and $\mathbf{e}_y$ is chosen to follow the right-hand rule as seen in Figure 2–1.

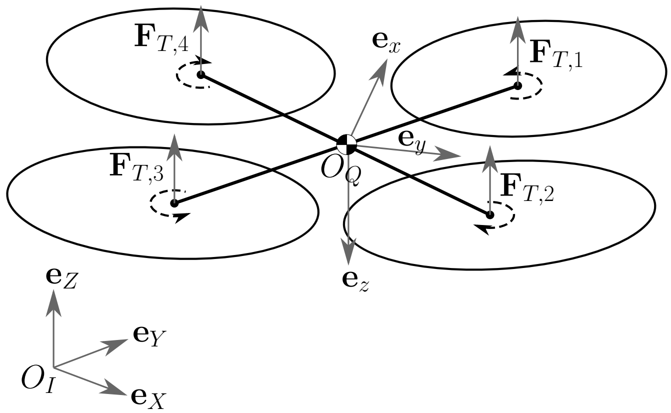

Figure 2–1: Dynamics model coordinate frames. Dashed arcs indicate propeller rotation direction. Note that the quadrotor CM is not necessarily coincident with the intersection of the quadrotor arms, as shown in this figure.

The quadrotor's translational (2.1) and rotational (2.2) dynamics are modelled using the Newton-Euler formulation for a single rigid body expressed in $\mathcal{F}_Q$:

$$m\dot{\mathbf{v}} + m\boldsymbol{\omega}^{\times}\mathbf{v} = \mathbf{F}_G + \mathbf{F}_T + \mathbf{F}_C \tag{2.1}$$

$$\mathbf{I}\dot{\boldsymbol{\omega}} = -\boldsymbol{\omega}^{\times}\mathbf{I}\boldsymbol{\omega} + \Big(\sum_{j=1}^{4}\mathbf{r}_{Tj}{}^{\times}\mathbf{F}_{Tj}\Big) + \mathbf{M}_T + \mathbf{M}_\Omega + \mathbf{M}_C \tag{2.2}$$

where $\mathbf{v} = [u\ v\ w]^T$ and $\boldsymbol{\omega} = [p\ q\ r]^T$ are the components of the absolute linear and angular velocities expressed in the body-fixed frame $\mathcal{F}_Q$. The platform specific parameters m, $\mathbf{I}$, and $\mathbf{r}_{Tj}$[1] are the mass, moment of inertia matrix about the CM, and relative position of the thruster locations to the CM respectively. The propeller/bumper index j prescribes the

[1] A subscripted $\mathbf{r}$ represents components of a relative position vector between two points, in the body-fixed frame. The points are specified by the subscript.

bumper locations: starboard front, starboard rear, port rear, and port front, respectively, as labelled in Figure 2–1. The cross product operator is denoted by $^\times$.

To complete the formulation, the pose kinematics are propagated with the quadrotor linear and angular velocities expressed in $\mathcal{F}_I$ as follows:

$$\dot{\mathbf{p}} = \mathbf{q} \odot \mathbf{v} \tag{2.3}$$

$$\dot{\mathbf{q}} = -\frac{1}{2} \begin{bmatrix} 0 \\ \\ \boldsymbol{\omega} \end{bmatrix} \otimes \mathbf{q} \tag{2.4}$$

where $\mathbf{p}$ represents the components of the absolute quadrotor CM position expressed in $\mathcal{F}_I$[2] , and the quaternion $\mathbf{q} = [q_w \ q_x \ q_y \ q_z]^T$ describes the quadrotor orientation relative to $\mathcal{F}_I$. A quaternion parametrization for quadrotor orientation was chosen because of the aerobatic nature of the collision response; collisions causing the vehicle to flip vertically against the wall would result in a singularity commonly known as 'gimbal lock' if Tait-Bryan Euler angles were used. Vector components are rotated from $\mathcal{F}_Q$ to $\mathcal{F}_I$ via the quaternion rotation operator $\odot$. The converse rotation from $\mathcal{F}_I$ to $\mathcal{F}_Q$ is represented by an inverse quaternion rotation (e.g., $\mathbf{v} = \mathbf{q}^{-1} \odot \dot{\mathbf{p}}$). The quaternion multiplication operator is denoted by $\otimes$.

The applied forces $\mathbf{F}$ and moments $\mathbf{M}$ in (2.1) and (2.2) have the subscripts G, T, Ω, and C to denote gravitational, thruster, gyroscopic, and contact respectively, and are defined in (2.5) to (2.8), with the exception of $\mathbf{F}_C$ and $\mathbf{M}_C$. These latter contact elements are derived in Section 2.2. The gravitational force is expressed as:

$$\mathbf{F}_G = \mathbf{q}^{-1} \odot m\mathbf{g} \tag{2.5}$$

[2] A subscripted $\mathbf{p}$ represents components of a position vector relative to the inertial frame. The point that is positioned by the subscripted $\mathbf{p}$ is specified by the subscript.

where $\mathbf{g} = [0\ 0\ -g]$ is the gravity vector in $\mathcal{F}_I$, and g is the acceleration due to gravity. The thruster force is expressed as:

$$\mathbf{F}_T = \sum_{j=1}^{4} \mathbf{F}_{Tj} = \sum_{j=1}^{4} \begin{bmatrix} 0 \\ 0 \\ -k_t \Omega_j^2 \end{bmatrix} \tag{2.6}$$

where k_t is the propeller lumped thrust coefficient that relates the square of the propeller angular speed Ω_j to the force generated by the propeller j. The term $\left(\sum_{j=1}^{4} \mathbf{r}_{Tj} \times \mathbf{F}_{Tj}\right)$ is the moment caused by the individual thruster forces $\mathbf{F}_{Tj}$ not applied at the CM, but at the thruster locations instead. The thruster moment is expressed as:

$$\mathbf{M}_T = \begin{bmatrix} 0 \\ 0 \\ k_d \sum_{j=1}^{4} (-1)^j \Omega_j^2 - J_r \sum_{j=1}^{4} (-1)^j \dot{\Omega}_j \end{bmatrix} \tag{2.7}$$

where k_d is the lumped drag torque coefficient relating Ω_j to the drag torque generated by the rotation of propeller j. A moment due to the propeller's angular momentum is also present, making use of the propeller moment of inertia about its rotational axis J_r. The gyroscopic moment is expressed as:

$$\mathbf{M}_\Omega = \begin{bmatrix} -qJ_r \sum_{j=1}^{4} (-1)^j \Omega_j \\ pJ_r \sum_{j=1}^{4} (-1)^j \Omega_j \\ 0 \end{bmatrix} \tag{2.8}$$

The $(-1)^j$ elements present in the moment expressions (2.7) and (2.8) account for the rotation direction of the counter-rotating propeller pairs. In particular, these elements dictate that propeller pair $1, 3$ generate thrust when rotating counter-clockwise when viewed from above, while pair $2, 4$ rotate clockwise to generate thrust. To have the pairs rotate in opposite directions to generate thrust, these elements would be replaced by $(-1)^{j+1}$.

It should be noted that forces and moments due to aerodynamic drag are not modelled, as these components are insignificant indoors, where wind is absent from the flying environment. The gyroscopic moment (2.8) and angular momentum rate term in (2.7) are included, even though they are omitted in many dynamic models in literature. Their effects are cancelled by the counter-rotating propeller pairs when the quadrotor heading is stable [14] and near equilibrium hover conditions. However, since the collision response is aerobatic in nature, these conditions are not met, making it important for these propeller-induced terms to be retained in the model.

2.2 Contact Model

The force and moment on a single bumper during a contact result from the normal force and friction force applied at the contact point, as determined by the contact geometry. Sections 2.2.1 to 2.2.3 formulate the contact components for a single bumper, and the full quadrotor contact model with four bumpers is assembled from these in Section 2.2.4.

The contacts occur between the quadrotor and a vertical wall, which spans $\{\mathbf{e}_Z,\ \mathbf{e}_T\}$, shown in Figure 2–2. The wall tangent vector $\mathbf{e}_T$ is defined as:

$$\mathbf{e}_T = \mathbf{e}_Z{}^{\times}\mathbf{e}_N \tag{2.9}$$

where $\mathbf{e}_N$ is the unit vector normal to the wall, pointing outwards towards the unconstrained open space.

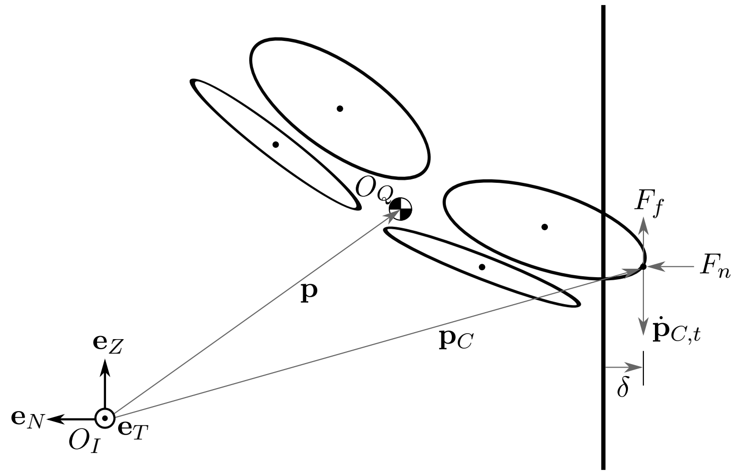

Figure 2–2: Contact force elements for example contact scenario at a bumper

2.2.1 Normal Contact Force Model

The normal contact force F_n is applied at the contact point $\mathbf{p}_C$, in the direction of $\mathbf{e}_N$. A compliant model for F_n was chosen over a discrete model because the contact scenario involves a flexible and deformable, as opposed to rigid, bumper. Also, to allow modelling of continuous contact between the quadrotor and the wall, including at high impact speeds, the non-linear compliant model first introduced by Hunt and Crossley [24] is used to explicitly model F_n:

$$F_n = \lambda \delta^n \dot{\delta} + k\delta^n \tag{2.10}$$

where δ is the local deformation (penetration) at $\mathbf{p}_C$, k is a constant stiffness coefficient, λ is a damping coefficient, and n is dependent on the contact scenario. Elements of the normal contact force model (2.10) with physical interpretation are shown in Figure 2–2. The relationship between λ and the coefficient of restitution e is approximated by the Herbert and McWhannell model because of its accuracy over other approximations [25, 26]. This relationship is:

$$\lambda = \frac{6(1-e)}{[(2e-1)^2+3]}\frac{k}{v_i} \tag{2.11}$$

where v_i is the initial contact velocity of $\mathbf{p}_C$ in the $\mathbf{e}_N$ direction, that is $\dot{\delta}$ at the beginning of the contact. The normal contact variables δ and $\dot{\delta}$ are made available from the contact geometry, and will be derived in Section 2.2.3.

2.2.2 Friction Force Model

The friction force F_f is also applied at $\mathbf{p}_C$, in the direction opposite $\dot{\mathbf{p}}_{C,t}$, which is the velocity of $\mathbf{p}_C$ tangent to the wall, as shown in Figure 2–2. This tangent velocity is computed as:

$$\dot{\mathbf{p}}_{C,t} = (\dot{\mathbf{p}}_C{}^T \mathbf{e}_T)\mathbf{e}_T + (\dot{\mathbf{p}}_C{}^T \mathbf{e}_Z)\mathbf{e}_Z \tag{2.12}$$

Then, F_f is modelled with the regularized Coulomb friction model:

$$F_f = \mu F_n \tag{2.13}$$

with the coefficient of friction μ defined as:

$$\mu = \begin{cases} \frac{\mu_C}{v_{th}}||\dot{\mathbf{p}}_{C,t}|| & \text{, if } ||\dot{\mathbf{p}}_{C,t}|| \leq v_{th} \\ \mu_C & \text{, otherwise} \end{cases} \tag{2.14}$$

where μ_C is a constant Coulomb friction coefficient for sliding, and v_{th} is the threshold velocity of $||\dot{\mathbf{p}}_{C,t}||$ past which μ remains constant. The value of v_{th} is non-zero and small, meaning this friction model requires a small amount of sliding to produce non-zero force. This model was chosen for its simplicity and more intuitive connection to actual physics over more complex models, while maintaining continuity at zero $\dot{\mathbf{p}}_{C,t}$.

2.2.3 Contact Geometry Model

The contact geometry is based on the 3-D printed bumpers of the two experimental platforms, which are similar in geometry and attachment configuration. The bumpers of both platforms are individually attached to the vehicle central body. On Navi, they are interconnected by carbon fibre rods to increase stiffness, as shown in Figure 2–3. Specifically, the contact geometry is a simplified representation of the bumpers' outside edges, which are most likely to contact the wall first in a collision; these edges are approximately circular and are tilted at a slight angle towards the body center. Accordingly, the contact geometry model is comprised of four circles[3] with a radius R_b, tilted at an angle τ towards the body center, and centred at known relative positions $\mathbf{r}_{Bj},\ j \in \{1,2,3,4\}$ to O_Q, or $\mathbf{p}_{Bj},\ j \in \{1,2,3,4\}$ in the inertial frame, as shown in Figure 2–3. For simplicity in the remaining contact geometry derivations for a single bumper below, the circle center of the bumper model is positioned at $\mathbf{r}_B$ and $\mathbf{p}_B$.

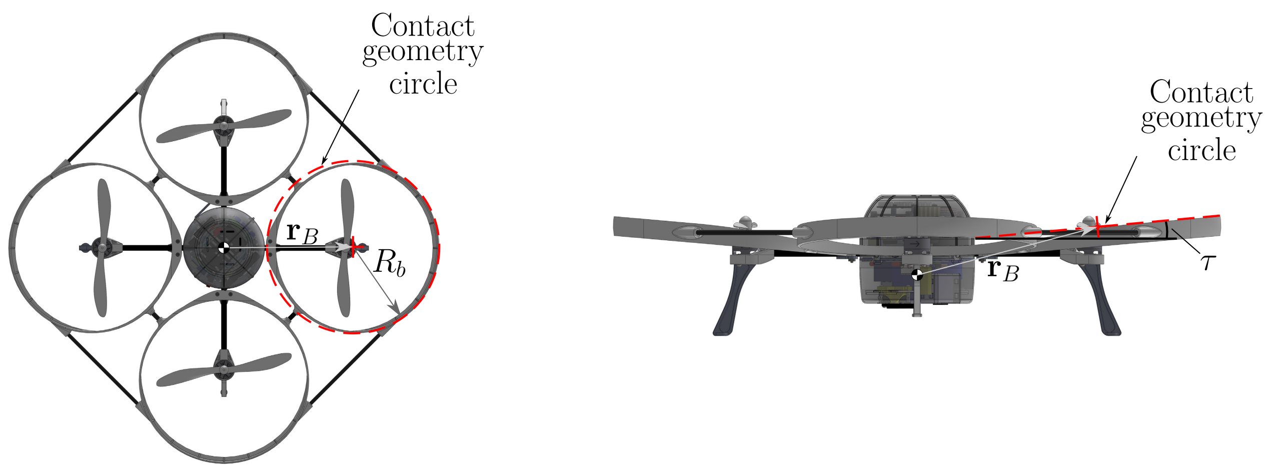

(a) Top view (b) Side view

Figure 2–3: Basis for contact geometry from Navi experimental platform

Equations (2.15) to (2.23) determine the point of contact $\mathbf{p}_C$ between a circle and a planar wall, from which the deflection δ and deflection rate $\dot{\delta}$ to complete the normal contact force model in (2.10) can be generated. Rigid body kinematics provide the point's velocity $\dot{\mathbf{p}}_C$ for the friction contact force direction in (2.12). Since δ is the local penetration *into* the

[3] The circular contact geometry, aside from representing the bumper geometry closely, would have to be used even in the absence of bumpers in order to detect collisions with a propeller, the tip of which traces a circular path.

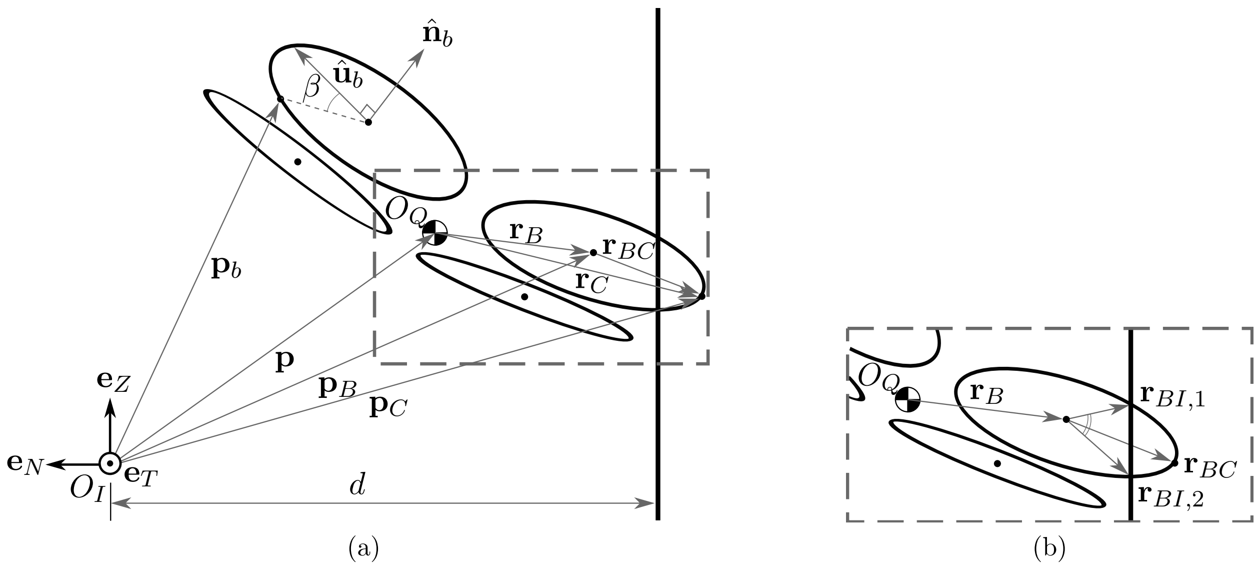

Figure 2–4: Contact geometry elements for example contact scenario at a bumper. The elements in (a) are pertinent to Equations (2.15) and (2.19) to (2.23), and the elements in (b) are pertinent to Equations (2.16) to (2.18). The dashed box encompasses the same region for the contact scenario in (a) and (b).

wall, the known direction $-\mathbf{e}_N$ is used in the derivations to generate components directed *into* the wall. Elements of the contact geometry derivations are shown in Figure 2–4. First, a generic point on the bumper circle is parametrized in $\mathcal{F}_I$ with the expression:

$$\mathbf{p}_b = R_b \cos\beta\ \hat{\mathbf{u}}_b + R_b \sin\beta\ \hat{\mathbf{n}}_b^{\times}\hat{\mathbf{u}}_b + \mathbf{p}_B \tag{2.15}$$

where $\hat{\mathbf{u}}_b$ and $\hat{\mathbf{n}}_b$ are the unit vectors tangent and normal to the circle plane respectively, and are derived using the bumper tilt angle τ in Figure 2–3. The generic bumper point $\mathbf{p}_b$ is parametrized by the angle β, which is the counter-clockwise angle from $\hat{\mathbf{u}}_b$ at which $\mathbf{p}_b$ is positioned, when viewed from above. Then, with a known wall location, the following equation is solved for β that parametrizes the points of intersection between the wall and the contact circle:

$$d = (R_b \cos\beta\ \hat{\mathbf{u}}_b + R_b \sin\beta\ \hat{\mathbf{n}}_b^{\times}\hat{\mathbf{u}}_b + \mathbf{p}_B)^T(-\mathbf{e}_N) \tag{2.16}$$

where d is the known distance in the $-\mathbf{e}_N$ direction the wall is located from O_I. Solutions of (2.16) that produce two real angles indicate a penetration, that is $\delta > 0$. These angles are then used in (2.15) to find the two points of intersection, positioned at $\mathbf{p}_{I,1}$ and $\mathbf{p}_{I,2}$. The relative positions of these points of intersection to the bumper center are then:

$$\mathbf{r}_{BI,i} = \mathbf{q}^{-1} \odot (\mathbf{p}_{I,i} - \mathbf{p}_B), \quad i \in \{1, 2\} \tag{2.17}$$

The vector $\mathbf{r}_{BC}$ bisects $\mathbf{r}_{BI,1}$ and $\mathbf{r}_{BI,2}$, has a magnitude R_b, and locates $\mathbf{p}_C$ relative to the bumper center. This vector is expressed as:

$$\mathbf{r}_{BC} = \pm R_b \frac{\mathbf{r}_{BI,1} + \mathbf{r}_{BI,2}}{||\mathbf{r}_{BI,1} + \mathbf{r}_{BI,2}||} \tag{2.18}$$

where the sign in (2.18) is negative if more than half the circle is enclosed by the wall, and positive otherwise.

With $\mathbf{r}_{BC}$, the position of the contact point $\mathbf{p}_C$, and the relative position of the contact point to O_Q, $\mathbf{r}_C$ can be expressed as:

$$\mathbf{p}_C = \mathbf{p}_B + \mathbf{q} \odot \mathbf{r}_{BC} \tag{2.19}$$

$$\mathbf{r}_C = \mathbf{q}^{-1} \odot (\mathbf{p}_C - \mathbf{p}) \tag{2.20}$$

Based on the known wall distance d along the $-\mathbf{e}_N$ direction, δ is simply the projection of $\mathbf{p}_C$ onto this direction into the wall, subtracted by d, as expressed below:

$$\delta = {\mathbf{p}_C}^T(-\mathbf{e}_N) - d \tag{2.21}$$

With rigid body kinematics, the contact point velocity in $\mathcal{F}_I$ is expressed as:

$$\dot{\mathbf{p}}_C = \mathbf{q} \odot (\mathbf{v} + \boldsymbol{\omega}^\times \mathbf{r}_C) \tag{2.22}$$

Finally, a projection of $\dot{\mathbf{p}}_C$ onto $-\mathbf{e}_N$ gives the penetration rate:

$$\dot{\delta} = \dot{\mathbf{p}}_C{}^T(-\mathbf{e}_N) \tag{2.23}$$

Thus, all the contact geometry elements needed to compute the normal and friction forces are available to complete the full contact model.

2.2.4 Full Contact Model

With the penetration distance and rate determined from the contact geometry, as per (2.21) and (2.23), Equation (2.10) provides the normal contact force F_n. The friction force direction is determined by (2.12), with the contact point velocity in (2.22). Equation (2.20) provides the contact location, which completes all the derivations necessary to find the force and moment due to contact on the quadrotor at bumper j in $\mathcal{F}_Q$:

$$\mathbf{F}_{Cj} = \mathbf{q}^{-1} \odot \left(F_n \mathbf{e}_N - F_f \frac{\dot{\mathbf{p}}_{C,t}}{||\dot{\mathbf{p}}_{C,t}||} \right), \qquad j \in \mathcal{P} \tag{2.24}$$

$$\mathbf{M}_{Cj} = \mathbf{r}_C{}^{\times} \mathbf{F}_{Cj}, \qquad j \in \mathcal{P} \tag{2.25}$$

where $\mathcal{P}$ is the set of bumpers participating in the collision at a particular instance of time. The sum of the forces and moments from the contacting bumpers in (2.24) and (2.25) comprise the total contact force and moment during a contact needed for the equations of motion in (2.1) and (2.2), that is:

$$\mathbf{F}_C = \sum_{j \in \mathcal{P}} \mathbf{F}_{Cj} \tag{2.26}$$

$$\mathbf{M}_C = \sum_{j \in \mathcal{P}} \mathbf{M}_{Cj} \tag{2.27}$$

Note that the contact geometry only allows for one contact point per bumper, so there can be a maximum of four and a minimum of zero contact points at any given time. The full contact model allows for a collision to be modelled via a series of contacts, determined by the quadrotor dynamic response to the external contact forces and moments, over time.

CHAPTER 3
Simulation of Collision Response

Through an investigation of the quadrotor response predicted by the contact dynamics model, as presented in Chapter 2, for a range of initial collision conditions, the model is verified and assessed. This is done by ensuring the quadrotor response agrees with intuition and can be explained in relation to the physical system, and by scrutinizing the trends observed from simulation. These trends are studied for the bumper deflection response, quadrotor post-collision angular velocity response, and general (visual description) response for the Navi quadrotor simulation. Results for the Spiri quadrotor are omitted in this chapter, as they do not add additional information or insight. Then, example scenarios are used to illustrate the full quadrotor collision response. Furthermore, the results of this chapter are used to gain 'expertise' for developing the collision characterization FLP in Section 5.3.

In the following, the position and incoming collision velocity of the vehicle refer to those of the quadrotor CM. For a more intuitive understanding of the results, the Tait-Bryan Euler angles $\{\phi, \theta, \psi\}$, denoting the roll, pitch, and yaw are presented to illustrate the orientation responses, instead of the quaternion parametrization they are derived from.

3.1 Simulation Setup

The dynamics model in Chapter 2 is simulated using *MATLAB*, with the position and attitude controllers running at 200 Hz, the same speed as the Navi on-board low level controller, and the equations of motion simulated with *ode45* at variable integration time steps ($>$ 200 Hz). To reduce the nonlinear multidimensional algebra in (2.16) to one dimension, the simulated wall spans the YZ plane, and is located at $d = 1.5$ m along the X axis, such that $\mathbf{e}_N = -\mathbf{e}_X$ and $\mathbf{e}_T = -\mathbf{e}_Y$.

3.1.1 Navi Quadrotor Parameters

The inertial, geometric, propeller, and contact parameters are provided in Table 3–1 for Navi. Table 3–2 lists the same parameters for the Spiri quadrotor, which will be used in Chapter 4. The inertial and geometric parameters were obtained from a detailed computer aided design (CAD) model of the Navi assembly. A CAD model of the two-bladed 8 inch propeller provided the propeller moment of inertia about its rotation axis J_r. The propeller thrust coefficient k_t to relate the thrusting force to the square of the propeller rotation speed was experimentally determined by using a force torque sensor to measure the thrusting force generated at different propeller rotation speeds, which were in turn measured with an optical encoder. Similarly, k_d was determined by measuring the moment about the rotation axis at different propeller rotation speeds.

The normal contact parameters k and n used in (2.10) were determined experimentally by measuring the bumper deflection under different static compressive loads at the point on the bumper's outside edge, farthest from its location of attachment to the body. Measurements were performed for a bumper assembled within the entire bumper structure: four bumpers attached with carbon fibre rods. The coefficient of restitution e for use in (2.11) was chosen to reflect a nearly elastic collision, which is reasonable given the flexibility of Navi's bumpers, and was set to be constant since variations in its value had negligible effect on the simulated response. Even though the normal contact parameters are likely to vary with incoming impact orientations and speeds [23], the values used here are reasonable for a first approach at capturing the contact mechanics.

The Coulomb friction coefficient for sliding μ_C used in (2.14) changes with different combinations of bumper material and wall surface (e.g., glass, cement, drywall), and is shown to have a significant impact on quadrotor response through simulations with no friction (i.e. $\mu_C = 0$) in Sections 3.2 to 3.4. However, given the in-the-lab experimental setup only has a painted drywall wall available as the collision surface, μ_C in simulations with friction are

Table 3–1: Navi Quadrotor Parameters

Inertial and Geometric Parameters			
m (kg)	1.10		
$\mathbf{I}$ (kg · m^2)	$\begin{bmatrix} 1.122 \times 10^{-2} & -5.62 \times 10^{-5} & -1.42 \times 10^{-8} \\ -5.62 \times 10^{-5} & 1.123 \times 10^{-2} & -4.50 \times 10^{-6} \\ -1.42 \times 10^{-8} & -4.50 \times 10^{-6} & 2.108 \times 10^{-2} \end{bmatrix}$		
$\mathbf{r}_{Tj}$ (m)	$\begin{array}{cccc} j=1 & j=2 & j=3 & j=4 \\ \begin{bmatrix} 0.1260 \\ 0.1261 \\ -0.0245 \end{bmatrix} & \begin{bmatrix} -0.1270 \\ 0.1261 \\ -0.0245 \end{bmatrix} & \begin{bmatrix} -0.1270 \\ -0.1271 \\ -0.0245 \end{bmatrix} & \begin{bmatrix} 0.1260 \\ -0.1271 \\ -0.0245 \end{bmatrix} \end{array}$		
Propeller Parameters			
k_t	8.70×10^{-8}	k_d	8.70×10^{-9}
J_r (kg · m^2)	2.21×10^{-5}		
Contact Force Parameters			
k (N/m)	372	μ_C	0.30
n	0.66	v_{th} (m/s)	1.00×10^{-4}
e	0.90		
Contact Geometry Parameters			
R_b (m)	0.125	τ (°)	5.00
$\mathbf{r}_{Bj}$ (m)	$\begin{array}{cccc} j=1 & j=2 & j=3 & j=4 \\ \begin{bmatrix} 0.1351 \\ 0.1351 \\ -0.0275 \end{bmatrix} & \begin{bmatrix} -0.1361 \\ 0.1351 \\ -0.0275 \end{bmatrix} & \begin{bmatrix} -0.1361 \\ -0.1361 \\ -0.0275 \end{bmatrix} & \begin{bmatrix} 0.1351 \\ -0.1361 \\ -0.0275 \end{bmatrix} \end{array}$		

Table 3–2: Spiri Quadrotor Parameters

Inertial and Geometric Parameters			
m (kg)	0.93		
$\mathbf{I}$ (kg · m^2)	$\begin{bmatrix} 8.737 \times 10^{-3} & -4.20 \times 10^{-7} & -5.29 \times 10^{-5} \\ -4.20 \times 10^{-7} & -8.988 \times 10^{-3} & -1.14 \times 10^{-6} \\ -5.29 \times 10^{-5} & -1.14 \times 10^{-6} & 1.714 \times 10^{-2} \end{bmatrix}$		
$\mathbf{r}_{Tj}$ (m)	$\begin{array}{cccc} j=1 & j=2 & j=3 & j=4 \\ \begin{bmatrix} 0.1319 \\ 0.1265 \\ -0.0242 \end{bmatrix} & \begin{bmatrix} -0.1212 \\ 0.1265 \\ -0.0242 \end{bmatrix} & \begin{bmatrix} -0.1212 \\ -0.1265 \\ -0.0242 \end{bmatrix} & \begin{bmatrix} 0.1319 \\ -0.1265 \\ -0.0242 \end{bmatrix} \end{array}$		
Propeller Parameters			
${k_t}^*$	8.70×10^{-8}	${k_d}^*$	8.70×10^{-9}
${J_r}^*$ (kg · m^2)	2.21×10^{-5}		
Contact Force Parameters			
k (N/m)	40.0	μ_C	0.16
n	0.54	v_{th}^* (m/s)	1.00×10^{-4}
e^*	0.90		
Contact Geometry Parameters			
R_b (m)	0.11	τ (°)	11.0
$\mathbf{r}_{Bj}$ (m)	$\mathbf{r}_{Tj},\ j \in \{1, 2, 3, 4\}$		

*Parameter is common among the two quadrotor configurations only dependent on Navi's bumpers, which are made of 3-D printed PLA. The value of μ_C was measured between a rectangular block of the corresponding bumper material and a stiff wood plank painted with wall paint. Lastly, the threshold velocity v_{th} used in (2.14) was chosen of the order used in other simulated friction models [29, 49, 50].

3.1.2 Quadrotor Control

Direction of the quadrotor into the wall at a specified angle and impact velocity is achieved by prescribing a desired attitude setpoint to the attitude controller, and specifying the initial position and velocity of the quadrotor. The attitude controller is based on a PID law for ϕ and θ, and a PI controller for the yaw rate r. A double-loop PID altitude controller [51] maintains the desired height at 2 m for the duration of the simulation.

The response of the quadrotor after the first impact with the wall is examined using a standard control strategy which simply continues using the pre-impact control law and reference inputs (i.e., desired attitude and altitude), and would represent a scenario where the vehicle is unaware of the collision, and therefore no recovery control is engaged.

3.1.3 Pre-Collision Kinematics

The quadrotor collision response is examined for a range of 'inclination' angles ζ from $-30°$ to $30°$, this angle measured between the projection of the body-fixed $-z$ axis onto the vertical plane normal to the wall, and the inertial Z axis. The angle is positive if the quadrotor is directed into the wall, and negative if directed away. For example, when $\psi = 0°$, ζ is simply the negative of pitch (i.e., $-\theta$). In the general case, ζ is expressed as:

$$\zeta = \mathrm{sign}(\zeta) \cdot \cos^{-1}\left(\frac{\left(\mathbf{e}_z^I - \left((\mathbf{e}_z^I)^T \mathbf{e}_T\right)\mathbf{e}_T\right)^T \mathbf{e}_Z}{\left|\left|\mathbf{e}_z^I - \left((\mathbf{e}_z^I)^T \mathbf{e}_T\right)\mathbf{e}_T\right|\right|} \right) \tag{3.1}$$

where $\mathbf{e}_T$ is defined in (2.9), and $\mathbf{e}_z^I$ is the body-fixed $-z$ axis rotated into the inertial frame:

$$\mathbf{e}_z^I = \mathbf{q} \odot (-\mathbf{e}_z) \tag{3.2}$$

Using the incoming collision ζ combines the parametrization of ϕ and θ into one value, with the added benefit of providing information on the quadrotor attitude *relative to the wall plane*.

The effect of ζ on the quadrotor collision response is examined for seven incoming collision velocities $\dot{X}_C$ ranging from 0.5 m/s to 2.50 m/s, for a two bumper initial impact ($\psi = 0°$) and a one bumper initial impact ($\psi = 45°$). The responses are simulated for the Navi quadrotor with friction ($\mu_C = 0.3$) and without friction ($\mu_C = 0$) in Sections 3.2 to 3.4.

3.2 Bumper Deflection Response

The maximum deflection during the initial contact δ_{init} is a good indicator of the contact model fidelity, as there exists a range of realistic deflections given the flexibility and radii of the quadrotor bumpers. The collisions for the $\psi = 0°$ case occur at bumpers 1 and 4 and δ_{init} is taken as the maximum deflection for the two bumpers.

Figure 3–1 shows higher deflections δ_{init} for increasing $\dot{X}_C$, as expected. Slightly lower δ_{init} are observed for the two bumper initial contact case ($\psi = 0°$) than the one bumper case ($\psi = 45°$)—also expected as there are two contact forces resisting deflection in the former case, as opposed to only one in the latter.

The peak deflection values occur consistently for all curves in Figure 3–1 at, or centred about $\sim 9°$, this inclination corresponding to the orientation where the contact point is horizontal with the quadrotor CM. Given the Navi quadrotor contact geometry, this situation occurs exactly when the inclination angle is 8.4° for $\psi = 0°$, and 9.2° for $\psi = 45°$. Contacts at these orientations will result in negligible total contact moment $\mathbf{M}_C$ applied to the vehicle, and hence, a more direct contact resulting in larger δ_{init}. When $\mathbf{M}_C$ is not negligible, the rotation of the quadrotor due to the contact moment decreases the bumper penetration in the $-\mathbf{e}_N$ direction, resulting in smaller δ_{init} values.

A comparison of the deflection curves with friction (Figures 3–1a and 3–1b) to those without friction (Figures 3–1c and 3–1d) shows that the presence of friction causes the peak

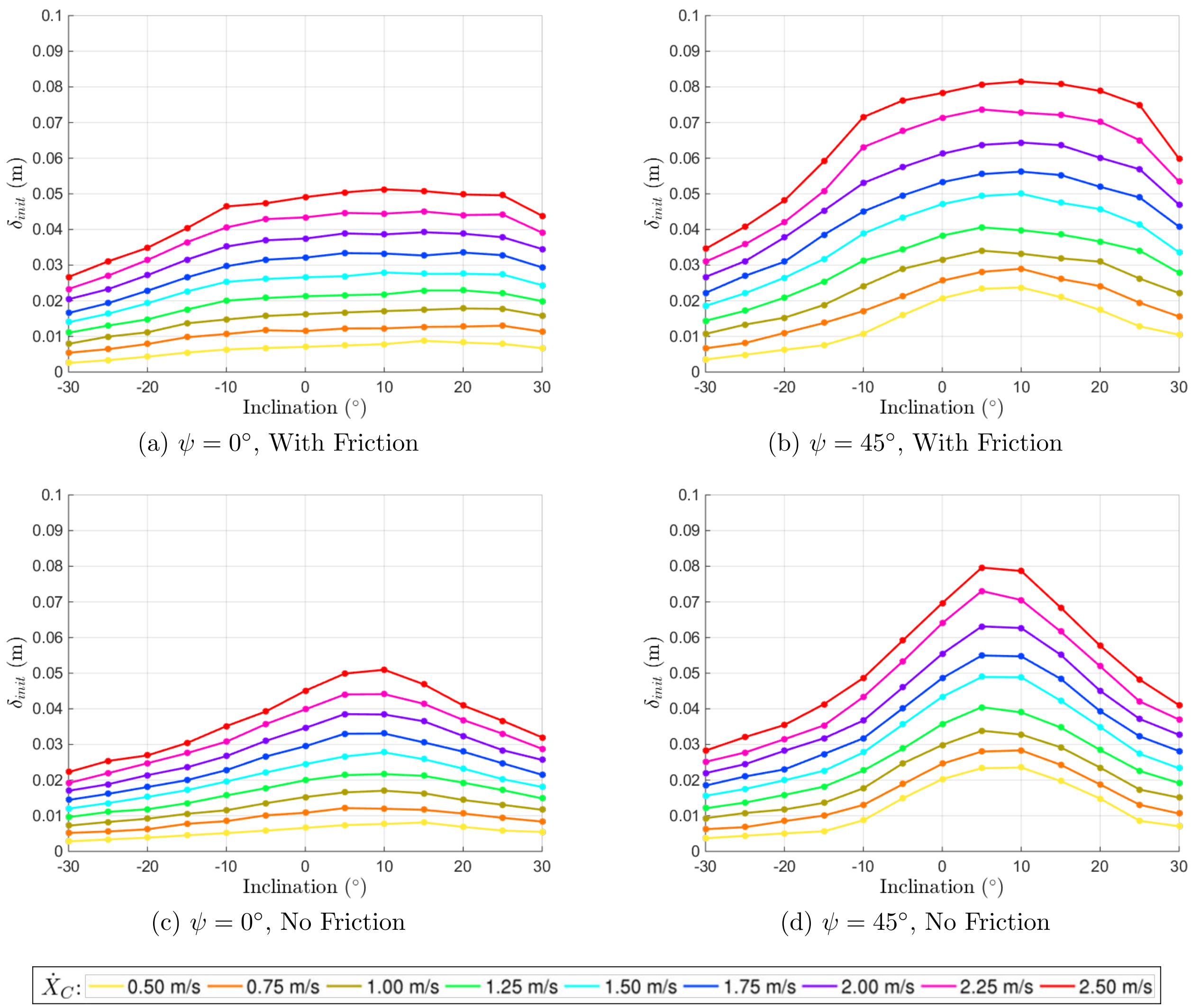

Figure 3–1: Peak deflection during first contact, δ_{init}, at different initial collision inclinations and velocities, for simulations of Navi quadrotor with initial collision headings $\psi = 0°$ (a,c) and $\psi = 45°$ (b,d), with friction (a,b) and without friction (c,d).

deflection to occur at a wider range of inclination angles, such that there is a 'plateau' for deflection curves with friction. Collisions in this range experience a friction force large enough to counteract the moment transmitted by the normal force applied at the contact point, resulting in a negligible contact moment $\mathbf{M}_C$, and a more direct contact. Without friction, there is no additional moment to counteract vehicle rotation, and no plateau is present.

Navi's bumpers are quite flexible, which is reflected in the deflection values observed in simulations. The most direct first contact at a collision velocity of $\dot{X}_C = 2.50$ m/s produces the greatest bumper deflection: 20% of the bumper diameter for a two bumper initial contact with a 53 N peak normal contact force, and 32% for a strictly one bumper initial contact with a 72 N peak normal contact force. These percentages are reasonable, given the maximum deflection seen during bumper parameter characterization was 5% of the bumper diameter for a 20 N static load, the maximum load that could be handled by the measurement setup. The relationship between the static load and bumper deflection (the second term of Equation (2.10)) is concave (i.e., the exponent n is less than 1), and dominates at the moment of peak normal force (when $\dot{\delta} \approx 0$ m/s in the non-linear damping term), so a unit increase in peak normal contact force would require a larger increase in bumper deflection, as observed in the simulation results.

3.3 Angular Velocity x and y Components Response

The collision response can be quantified by the peak angular velocity x and y components magnitude (i.e., $||[p\ q]^T||$) after the first contact, denoted as $||\boldsymbol{\omega}_{xy}||_{PEAK}$. This is a good indicator of the collision response *intensity*, as higher pitch and roll rates are expected when the collision causes the vehicle to spin out of control and crash.

As expected, higher $||\boldsymbol{\omega}_{xy}||_{PEAK}$ values are seen for increasing $\dot{X}_C$ in Figure 3–2. The $||\boldsymbol{\omega}_{xy}||_{PEAK}$ curves are largely unaffected by heading.

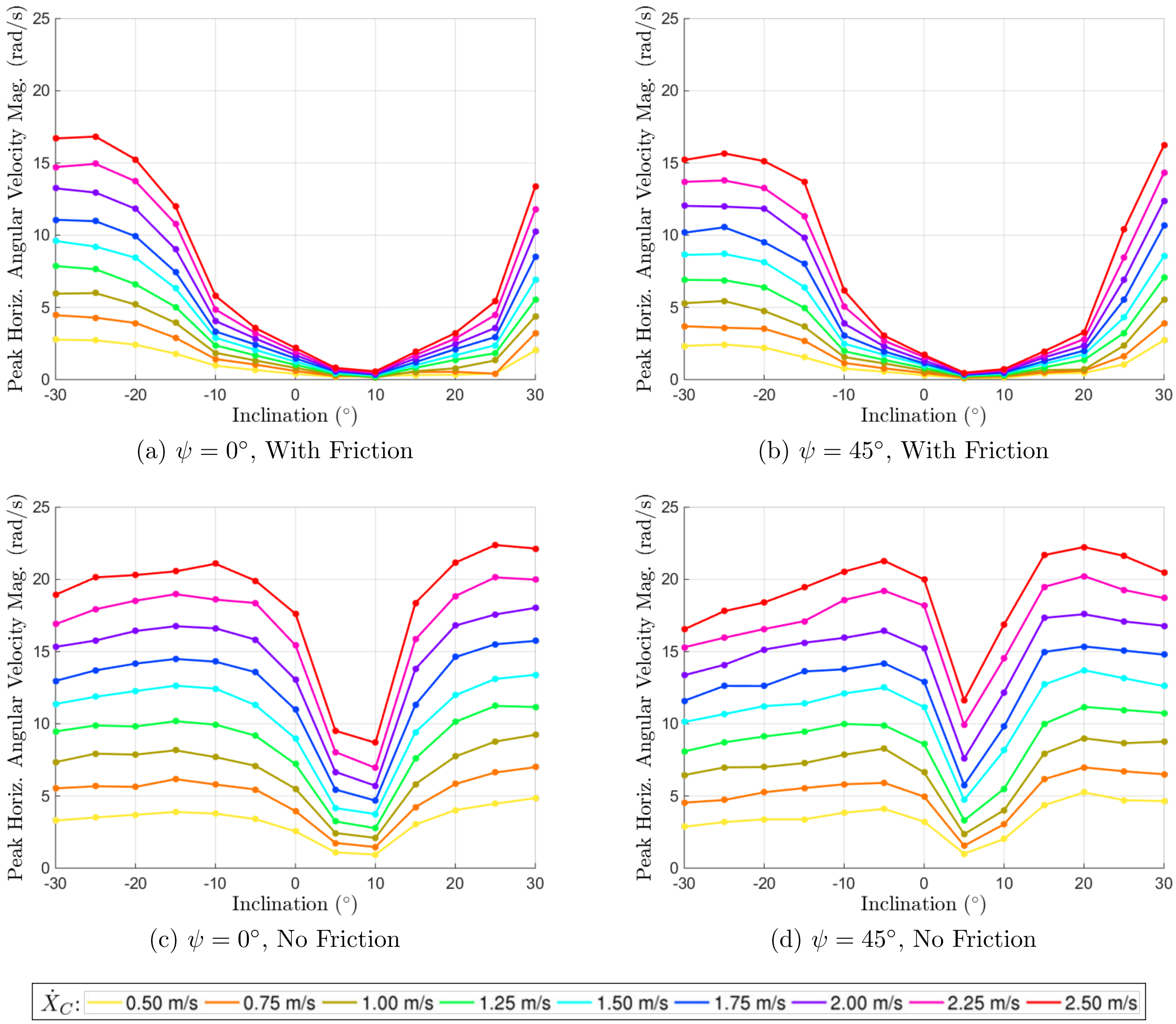

(a) $\psi = 0°$, With Friction

(b) $\psi = 45°$, With Friction

(c) $\psi = 0°$, No Friction

(d) $\psi = 45°$, No Friction

Figure 3–2: First peak angular velocity x and y components magnitude after first contact, $||\boldsymbol{\omega}_{xy}||_{PEAK}$, at different initial collision inclinations and velocities, for simulations of Navi quadrotor with initial collision headings $\psi = 0°$ (a,c) and $\psi = 45°$ (b,d), with friction (a,b) and without friction (c,d).

Minimum $||\boldsymbol{\omega}_{xy}||_{PEAK}$ values occur at $\sim 9^\circ$, because collisions around this inclination result in the lowest contact moment applied to the quadrotor, as discussed in the deflection curve analysis above. Accordingly, this inclination corresponds with where peak deflection values are observed in Figure 3–1. In general, as the inclination angle deviates from $\sim 9^\circ$, $||\boldsymbol{\omega}_{xy}||_{PEAK}$ increases until a maximum value, and then levels off. The curves are asymmetric about $\sim 9^\circ$, with slightly higher $||\boldsymbol{\omega}_{xy}||_{PEAK}$ values predicted for positive deviations from the minimum value, compared to negative deviations. This can be attributed to a higher inclination corresponding with a higher percentage of the thruster forces being directed in the XY plane, toward the wall, before the collision. This means the quadrotor has more inertia toward the wall, resulting in a more intense rotational response, and higher p and q values experienced.

Figure 3–2 also shows that all $||\boldsymbol{\omega}_{xy}||_{PEAK}$ values are lower with friction present. This is because the first contacting bumper(s) maintains contact with the wall while the quadrotor rotates due to $\mathbf{M}_C$, for either flipping direction. With friction present, the friction force F_f at these first contacting bumpers is directed to resist the quadrotor rotation, causing a lower $||\boldsymbol{\omega}_{xy}||_{PEAK}$. With friction, the $||\boldsymbol{\omega}_{xy}||_{PEAK}$ values are especially low for the same region where a 'plateau' occurs in the deflection curves with friction (Figures 3–1a and 3–1b), in accordance with a lower $\mathbf{M}_C$ inducing less rotation, and a more direct contact.

3.4 General Collision Response

Through a combination of visually inspecting the collision response, and examining the post-collision inclination response, the general collision response can be classified by one of five categories. A quadrotor of category:

- Away Big (AB) flips *away* from the wall, experiencing rapid and large rotational motion, such that the inclination decreases to $\zeta \leq -60^\circ$ after the first contact at the fore bumper(s). This large rotation causes the majority of quadrotors with AB responses to lose control into a somersault-like response followed by a crash away from the wall.

- Away Small (AS) flips *away* from the wall, experiencing small rotational motion, such that the inclination decreases to $-60° < \zeta \leq -30°$ after the first contact at the fore bumper(s).
- Level (L) flips *away* from or *towards* the wall, experiencing minimal rotational motion after the first contact at the fore bumper(s), such that the inclination remains within the range $-30° < \zeta \leq 30°$, and the vehicle maintains level orientation.
- Toward Small (TS) flips *toward* the wall experiencing small rotational motion, such that the inclination increases to $30° < \zeta \leq 60°$ after the first contact at the fore bumper(s). The constant attitude setpoint toward the wall causes the majority of quadrotors with TS responses to have a subsequent contact also at the fore bumper(s), followed by successive contacts with the wall, resulting in the quadrotor 'sliding' downwards until crashing.
- Toward Big (TB) flips *toward* the wall, experiencing rapid and large rotational motion, such that the inclination increases to $\zeta > 60°$ after the first contact at the fore bumper(s). This large rotation causes the majority of quadrotors with TB responses to destabilize into a vertical orientation against the wall, causing a subsequent contact to occur at the aft bumper(s). A series of successive impacts with the wall follows, usually resulting in the quadrotor 'sliding' downwards until crashing. The remaining collisions in the TB category are characterized by a visual response similar to the TS category, as described above.

A 'crash' occurs in simulation when the vehicle reaches $Z = 0$ m within 0.9 s after first contact. The general quadrotor responses, defined by one of the above categories and whether the vehicle crashes, are illustrated in Figure 3–3 for the array of collision conditions.

As expected, the TB and AB responses are seen at higher inclination magnitudes and velocities compared to the TS and AS responses respectively. The majority of collisions with initial inclination values above $\sim 9°$ produce TS or TB responses, when the contact point

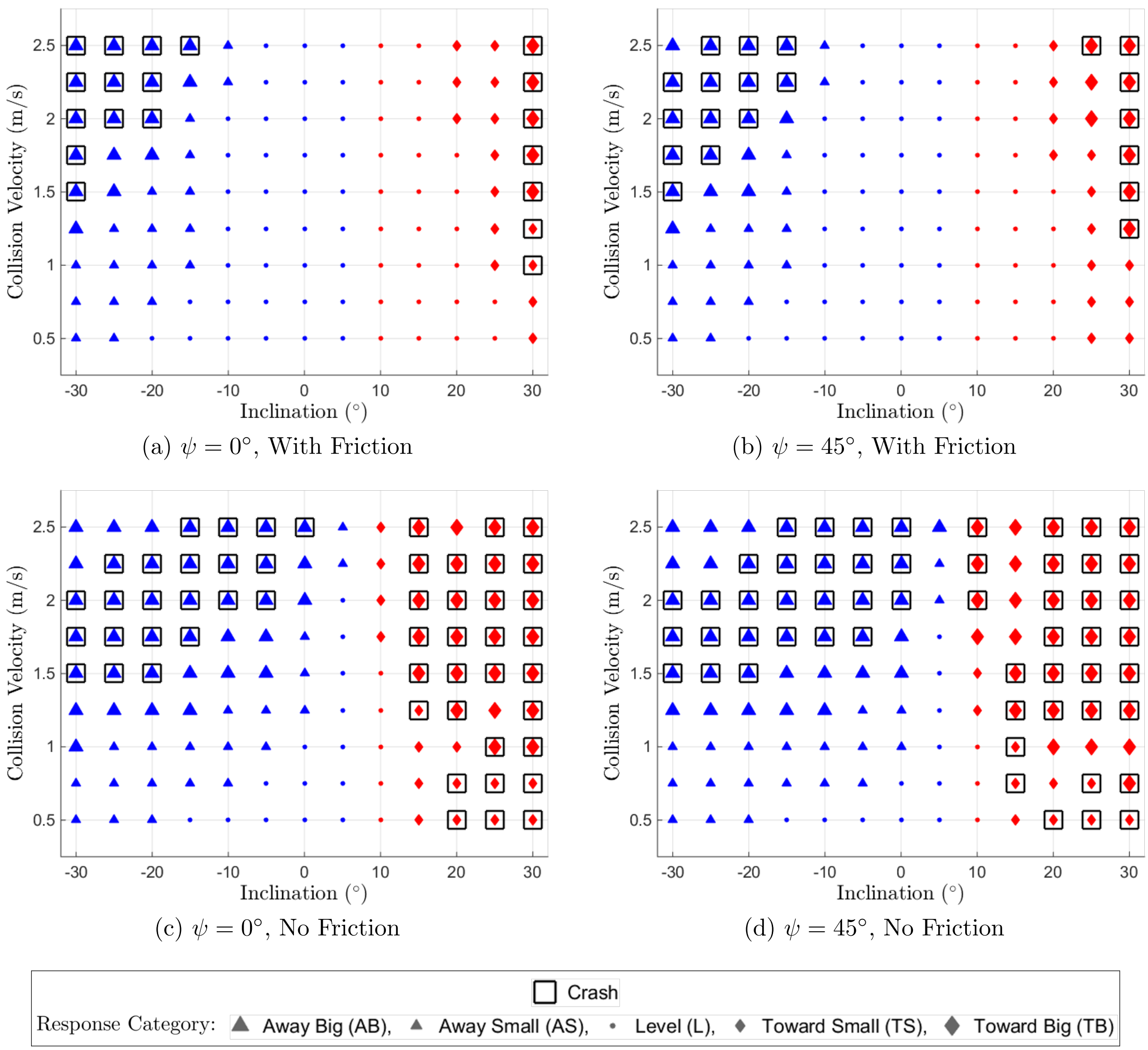

Figure 3–3: General quadrotor response at different initial collision inclinations and velocities, for simulations of Navi quadrotor with initial collision headings $\psi = 0°$ (a,c) and $\psi = 45°$ (b,d), with friction (a,b) and without friction (c,d). Quadrotor responses flipping with any intensity *away* from and *toward* the wall are indicated in blue and red respectively.

$\mathbf{p}_C$ is located below the CM, and the associated contact moment $\mathbf{M}_C$ rotates the vehicle toward the wall. Conversely, when initial inclination values are below $\sim 9°$, $\mathbf{p}_C$ is above the CM, $\mathbf{M}_C$ rotates the vehicle away from the wall, generating AS or AB responses. When $\mathbf{p}_C$ is nearly horizontal with the CM, $\mathbf{M}_C$ is small, generating a L response. These observations on the quadrotor flipping direction are in agreement with the experimental results reported in [52].

Because crashes occur at inclinations deviating from $\sim 9°$ and high collision velocities, no quadrotor with a L or AS response crash. A quadrotor with a TS response can crash due to successive contacts with the wall, and/or the inability to re-orient itself in the constrained space, versus an AS response that does not encounter these problems. For initial conditions causing a crash, the first contact force is large enough to destabilize the quadrotor into a 'somersault' response, losing the thrusting direction and therefore control. There are a few inconsistencies in the trends for which initial conditions cause a crash, in cases where the vehicle flips toward the wall. These inconsistencies are best demonstrated by Figure 3–3d, where crashes do not occur at $\zeta = 15°$ for $\dot{X}_C = \{1.75,\ 2.00,\ 2.25,\ 2.50\}$ m/s. This is due to the unpredictable nature of collisions that involve multiple contacts with the wall. In these particular collisions, the subsequent contact forces re-orient the quadrotor to regain its thrusting direction, and a crash does not occur. The accidental re-orientation from subsequent contacts also occur at $\zeta < -15°$, for $\dot{X}_C = 2.50$ m/s and at $\zeta < -20°$, for $\dot{X}_C = 2.25$ m/s. In general, however, and for recovery control, crashes should be expected for collisions with high initial ζ magnitudes, at high collision velocities.

3.5 Full Quadrotor Collision Response

Now, the full simulated response is examined for four example scenarios. Two simulations with friction show an AB collision response in Figure 3–4, and a TB response in Figure 3–5. Both scenarios are simulated using Navi, at incoming collision speed $\dot{X}_C = 2$ m/s, and heading $\psi = 45°$. The ζ angles chosen achieve the different response categories: $\zeta = -25°$

for the AB response, and $\zeta = 25°$ for the TB response. Two additional simulations with the same initial collision conditions as above are performed, but without friction. The corresponding AB and TB collision responses are in Figures 3–6 and 3–7 respectively. The standard control strategy described previously in Section 3.1.2 is used, setting the desired roll ϕ_{des}, pitch θ_{des}, and yaw ψ_{des} to be constant and equal to the corresponding initial angles that achieve the prescribed inclination and heading.

Normal contact force magnitudes, friction forces in $\mathcal{F}_I$, and quadrotor states are shown for the AB collision response with friction in Figure 3–4, and a timeline providing a detailed description of the quadrotor response over time is in Table 3–3. The same information is displayed in Figure 3–5 and Table 3–4 for the TB collision response scenario with friction. For more intense collisions in the TB response category, the quadrotor will flip rapidly toward the wall, with the second contact at the aft bumpers — a response demonstrated by the example TB response after 0.75 s. Both presented collisions with friction begin at simulation time $t = 0$ s, and show the standard attitude controller not being able to compensate for the contact force and moment, leading to a crash. Example scenarios for the L and AS response categories are omitted, as the vehicle remains stable throughout the collision, thus the full response is not particularly noteworthy. A TS response is similar to the TB response described in Table 3–4 and shown in Figure 3–5, however the inclination does not exceed 60°, or 1.05 rad.

The collisions without friction also begin at simulation time $t = 0$ s, and lead to crashes. The absence of friction in Figure 3–6 compared to Figure 3–4 for the AB collision response has minimal effect on the quadrotor state response intensity. The first minimum inclination peak and first angular velocity x and y components peak occur 0.02 s and 0.01 s earlier in the simulation without friction respectively. The visual response does differ between the two simulations, as the quadrotor rotates into an upside-down orientation and has a subsequent impact on a fore bumper before crashing in the scenario without friction. The effect of friction on collision response is more significant when comparing the TB collision response in Figure 3–7 without friction to Figure 3–5 with friction. Without friction, there is no subsequent impact at the fore bumpers before the quadrotor flips into a vertical orientation and instead has a second contact on the aft bumpers, similar to the response with friction after 0.75 s. Accordingly, the maximum angular velocity x and y component values occur much earlier, and are higher. This more intense collision response results in the vehicle crashing 0.6 s before the crash in the simulation with friction.

3.6 Implications for Quadrotor Recovery Control

Figure 3–3 is important in that it demonstrates multiple factors influencing collision response intensity, and ultimately if the quadrotor crashes. For intelligent recovery control, indicators of collision velocity and inclination must be provided to the recovery controller. An additional indicator can be the angular velocity x and y components magnitude, which will need to be measured well before the $||\boldsymbol{\omega}_{xy}||_{PEAK}$ values in Figure 3–2, for a responsive recovery controller. The friction coefficient is an important consideration for the collision response intensity as well. However, since this coefficient cannot be easily estimated with on-board sensors, the vehicle's angular velocity x and y components magnitude may be sufficient to capture the effect of friction on the vehicle rotational motion.

The simulations show logical responses to different collision conditions, providing confidence in the quadrotor contact dynamics model. Along with the experimental validation in Chapter 4, it can be concluded that the model provides good fidelity for recovery control development.

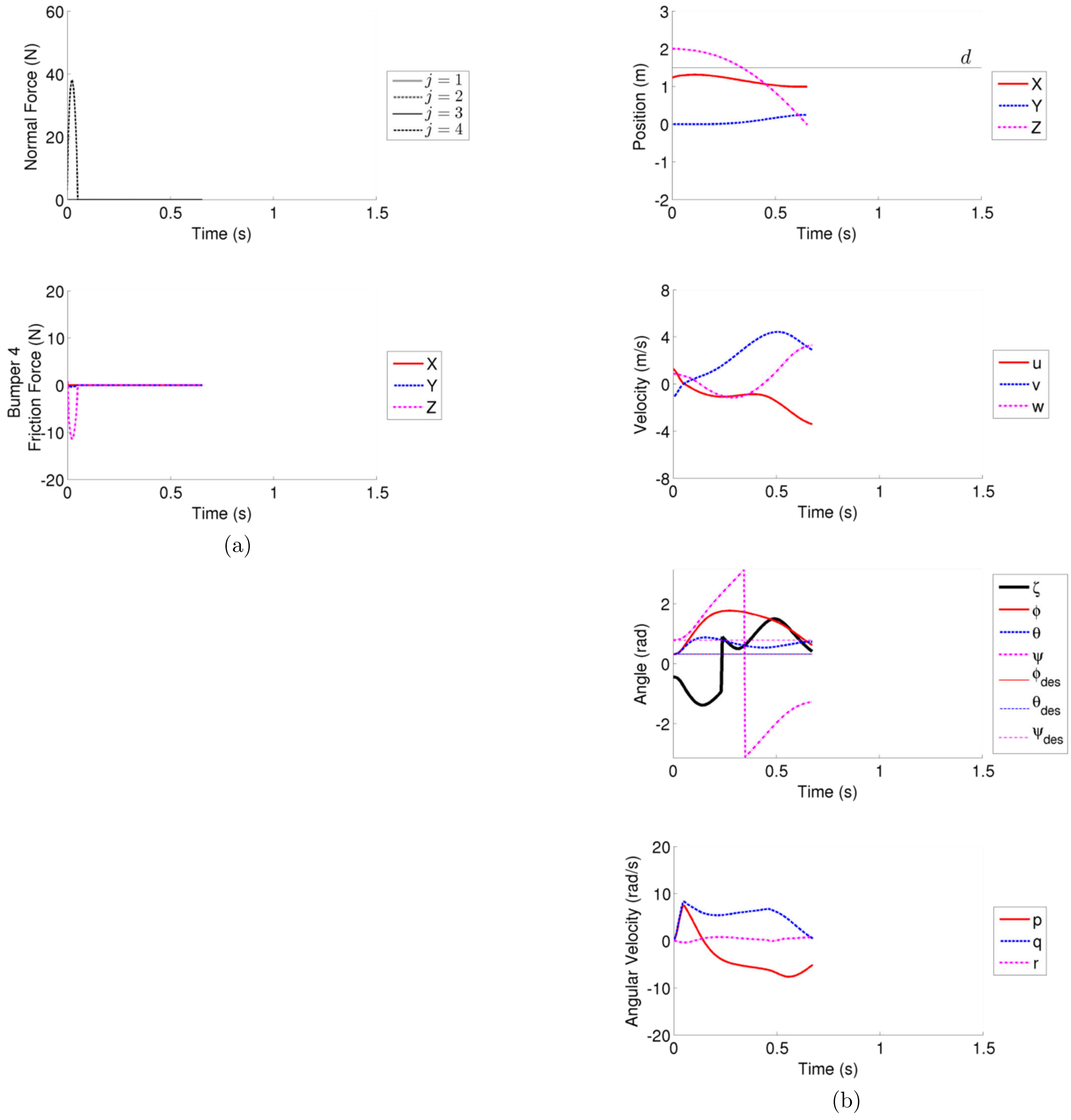

Figure 3–4: Quadrotor Away Big response to incoming collision speed $\dot{X}_C = 2$ m/s, inclination $\zeta = -25°$, and heading $\psi = 45°$. Friction is present ($\mu_C = 0.3$). The normal force magnitude and the $\mathcal{F}_I$ components of friction force for the contacting bumper are in (a), and the quadrotor states are in (b).

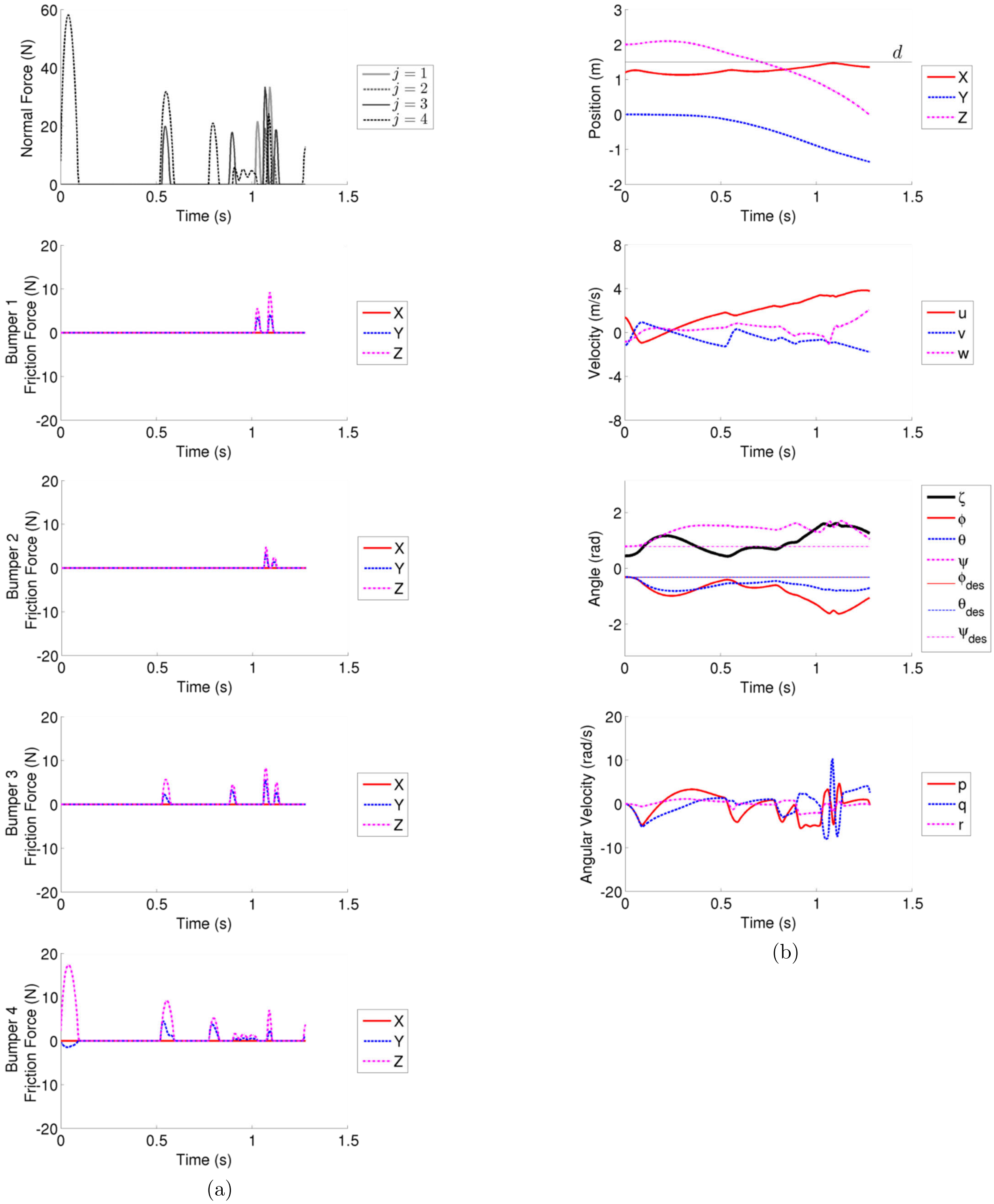

Figure 3–5: Quadrotor Toward Big response to incoming collision speed $\dot{X}_C = 2$ m/s, inclination $\zeta = 25°$, and heading $\psi = 45°$. Friction is present ($\mu_C = 0.3$). The normal force magnitude and the $\mathcal{F}_I$ components of friction force for the contacting bumpers are in (a), and the quadrotor states are in (b).

Table 3–3: Timeline for Example Away Big Collision Response

Time (s)	Response Description
0.00 to 0.05	The first impact at the fore bumper generates a normal force, and the resulting moment rotates the quadrotor away from the wall (seen by the increasing ϕ and θ values), which moves the contact point $\mathbf{p}_C$ upwards simultaneously. Accordingly, the friction force is generated to resist the motion of $\mathbf{p}_C$, and is directed downwards.
0.05	The impact is large enough to destabilize the quadrotor, flipping the vehicle rapidly, and there is a spike in the angular velocity x and y components.
0.15	The vehicle somersaults into a vertical orientation, losing thrusting direction, as seen by the peak θ angle, before continuing its flipping motion into the 'upside-down' region. The maximum inclination ζ below $-60°$, or -1.05 rad after first contact places this collision in the AB category.
0.15 to 0.70	The vehicle steadily loses altitude, and continues its somersaulting motion (seen by the fluctuating Euler angles). Deviations from $Y = 0$ m are due to the Navi quadrotor non-zero products of inertia.
0.70	The quadrotor crashes 0.5 m away from the wall, indicative of an AB response.

Table 3–4: Timeline for Example Toward Big Collision Response

Time (s)	Response Description
0.00 to 0.10	The first impact at bumper 4 generates a normal force, and the resulting moment rotates the quadrotor toward the wall (seen by the decreasing ϕ and θ values), which moves the contact point $\mathbf{p}_C$ downwards simultaneously. Accordingly, the friction force on bumper 4 is generated to resist the motion of $\mathbf{p}_C$, and is directed principally upwards.
0.10	Peak angular velocity x and y components are experienced, as the quadrotor rotates rapidly toward the wall.
0.10 to 0.50	The quadrotor is pushed away from the wall by the first impact (seen by slight X position decrease), while rotating toward the wall (seen by the peak negative ϕ and θ values). The maximum inclination ζ above 60°, or 1.05 rad after first contact places this collision in the TB category. The quadrotor then returns to a more level orientation, as the ϕ and θ values increase, but do not go beyond 0°. During this interval, the heading drifts such that bumpers 3 and 4 are now the fore bumpers.
0.50 to 0.60	A subsequent impact occurs at the fore bumpers. Once gain, the resulting moment rotates the quadrotor toward the wall (seen by the decreasing ϕ and θ values), and friction forces at bumpers 3 and 4 are principally directed upwards to resist this rotation. This subsequent impact has a peak total normal force less than the first impact, as it occurs on two bumpers, and the initial contact speed is lower. The vehicle has now started to lose altitude.

Table 3–4: Timeline for Example Toward Big Collision Response (continued)

Time (s)	Response Description
0.75 to 0.90	A third impact occurs at the two fore bumpers in succession, and the vehicle is now pitched to be nearly vertical, while still in contact with the wall.
0.90 to 1.00	A continuous, sliding interaction occurs at bumper 4, seen by the continuous normal contact force with several peaks. This is in contrast to the previous impulsive contacts, which are characterized by a single peak.
1.00 to 1.15	Now oriented vertically, the aft and fore bumpers have unpredictable, successive contacts with the wall, while 'sliding' downwards, as the Z position approaches 0 m. In this orientation, the vehicle CM is much closer to the wall, and the X position approaches d.
1.15 to 1.25	The force of the successive contact separates the quadrotor from the wall for a brief interval.
1.25 to 1.30	The quadrotor heads back into the wall for a final impact at a fore bumper before crashing beside the wall.

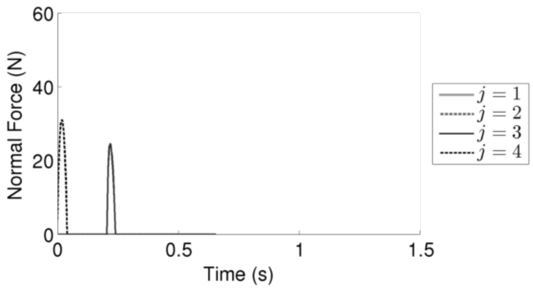

(a)

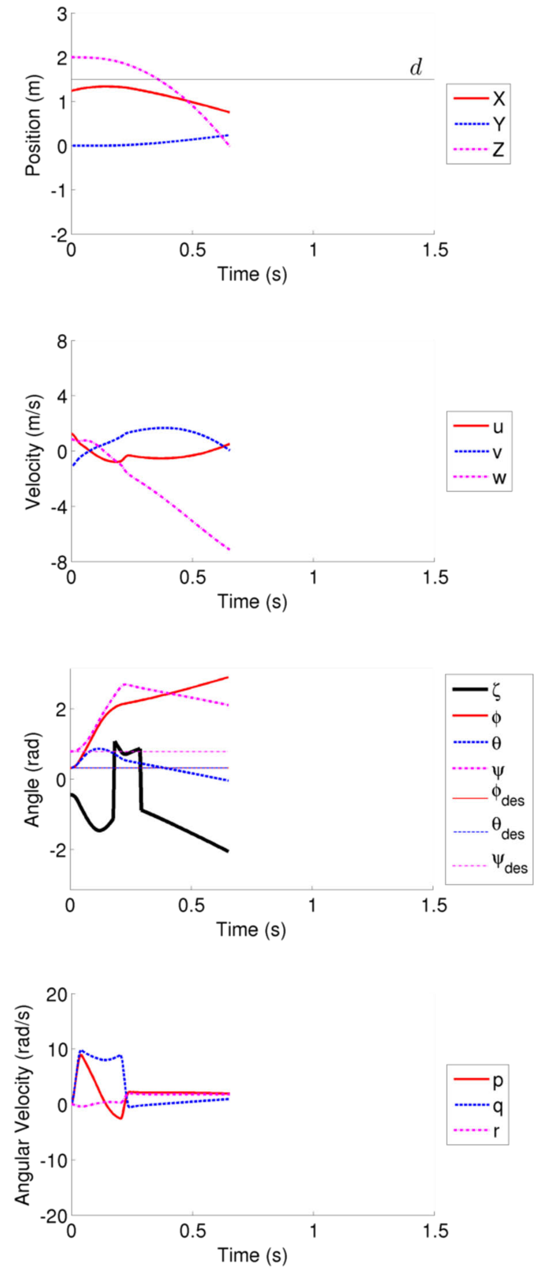

(b)

Figure 3–6: Quadrotor Away Big response to incoming collision speed $\dot{X}_C = 2$ m/s, inclination $\zeta = -25°$, and heading $\psi = 45°$. Friction is not present (i.e., $\mu_C = 0$). The normal force magnitude is shown in (a), and the quadrotor states are in (b).

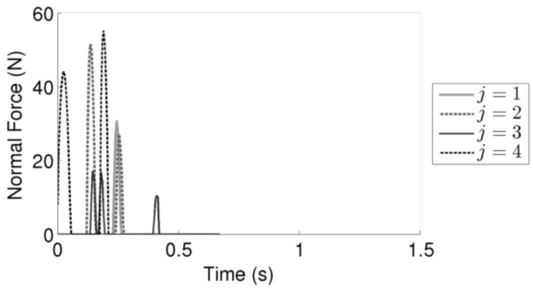

(a)

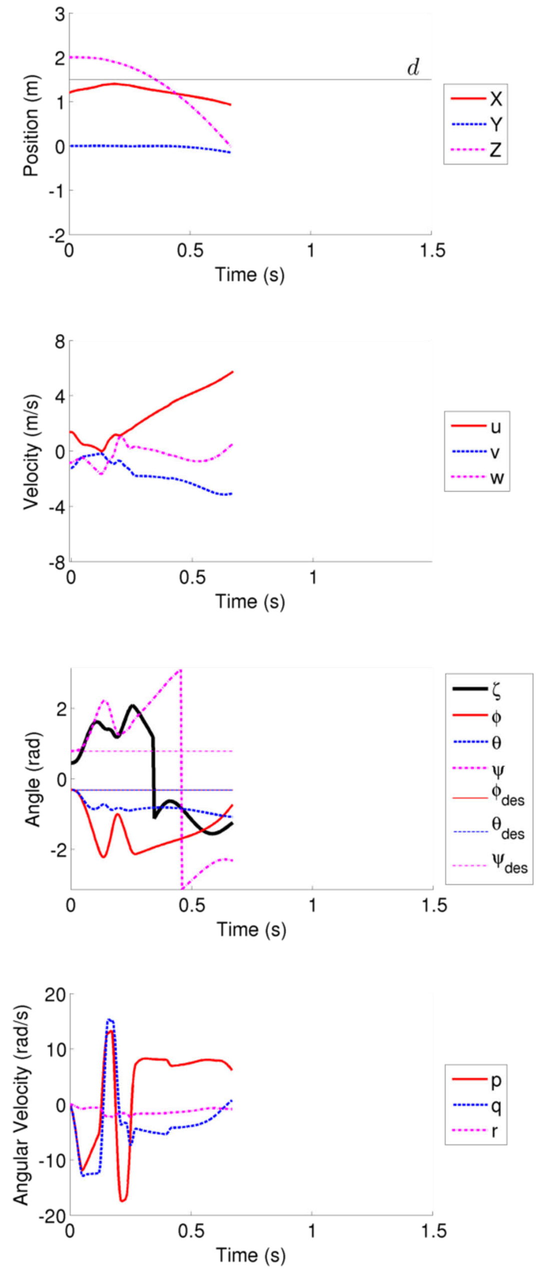

(b)

Figure 3–7: Quadrotor Toward Big response to incoming collision speed $\dot{X}_C = 2$ m/s, inclination $\zeta = 25°$, and heading $\psi = 45°$. Friction is not present (i.e., $\mu_C = 0$). The normal force magnitude is shown in (a), and the quadrotor states are in (b).

CHAPTER 4
Experimental Validation of Collision Modelling

The dynamics model presented in Chapter 2 is validated by demonstrating correspondence between real-life experimental collisions and their simulated reconstructions. Two experimental quadrotor platforms are employed for the validations: 'Navi' and 'Spiri', seen in Figure 1–2. Experimental testing reveals that using Spiri poses significant difficulties to successful recovery control in Section 4.1. As a result, only Navi is used for developing quadrotor collision recovery in Chapter 5. However, experimental validations are shown for both platforms to evaluate model accuracy for multiple vehicles. Both the experimental and simulated wall spans the YZ plane, and is normal to the X axis. The simulated wall is located at a distance $d = 1.5$ m along the X axis.

4.1 Experiments and Validation with Spiri

4.1.1 Spiri Quadrotor Platform

The Spiri quadrotor used in experiments is a prototype platform from Pleiades Robotics Inc. The majority of Spiri's on-board electronics are integrated into a single board, including the motor controllers. The body and bumpers are 3-D printed with Selective Laser Sintering in nylon[1] , which are designed to protect the electronics and propellers during collisions. The bumpers are snap-mounted to the main body, and may detach when the quadrotor crashes or encounters a substantial normal impact force transverse to the propeller plane.

[1] Selective Laser Sintering uses lasers to fuse plastic powder particles together layer by layer, while normal 3-D printing relies on the melted filament layers fusing together during the cooling process.

The attitude controller used in the experiments is of the same form as the controller used in Chapter 3 model verification simulations, as described in Section 3.1.2. Since position control is not available using this platform, manual joystick control is used to fly the vehicle.

4.1.2 Spiri Quadrotor Parameters

The inertial, geometric, propeller, and contact parameters in Table 3–2 are used for the Spiri experiment reconstructions in simulation. Navi and Spiri share the same motor supports, central frame connecting the motor supports, motors, and propellers. The electronics necessary for operation of the vehicle are completely different between the two platforms, which is reflected in the quadrotor mass and CM location, in turn changing the thruster locations relative to the CM ($\mathbf{r}_{Tj},\ j \in \{1, 2, 3, 4\}$). The main physical distinction between the platforms comes from the bumpers, which are less stiff and have smaller radii on Spiri. The bumper centres coincide with the thruster locations on Spiri only.

All parameters determined with measurements for Navi in Section 3.1.1 were determined for Spiri using the same methods. Static deflection measurements for determining the normal contact parameters k and n used in (2.10) were performed on an independent, detached bumper for Spiri. The Coulomb friction coefficient for sliding μ_C used in (2.14) is lower on Spiri, as its bumpers are 3-D printed with Selective Laser Sintering in nylon.

4.1.3 Spiri Experiment Setup

Twelve live experiments were performed on Spiri flown into the wall, under manual joystick attitude and thrust inputs, at varying initial inclination angles and incoming velocities. In every experiment using Spiri, the quadrotor was destabilized by the collision and crashed undamaged onto a foam crash bed.

Spiri's on-board electronics allowed for IMU data to be captured at approximately 20 Hz. Data from the Vicon motion-capture system was logged using ROS at approximately 70 Hz. The side-view of all collisions were captured on video at 29 FPS. These data are post-processed to determine the vehicle's pre-collision orientation and velocity. Additionally, motor speed data recorded at approximately 20 Hz is used to simulate post-collision thruster rotation speeds. A comparison of the experimental setup for the collision sets performed with Spiri and Navi are summarized in Table 4–1.

Table 4–1: Summary of Experimental Setups

Quadrotor	Spiri	Navi
# Total collisions	12	26
# Collisions with valid data	7	22
Low level controller	PID laws	PX4 attitude control
High level controller	Manual joystick	PX4 position control
IMU (3-axis accelerometer and 3-axis gyroscope) data frequency	20 Hz	200 Hz
Barometer data frequency	N/A	200 Hz
Vicon motion capture frequency	70 Hz	70 Hz
Side-view camera frame rate	29 FPS	29 FPS
Top-view high-speed camera frame rate	N/A	500 FPS

4.1.4 Reconstruction of Spiri Collision Conditions in Simulation

Viable data was recorded for seven of twelve experimental tests using the Spiri quadrotor. Careful inspection of the side-view video footage as well as the post-collision motor speed data revealed that motor controller safety power-off was triggered by the motor stall when a propeller/bumper experienced contact with the wall. Accordingly, generation of simulated responses for comparison to experimental results required matching not only the respective initial conditions of the vehicle, but also the motor speeds after the first bumper to wall contact.

The start of the collision is identified from a spike in the accelerometer reading. The attitude of Spiri at the instant of impact is computed as a weighted average of the IMU filtered attitude, the attitude estimate from the motion-capture system, and the angle between Spiri's xy body plane and the wall, as estimated from a side-view video frame at impact.

The incoming horizontal and vertical velocities are estimated using a band pass filter on the motion-captured position data with cut-off frequencies at 10 and 50 Hz. The simulated initial impact conditions all lie within the error ranges of the estimated initial conditions in Table 4–2, which in turn were generated according to the discrepancies seen between the different measurement methods.

As a result of motor power-off on impact noted earlier, the recorded motor speed data shows that the four motor speeds decreased at varying rates after first contact towards zero. This is imitated in simulation by decreasing the four propeller angular velocities at matching rates to those recorded from experiment.

4.1.5 Comparison of Spiri to Simulated Response

Table 4–2: Impact Conditions and Response Comparison between Spiri Experiments and Simulations

Trial	Experiment				Simulation Response Category	Qualitative Correspondence Duration (s)
	ζ (°)	$\dot{X}_C$ (m/s) $\pm$ 0.05	ψ (°) $\pm$ 6.4	Response Category		
S-1	4.5 ± 7	0.7	20	TS	TS	0.3
S-2	4.4 ± 7	1.1	10	TS	TS	0.4
S-3	6.8 ± 7	1.1	14	TS	TS	0.6
S-4	11 ± 8	1.3	14	TS	TS	0.4
S-5	15 ± 7	2.0	11	TB	TB	0.2
S-6	16 ± 7	2.7	4.0	TB	TB	0.3
S-7	19 ± 8	2.0	11	TB	TB	0.4

Table 4–2 summarizes the initial collision conditions measured during the seven viable experiments and compares the collision response seen in experiment verses simulation. The first observation on these results is that only category TS and TB responses of the vehicle occurred: this is as a consequence of the motor power-off phenomenon since both of these

response types involve the vehicle flipping toward the wall after the first impact—a behaviour consistent with loss of thrust on the impacted motors.

All experimental response types are matched in simulation. Furthermore, good correspondence is observed in visual comparison of simulated and experimental post-collision behaviour. The qualitative correspondences (last column in Table 4–2) continue for ≥ 0.3 s, some spanning the entire duration from first bumper contact until the quadrotor crashes. Example side-by-side comparisons of snapshots from the experimental and simulated collisions are seen in Figure 4–1 for Trial S-6 (category TB).

The duration of qualitative correspondence is shortest for Trial S-5. In this experiment, the first impact turned the quadrotor sideways while it flipped toward the wall, leading to a second impact on only one of its aft bumpers, where significant deformation was seen in the direction *transverse* to the propeller plane. This differs from the other TB trials, where the second impact occurred on two aft bumpers. A somersault-like response *away* from the wall followed, and the aircraft crashed with one additional grazing contact on the second aft bumper. In simulation, after the second impact on the single aft bumper, the qualitative correspondence ends, as the aircraft continues its flipping motion *toward* the wall, and then crashes away from the wall without additional impacts. The contact model does not capture properly the transverse stiffness of the bumpers, nor the additional flexibility and play in the transverse direction at the bumper snap-mounted attachment to the body. Hence, a crash resulting in large impact forces directed transversely to the rotor plane is not simulated with full accuracy using the present model.

4.2 Experiments and Validation with Navi

4.2.1 Navi Quadrotor Platform

Since the Navi quadrotor was custom built, more details are provided on its on-board electronics. A Pixhawk flight controller runs the PX4 flight stack [53] for low level attitude control and high level position control with external position data, making use of an internal

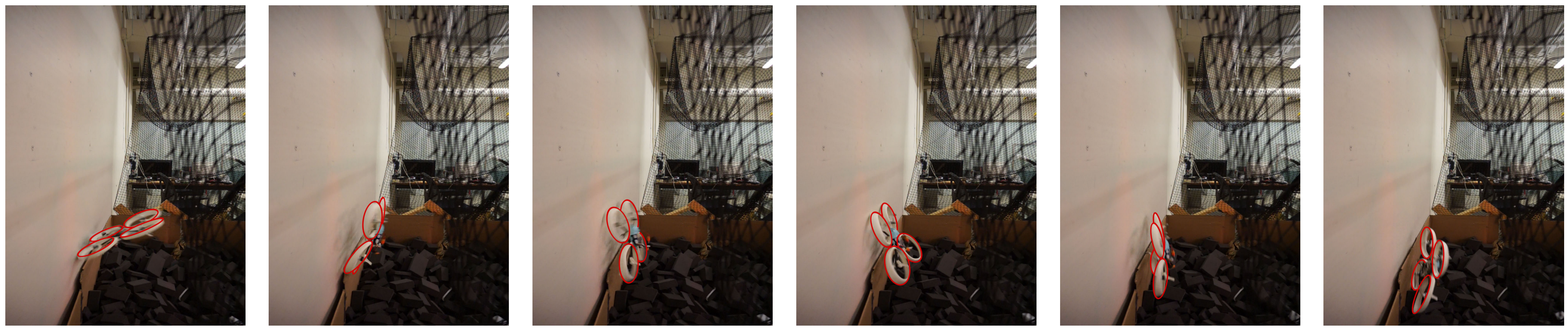

(a) $t = 0.0$ s (b) $t = 0.067$ s (c) $t = 0.1$ s (d) $t = 0.133$ s (e) $t = 0.2$ s (f) $t = 0.267$ s

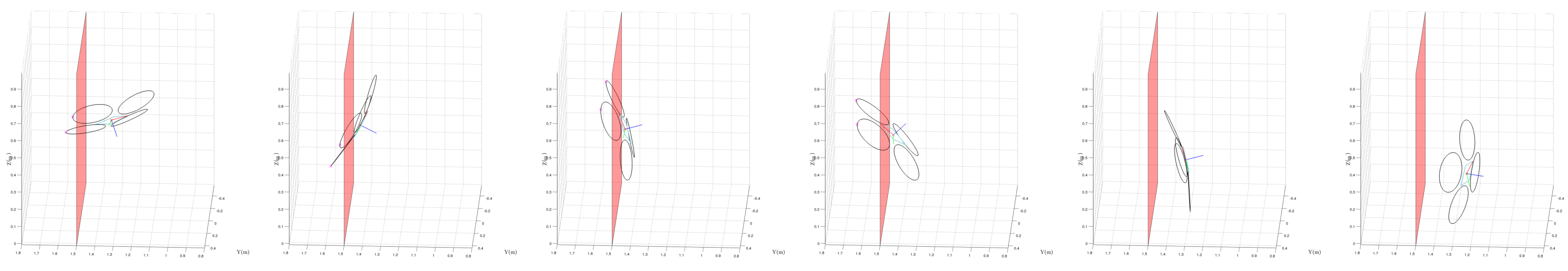

(g) $t = 0.0$ s (h) $t = 0.07$ s (i) $t = 0.1$ s (j) $t = 0.13$ s (k) $t = 0.215$ s (l) $t = 0.25$ s

Figure 4–1: Qualitative comparison of experimental (a-f) and simulated (g-l) quadrotor response with matching initial collision conditions for Trial S-6, exhibiting a Toward Big (TB) response. The bumper outside edges are approximately outlined in the experimental response (a-f) for clarity. Time after first contact is indicated in the subfigure captions. Images (a) and (f) mimic the initial impact conditions and initial deformation, (b) and (h) show the pitching into the wall of a TB collision, (c-d) and (i-j) show destabilization of the quadrotor and the impact at the aft bumpers after pitching into the 'upside-down' range, and finally (e) and (k) show the beginning of the quadrotor's descent to the ground (foam bed in the live test).

IMU and barometer for attitude and altitude estimation. An ODROID-XU4 Linux computer runs ROS to facilitate communication between the Vicon motion-capture system and the Pixhawk through wireless internet for position control. Additional transmitter-receiver modules on the platform are for telemetry and RC manual control. Each motor is controlled by an electronic speed controller (ESC), which receives pulse-width modulation (PWM) signals from the Pixhawk. A 3-D printed nylon body encases and protects the electronics during collisions, with the exception of the ESCs and motors, which are mounted on the quadrotor arms. Navi's PLA bumpers are rigidly attached to the quadrotor arms and do not detach due to a collision, unless the bumper is damaged.

Both the PX4 position controller and attitude controller are based on the trajectory-following controller developed by Mellinger and Kumar [5]. The position controller takes a setpoint position and heading, and generates $\boldsymbol{\omega}$ and thrust setpoints for the attitude controller, which are then mapped to thruster RPMs with the PX4 'mixer' module.

4.2.2 Navi Experiment Setup

Using the PX4 position controller, Navi was flown into the wall for 26 live experiments. The initial collision conditions were varied by prescribing different combinations of starting hover positions away from the wall, and target position setpoints located at, or into the wall. All prescribed positions had the same Y and Z components, to collide the quadrotor into the wall in the most direct manner. In addition to hover and target setpoint positions, the corresponding headings were prescribed to be the same in all collisions, and generate a two-bumper initial contact (i.e., ψ setpoint was $0°$). However, a less than ideal PX4 heading estimate generated collision headings deviating from $\psi = 0°$, as seen in Table 4–3. In some experiments, Navi experienced multiple unintelligent[2] and aggressive impacts on the fore bumpers, and had to be manually shut off before it crashed into the foam crash bed for safety reasons. In the remaining experiments, Navi was destabilized by the collision with the wall into an aerobatic motion before crashing into the crash bed.

All PX4 state estimators make use of complementary filters to combine different sensor measurements. The PX4 position controller makes use of the PX4 position and velocity estimator, which has different parameters for horizontal and vertical (altitude) motion. The estimates of horizontal position and velocity use Vicon motion capture position data and accelerometer measurements. The altitude estimate uses Vicon motion capture position, barometer, and accelerometer data. The PX4 attitude controller uses the PX4 attitude estimator, which filters the gyroscope and accelerometer data; magnetometer data is used for the heading estimate. Magnetic interference caused by the spinning motors degrades the magnetometer data, and therefore the PX4 heading estimate.

The on-board IMU and barometer data were captured at approximately 200 Hz. The Vicon motion-capture data was streamed for the position controller and recorded at approximately 70 Hz. The side-view of all collisions were captured on video at 29 FPS. These data are post-processed to determine the vehicle's pre-collision ϕ, θ, and velocity. Additionally, a high-speed camera captured video of the collision from above at 500 FPS, which is used to determine the pre-collision heading ψ, the bumper deflection, and the duration of the first bumper contact. Differences in the experimental setup for the collision experiments using Navi compared to those using Spiri are summarized in Table 4–1.

[2] Here, the impacts are described as unintelligent because the vehicle has no knowledge of the obstacle presence, and continues heading into the obstacle multiple times.

4.2.3 Reconstruction of Navi Collision Conditions in Simulation

Viable data was recorded for 22 of 26 experimental tests using the Navi quadrotor. The top-view high speed videos confirm that motor stall did not occur in any of the tests. However, the propeller still experienced contact with the bumper/wall during more intense first contacts, which would undoubtedly slow its rotation. Aside from stiffer bumpers on the Navi platform, motor stall did not occur because a higher threshold has been implemented to trigger the safety power-off feature with Navi's ESCs. Motor speed data is not available for these collisions, but in the absence of complete motor stall, the high level controller influences collision response most significantly, compared to the short duration slow-down of contacting propellers.

The collision initial conditions are matched in simulation to those measured in experiment. Alike to the experiment reconstruction procedure for Spiri, the collision times are identified from the spikes in the accelerometer readings. The attitude estimate provided by the PX4 flight stack is taken just prior to the collision identification for the initial ϕ and θ values. The top-view camera gives a high accuracy ψ measurement, and ζ can be calculated from the three Euler angles. The incoming velocities are estimated from Vicon position data using the same band pass filter as for the Spiri experiments. The simulated and experimental initial collision conditions in Table 4–3 all lie within the error ranges of $\pm 1^\circ$ for ζ, ± 0.05 m/s for $\dot{X}_C$, and $\pm 1^\circ$ for ψ, which were generated according to the uncertainty of the experimental measurement methods.

Due to the complexity of the PX4 position controller code, it cannot be matched exactly in simulation. Instead, the initial collision conditions produced by the PX4 position controller in experiment are matched by directing the quadrotor into the wall with the attitude controller described in Section 3.1.2. Then, when the first contact begins (i.e., any of the simulated bumpers experience deflection), control switches to mimic the PX4 position and attitude controllers, to capture the response of a position controlled quadrotor that is unaware of the collision. The position and heading control, and attitude control components of Mellinger and Kumar's trajectory-following controller are used [5], as they are the basis for the respective PX4 controllers as well. The controller gains are tuned to generate collision responses similar to those seen in experiment for one trial, and these gains are kept constant for all experiment reconstruction simulations. The post-collision simulated and experimental target position setpoints are the same distance along the X axis into the wall, with Y and Z components matching the initial collision quadrotor position. Finally, the simulated target heading matches the initial heading estimated with the top-view camera for the collision duration.

4.2.4 Comparison of Navi to Simulated Response

The mean and standard deviation of the initial collision conditions measured during the 22 viable experiments is presented for two trial sets in Table 4–3: the first for 7 collisions all with negative initial ζ angles, and the second for 15 collisions all with positive initial ζ angles. The table also includes values for the maximum deflection during the first bumper contact δ_{init}, and the duration of the first bumper contact, both measured in experiment by examining the top-view high speed camera. The last column of Table 4–3 shows the approximate qualitative correspondence duration between the experimental and simulated quadrotor responses, evaluated visually. The complete individual trial results are presented in Appendix A.

The Navi quadrotor exhibited a TS response in all experimental collisions, and the corresponding simulations. Because position control was used to direct Navi into the wall, the initial collision inclination could not be easily prescribed, with the maximum value seen among all the collisions being $\zeta = 11°$ (see Appendix A). For Navi, it was demonstrated that a TB response occurs at a minimum inclination of $\zeta = 25°$ in Figure 3–3, so it is reasonable that no TB responses were observed in the experimental trials. The TS response was still

Table 4–3: Impact Conditions and Response Comparison between Navi Experiments and Simulations

		Initial Conditions			Experiment		Simulation		Qualitative Correspondence Duration (s)
Trial Set	Value	ζ (°)	$\dot{X}_C$ (m/s)	ψ (°)	δ_{init} (m)	1st Contact Duration (s)	δ_{init} (m)	1st Contact Duration (s)	
N-1 to N-7	Mean	-3.9	1.3	11.4	0.016	0.049	0.028	0.080	0.4
	Std. Dev.	2.4	0.2	2.7	0.005	0.002	0.006	0.006	0.1
N-8 to N-22	Mean	5.9	1.5	10.2	0.025	0.053	0.037	0.086	0.5
	Std. Dev.	2.4	0.1	5.3	0.004	0.006	0.003	0.007	0.2

exhibited for negative initial ζ values, as the position setpoint remained ‘inside’ the wall after the first collision, causing the position controller to react aggressively to counteract contact disturbance, and direct the quadrotor into the wall again for subsequent contacts. These situations are good examples of how even mild collision conditions can result in a more extreme response, when using a position controller that is unaware of the obstacle.

The experimental δ_{init} values in Table 4–3 are determined by measuring the shortest pixel distance between the thruster rotational centre and the wall at a video frame showing the moment right before first contact, and a second video frame capturing the moment of greatest bumper deflection, as shown in Figure 4–2. The pixel distances are then mapped to real-life lengths by measuring the pixel distance of an undeflected feature of known physical length on one of the video frames (e.g., the undeformed bumper diameter). The difference between the two lengths is then taken as the measurement of δ_{init}. The average simulation δ_{init} value predicted by the contact model is 0.012 m greater than the experimental value for both trial sets (0.028 - 0.016 for the first set, and 0.037 - 0.025 for the second). This value of 0.012 m is 4.8% of the bumper diameter, and is probably within the error margin of the deflection measurement method.

The first contact durations are over-estimated by the contact dynamics model, by an average of 0.032 s for all 22 trials. This value is small, but beyond the error margin of the measurement method, as the top-view videos were captured at 500 FPS, or one frame every 0.002 s.

Despite the differences in first contact deformation and duration, good qualitative correspondence is again observed in visual comparison of simulated and experimental post-collision behaviour. On average, the duration of qualitative correspondence is ten times greater than the first bumper contact duration. Example side-by-side comparisons of snapshots from the experimental and simulated collisions are seen in Figure 4–3 for Trial N-11.

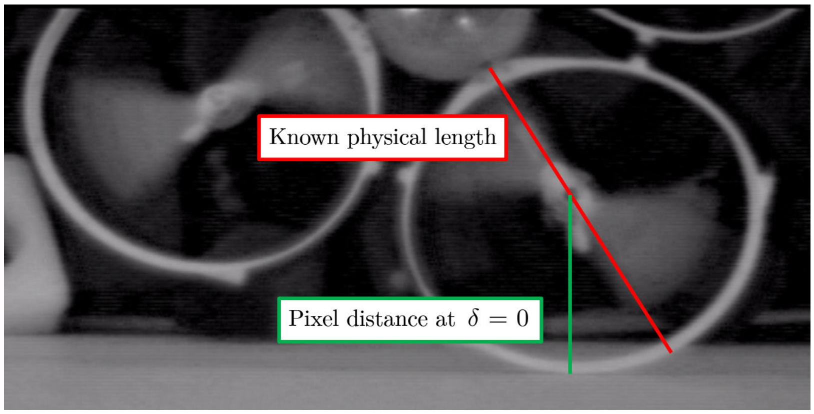

(a)

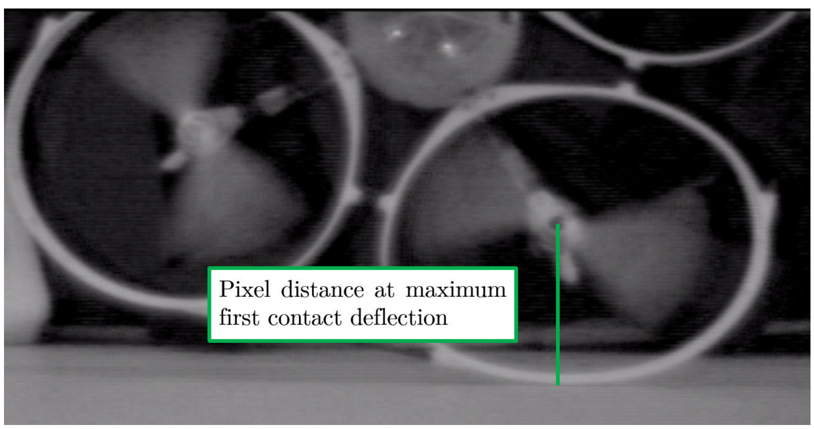

(b)

Figure 4–2: Bumper deflection measurement using top-view video frames. The pixel lengths of the known feature and the undeformed distance between the thruster center and the wall are in (a), and the distance between the thruster center and the wall at the moment of maximum bumper deflection during the first contact are in (b).

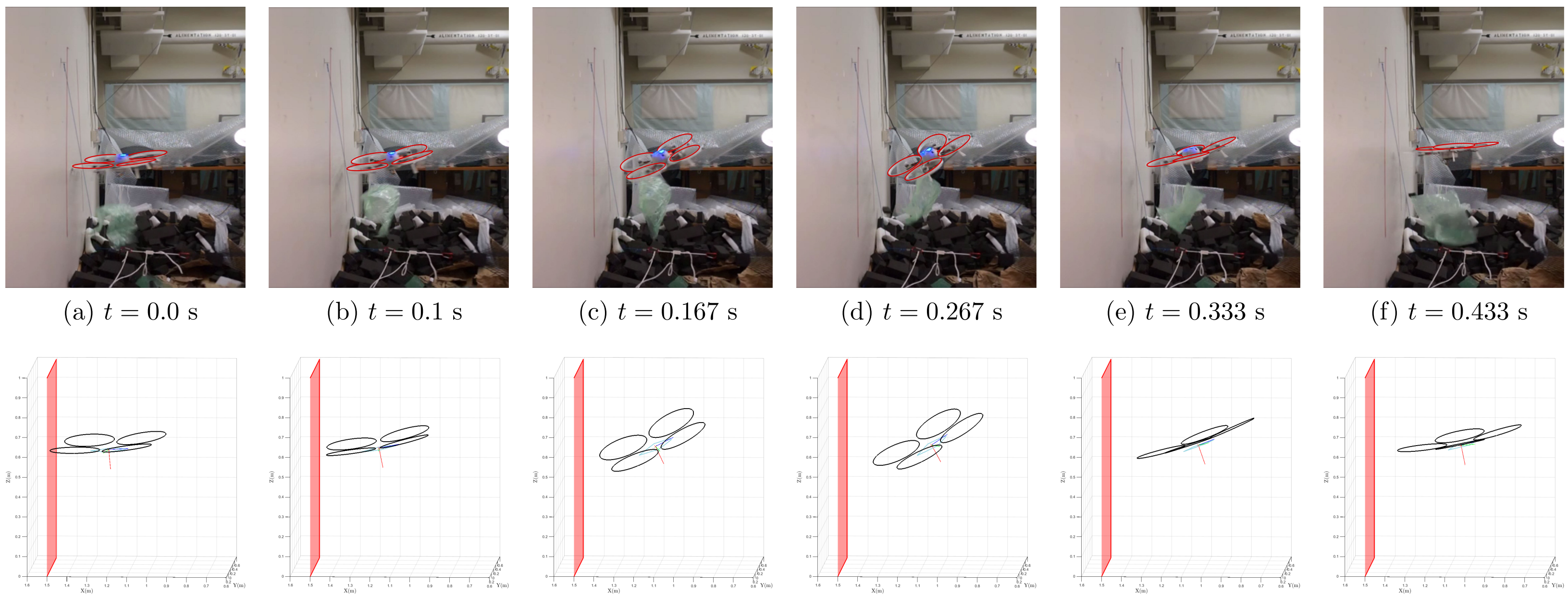

(a) $t = 0.0$ s (b) $t = 0.1$ s (c) $t = 0.167$ s (d) $t = 0.267$ s (e) $t = 0.333$ s (f) $t = 0.433$ s

(g) $t = 0.0$ s (h) $t = 0.133$ s (i) $t = 0.2$ s (j) $t = 0.3$ s (k) $t = 0.367$ s (l) $t = 0.467$ s

Figure 4–3: Qualitative comparison of experimental (a-f) and simulated (g-l) quadrotor response with matching initial impact conditions for Trial N-11, exhibiting a Toward Small (TS) response. The bumper outside edges are approximately outlined in the experimental response (a-f) for clarity. Time after first contact is indicated in the subfigure captions. Images (a) and (f) mimic the initial collision conditions, (b-d) and (h-j) show the pitching into the wall of a TS collision, and (e-f) and (k-l) show the high level controller re-orienting the quadrotor to a level attitude.

4.3 Experimental Validation Summary

Experimental testing with the Spiri platform uncovered additional considerations for successful recovery control, aside from the controller itself. Given the collision recovery problem defined in Section 1.3, the quadrotor must have full control of its four thrusters after the collision, and therefore must have bumpers that do not deform to a point where the propeller motion is halted and the motor shuts down. Because of this requirement, Navi is a more suitable collision recovery platform, as its bumpers are stiffer and have larger radii. However, there were still experimental trials using Navi where the bumper deflection disturbed the propeller motion, but did not completely stop their rotation. This is because Navi's ESCs allow for some resistance against the motor rotation. However, the ideal platform would have no propeller disturbance during contacts with the wall.

As the purpose of the quadrotor contact dynamics model is to provide a tool for developing recovery control, correspondence between the experimental tests and their reconstructed simulated collisions is indeed only important until the recovery controller engages. Because recovery needs to start as soon after the first contact as possible, and the qualitative correspondence durations well surpass the first contact durations, it can be seen that the contact model is capable of capturing real-life collision responses for the necessary period after first contact. This capability, along with the logical responses seen in Chapter 3, makes the simulation of the quadrotor contact dynamics model a good tool for recovery control development and validation, and will be used for these purposes in Chapter 5.

CHAPTER 5
Quadrotor Collision Recovery

The array of quadrotor responses to different initial collision conditions in Chapters 3 and 4 was examined critically to form an overall control strategy which addresses the quadrotor collision recovery problem, as defined in Section 1.3. Although the responses observed can be generally categorized, the dynamic collisions are still random and not fully predictable in nature, and must be handled by the control strategy presented in Sections 5.1 to 5.4. The components of this strategy, and the strategy as a whole, are verified in Sections 5.5 and 5.6 respectively. In algorithms implemented on the Navi experimental platform for live demonstrations of quadrotor collision recovery, estimated values are denoted with a hat (e.g., $\hat{\mathbf{q}}$) and measured values are given a tilde (e.g., $\tilde{\mathbf{a}}_{acc}$).

5.1 Overall Control Strategy

Three consecutive phases of the Collision Recovery Pipeline (CRP) shown in Figure 5–1 attempt to transform the quadrotor from a state of being unaware of the collision, to being recovered a safe distance away from the wall. The first phase — Collision Identification, detects the collision has occurred, and estimates the wall normal vector to provide a recovery direction for the remaining phases. After the collision has been detected, the second phase — Collision Characterization, uses a FLP to transform four collision response indicators into a single value that characterizes the quadrotor response: *Collision Response Intensity* (CRI). This CRI characterization is then sent to the final phase — Re-orientation Control, which maps the CRI to a reference acceleration control input $\mathbf{a}_{ref}$, and returns the quadrotor to stable flight. The first and second phases of the pipeline are presented and examined in detail in the remainder of this chapter. The third phase is the primary focus of Dicker's work [47],

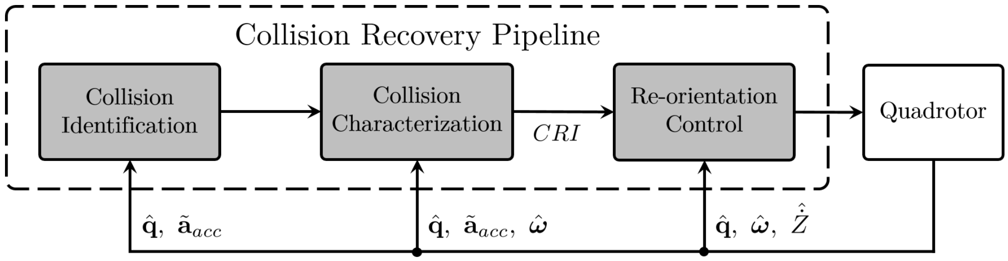

Figure 5–1: Collision Recovery Pipeline and quadrotor plant

and therefore only a brief summary of Re-orientation Control is provided in Section 5.4, with more details available in [54].

A FLP-based characterization followed by a CRI-to-$\mathbf{a}_{ref}$ mapping is used over FLC to directly compute a control signal, allowing for more intuitive validation of the proposed system. The array of collision responses observed in Chapters 3 and 4 make validating a response intensity more straightforward than validating a reference acceleration.

An important consideration for the overall control strategy is the CRP response time, from when the collision begins at t_C, to when Re-orientation Control first engages to begin stabilizing the quadrotor. In Chapters 3 and 4, it was demonstrated that intense collisions can cause the quadrotor to spin out of control as its angular momentum increases over time, so the pipeline response time should be as short as possible. However, the four indicators of collision response used in Collision Characterization are more informative when they are calculated later, rather than sooner. A good compromise between the two opposing persuasions is to have a response time less than or equal to the duration of first bumper contact, as the quadrotor generally has not lost total control at this time. Thus, for the Navi experimental platform, the maximum response time $\Delta t_{R,MAX}$ is approximately 50 ms according to Table 4–3.

5.2 Collision Identification

The CRP is triggered by an accelerometer-based collision event detection. As soon as the collision is detected, the wall normal direction is estimated, for use in both the Collision

Characterization and Re-orientation Control phases. The Collision Identification phase is general to all propeller protected UAVs, given normal free-flight accelerometer readings are not unreasonably noisy. On Navi, the accelerometer noise during free-flight can be characterized by zero mean Gaussian noise with the covariance matrix $\mathbf{Q}_{acc}$:

$$\mathbf{Q}_{acc} = \begin{bmatrix} 1.33 & 1.92 & 0.11 \\ 1.92 & 5.94 & 0.76 \\ 0.11 & 0.76 & 1.28 \end{bmatrix} \ \mathrm{m/s^2} = \begin{bmatrix} 0.13 & 0.20 & 0.01 \\ 0.20 & 0.61 & 0.08 \\ 0.01 & 0.08 & 0.13 \end{bmatrix} \ \mathrm{g}$$

where the first, second, and third diagonal entries are the variance of the x, y, and z sensing axes respectively. This matrix was computed with high-pass filtered accelerometer measurements using a 10 Hz cut-off frequency.

5.2.1 Collision Detection

Since the collision is with a vertical wall, spikes in horizontal acceleration are monitored. To estimate the horizontal acceleration, the accelerometer measurement $\tilde{\mathbf{a}}_{acc}$ is rotated into the inertial frame, and compensated with gravity $\mathbf{g}$ as:

$$\hat{\mathbf{a}} = \hat{\mathbf{q}} \odot \tilde{\mathbf{a}}_{acc} + \mathbf{g} \tag{5.1}$$

where $\mathbf{a} = [a_X \ a_Y \ a_Z]$ is the vehicle CM acceleration in $\mathcal{F}_I$. Then, the collision is detected at the time t_D, when the magnitude of the inertial acceleration horizontal components reaches a threshold:

$$\text{Collision Detection Flag} = \begin{cases} 1, \ \text{if} \ \left\| \left[\hat{a}_X, \ \hat{a}_Y \right]^T \right\| > 1 \text{ g} \\ 0, \ \text{otherwise} \end{cases} \tag{5.2}$$

where the threshold of 1 g may need to be increased for platforms with noisier normal free-flight accelerometer readings, but is still suitable for platforms with accelerometer readings less noisy than, or comparable, to those of Navi.

For less intense collisions, the full CRP can run to completion while the quadrotor is still in contact with the wall, whence an additional collision would be detected, and the CRP would be unnecessarily engaged again. To prevent this, the Collision Detection Flag can only be changed from 0 to 1 once per horizontal acceleration spike, and is set to 0 upon successful recovery.

5.2.2 Wall Normal Estimation

At t_D, the wall normal is also estimated by the variable $\hat{\mathbf{e}}_N$ as follows:

$$\hat{\mathbf{e}}_N = [\hat{a}_X,\ \hat{a}_Y]^T \ / \left\| [\hat{a}_X,\ \hat{a}_Y]^T \right\| \tag{5.3}$$

It should be noted that even with perfect accelerometer readings (as provided in simulation), this wall normal estimation $\hat{\mathbf{e}}_N$ is not perfectly equal to $\mathbf{e}_N$ in most situations, when the quadrotor pre-collision direction of horizontal motion is not exactly $-\mathbf{e}_N$, and the pre-collision inclination is non-zero. In these situations, the thrusters of the under-actuated quadrotor are not pointing strictly upwards, and generate vehicle acceleration components in the $\mathbf{e}_N$ and $\mathbf{e}_T$ directions. Any accelerations in the $\mathbf{e}_T$ direction are largely unaffected by the contact force, are still present at t_D, and are captured in (5.3). This means that the estimate $\hat{\mathbf{e}}_N$ is always directed away from the wall, but likely not exactly normal to it (i.e., when $\hat{\mathbf{e}}_N = \mathbf{e}_N$). This situation is further complicated when the accelerometer is not coincident with the location of the quadrotor CM; when the accelerometer is closer to the wall than the CM at the impact configuration, $\hat{\mathbf{e}}_N$ is closer to $\mathbf{e}_N$ than if the accelerometer were located at the CM, and conversely $\hat{\mathbf{e}}_N$ deviates more from $\mathbf{e}_N$ when the accelerometer is farther from the wall than the CM. To correct for this using rigid body kinematics, (5.1) can be augmented as:

$$\hat{\mathbf{a}} = \hat{\mathbf{q}} \odot \tilde{\mathbf{a}}_{acc} + \mathbf{g} + \dot{\hat{\mathbf{\Omega}}}^{\times}\big(\hat{\mathbf{q}} \odot (-\mathbf{r}_S)\big) + \hat{\mathbf{\Omega}}^{\times}\Big(\hat{\mathbf{\Omega}}^{\times}\big(\hat{\mathbf{q}} \odot (-\mathbf{r}_S)\big)\Big) \tag{5.4}$$

where $\mathbf{r}_S$ is the accelerometer relative position to the CM in $\mathcal{F}_Q$, and the angular velocity and acceleration are represented in $\mathcal{F}_I$ as $\hat{\boldsymbol{\Omega}} = \hat{\mathbf{q}} \odot \hat{\boldsymbol{\omega}}$ and $\dot{\hat{\boldsymbol{\Omega}}} = \hat{\mathbf{q}} \odot \dot{\hat{\boldsymbol{\omega}}}$ respectively. Then, the wall estimation continues normally using (5.3). However, the use of (5.4) relies on an accurate knowledge of $\mathbf{r}_S$. When this relative position is small, the additional noise and uncertainty associated with using this rigid body kinematics correction reduces any potential accuracy improvement on the $\mathbf{a}$ estimation. The collision detection in (5.2) is largely unaffected by the accelerometer location, therefore $\hat{\mathbf{a}}$ from (5.1) is still used in (5.2).

5.3 Collision Characterization

The Collision Characterization phase shown in Figure 5–2 provides an estimate of the control effort required to successfully recover from the collision. Following t_D, four indicators of collision response are calculated with on-board sensor data. These indicators are then used as inputs to a FLP (thus, the terms 'collision response indicator' and 'FLP input' are used interchangeably), which outputs the CRI. The indicator calculation times specified in Section 5.3.1 and the FLP parameters in Section 5.3.3 were chosen and tuned for the Navi experimental platform, but adjustments can easily be made to these values for use on other propeller protected quadrotors.

The choice of using type-2 Mamdani fuzzy logic [37] to characterize the response provides a flexible and robust method for weighting the four indicators to produce a single value that can be intuitively mapped for use by the Re-orientation Control phase. Using a FLP is flexible in that parameters can be easily tuned and adjusted for other platforms, and is robust in that it can characterize a collision with any initial conditions — a challenging task given their unexpected and unpredictable nature. A FLP also does not require explicitly using the dynamics model of the collision, or estimation of unmeasurable model states, making it suitable for live implementation on any standard quadrotor platform (i.e., with only IMU sensing). Designing and tuning the FLP inputs and parameters requires 'expertise', which was gained by studying correlations between simulated sensor data and quadrotor response.

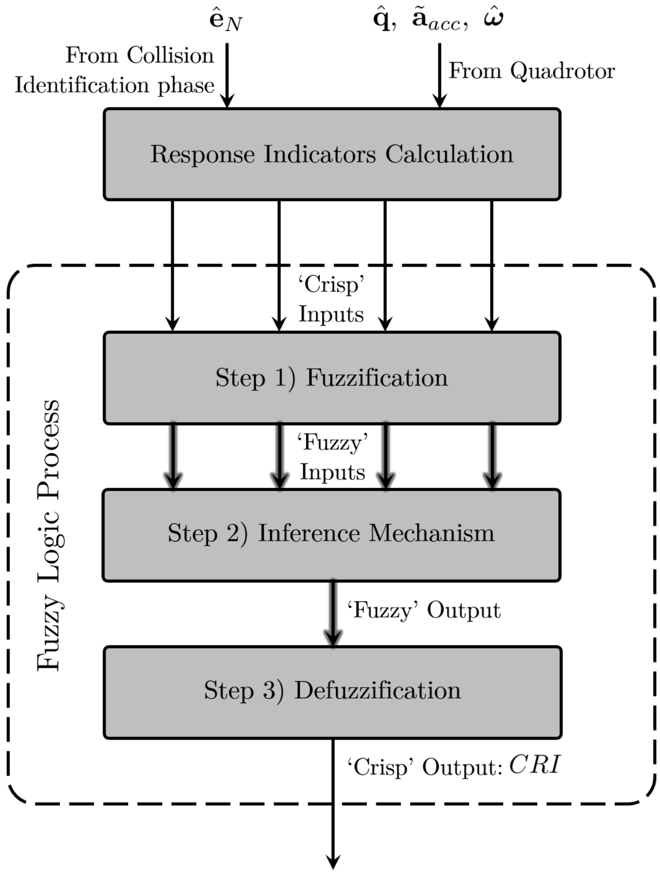

Figure 5–2: Collision Characterization phase

5.3.1 Collision Response Indicators

The four collision response indicators were chosen based on the contact model simulation findings described in Section 3.6. Indicators can be calculated simultaneously, however the effectiveness of each indicator depends on when they are taken, as described in Section 5.1. The calculation times were chosen to be as short as possible, while still providing enough information for the FLP, and are specified for the four indicators below. The calculation times for indicators 2 to 4 can be tuned along with the FLP parameters in Section 5.3.3 for collision characterization of other quadrotors.

1) Pre-collision Inclination

The *pre-collision* inclination can be estimated with (3.1), where the element $\mathbf{e}_T$ is calculated in (2.9) with the estimated wall normal $\hat{\mathbf{e}}_N$ from (5.3), using $\hat{\mathbf{a}}$ from (5.1). The element $\mathbf{e}_z^I$ is calculated in (3.2) with the estimated attitude $\hat{\mathbf{q}}$. This quaternion must be stored from a few estimation samples before t_D; specifically, the $\hat{\mathbf{q}}$ value captured 2 samples before t_D is used for the live implementation. Since $\hat{\mathbf{q}}$ is saved from before the collision, and $\hat{\mathbf{e}}_N$ is available at t_D, this first indicator can be generated at t_D.

2) Acceleration x and y Components Magnitude

This FLP input is a direct indicator of the collision normal force magnitude, and therefore an implicit indicator of the collision velocity. It is the magnitude of the body-fixed x and y components of $\tilde{\mathbf{a}}_{acc}$: the raw measurement of acceleration experienced by the IMU. It is calculated 8 ms after t_D.

3) Flipping Direction Angle

The flipping direction angle η indicates if the quadrotor is flipping toward or away from the wall. The angle is between $\hat{\mathbf{e}}_N$ and the horizontal flipping direction $(\hat{\mathbf{q}} \odot \hat{\boldsymbol{\omega}})^{\times}\mathbf{e}_Z$:

$$\eta = \cos^{-1}\left(\frac{\hat{\mathbf{e}}_N^T\big((\hat{\mathbf{q}} \odot \hat{\boldsymbol{\omega}})^{\times}\hat{\mathbf{e}}_Z\big)}{\big|\big|(\hat{\mathbf{q}} \odot \hat{\boldsymbol{\omega}})^{\times}\hat{\mathbf{e}}_Z\big|\big|}\right) \tag{5.5}$$

With perfect sensing and wall normal estimation, η would indicate the flipping direction as follows:

$$\text{Flipping direction} = \begin{cases} \text{Toward wall,} & \text{if } \eta > 90^\circ \\ \text{Away from wall,} & \text{if } \eta \leq 90^\circ \end{cases} \tag{5.6}$$

Since it is the direction, and not magnitude of $\hat{\boldsymbol{\omega}}$ that is pertinent, and $\hat{\mathbf{e}}_N$ is available at t_D, η is calculated 8 ms after t_D.

4) Angular Velocity x and y Components Magnitude

This last input is an indicator of the quadrotor's flipping motion, as larger x and y angular velocity components are seen when the vehicle spins out of control. The indicator is simply $\left|\left|[\hat{p} \quad \hat{q}]^T\right|\right|$, and is taken 12 ms after t_D, which is the greatest among all indicator calculation times. This indicator is a magnitude that increases over time, and angular velocity is less reactive to the collision than acceleration, which is measured for indicator 2 at 8 ms after t_D.

5.3.2 Characterization Output: Collision Response Intensity

The output of the Collision Characterization phase is the CRI, a numerical value on a scale from -1 to 1. Negative CRI values characterize the quadrotor collision response as flipping away from the wall, while positive CRI values characterize the response as flipping towards the wall. A larger CRI magnitude represents a more intense response: the quadrotor spins out of control more rapidly and is more difficult to recover. Figure 5–3 illustrates the immediate post-collision orientation of the quadrotor which corresponds to different values on the CRI scale.

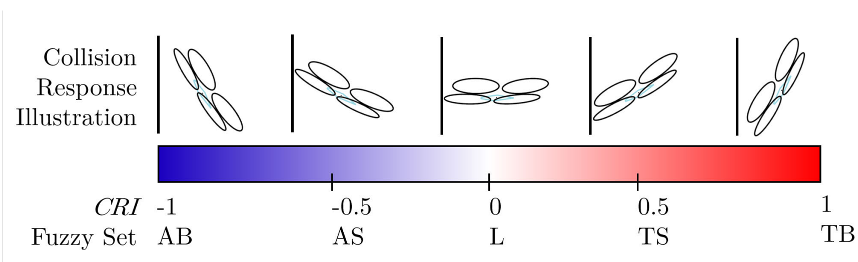

Figure 5–3: Collision Response Intensity (CRI) scale and FLP output fuzzy sets with corresponding post-collision quadrotor illustrations

5.3.3 Fuzzy Logic Process

The four indicators in Section 5.3.1 are treated as the 'crisp' or numerical inputs into the FLP. Then, the three steps of the FLP: fuzzification, inference mechanism, and defuzzification, produce the 'crisp' output, or CRI, of Section 5.3.2. The fuzzification parameters

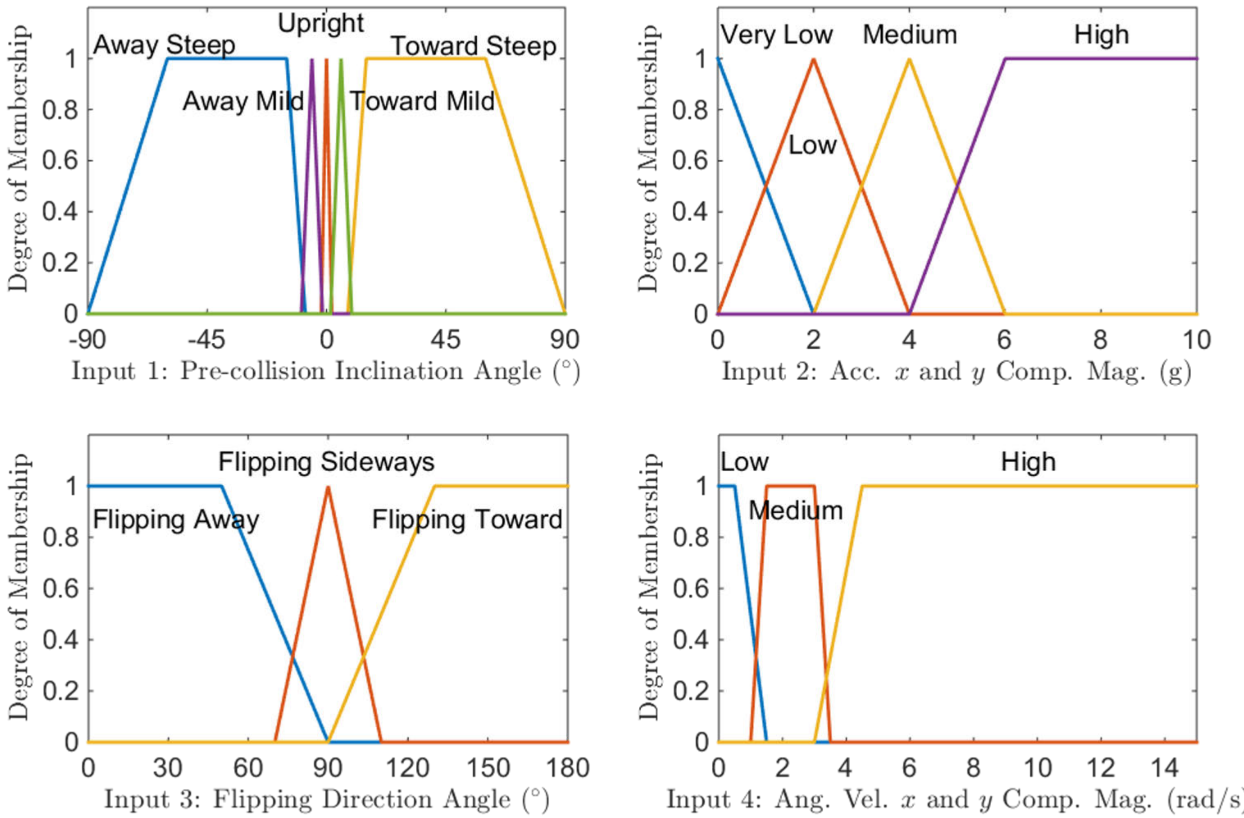

Figure 5–4: Fuzzy Logic Process input membership functions

can be easily adapted for use on other propeller protected quadrotors, while the inference mechanism and defuzzification parameters are generally usable cross-platform.

Step 1) Fuzzification

The first step in the FLP takes each of the four inputs and assigns them degrees of membership for each of the fuzzy sets, depending on the membership functions defined in Figure 5–4. For example, an Acceleration x and y Components Magnitude of 5 g would have a degree of membership of 0.5 for both the Medium and High fuzzy sets. These degrees of membership for each of the four 'crisp' inputs are now said to be the 'fuzzy' inputs. By having degrees of membership for multiple fuzzy sets, the uncertainty of the collision response indicated by an individual 'crisp' input is captured.

Triangular and trapezoidal membership functions were chosen for both the fuzzification and defuzzification steps because they are sufficient for segmenting the membership and are more computationally efficient than non-linear membership functions, which is important for real-time flight control. The specific fuzzy set definitions (i.e., where triangle and trapezoid vertices are placed) for inputs 2 and 4 are directly affected by the indicator calculation times chosen in Section 5.3.1, as these inputs are both sensor magnitudes that change over time. With the exception of input 3, all the membership functions are specific to the Navi platform, and would need to be re-tuned for collision characterization of a different platform.

Step 2) Inference Mechanism

The Mamdani-type inference mechanism turns the 'fuzzy' inputs from the first step into a 'fuzzy' output for the last step. This is done via IF-THEN rules, where certain combinations of the input fuzzy sets will result in an output fuzzy set. The degrees of membership from the fuzzification step translate to this step, where there are degrees of membership for the fuzzy output sets as well. In this inference system, two rule sets as defined in Table 5–1 are used with equal weighting, where the output fuzzy sets abbreviations are defined in Figure 5–5. The use of only rule set 1 or rule set 2 as the inference mechanism is shown to be less effective in producing an informative CRI in Section 5.5.4.

Step 3) Defuzzification

This step turns the fuzzy output degrees of membership into a 'crisp' output, via the membership function defined in Figure 5–5. Collision response correlations to the output fuzzy sets are also illustrated in Figure 5–3. These output fuzzy sets are based on, and correspond with, the collision response categories observed in Section 3.4.

5.4 Re-orientation Control Summary

The final phase of the CRP begins with a mapping of the CRI input to a quadrotor CM reference acceleration, pointing in the same direction as the estimated wall normal.

Table 5–1: Fuzzy Rule Sets

Fuzzy Rule Set 1

	Input 1				
Input 2	Toward Steep	Toward Mild	Upright	Away Mild	Away Steep
Very Low	L	L	L	L	L
Low	TS	TS	L	AS	AS
Med.	TB	TS	L	AS	AB
High	TB	TB	L	AB	AB

Fuzzy Rule Set 2

	Input 3		
Input 4	Flipping Toward	Flipping Sideways	Flipping Away
Low	L	L	L
Med.	TS		AS
High	TB		AB

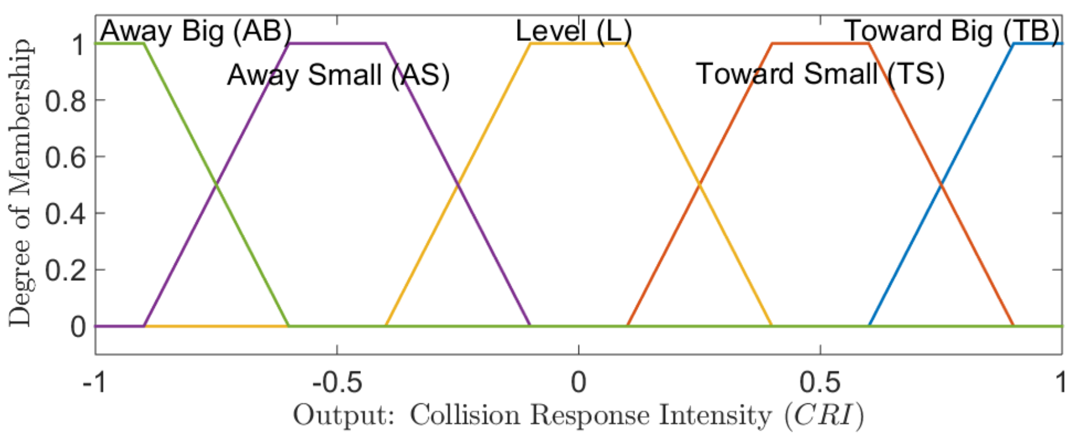

Figure 5–5: Fuzzy Logic Process output membership function

Then, two consecutive recovery stages use different algorithms to generate desired body angular velocities, which are then mapped to thruster RPMs by the attitude controller. The first stage orients the quadrotor to track the reference acceleration. Then, an upright attitude is achieved in the second stage. Vertical velocity stabilization and horizontal velocity stabilization are not attempted, as they requires additional sensing, and have already been successfully demonstrated with vison-based feedback using only on-board sensors in [6].

5.5 Collision Recovery Pipeline Phase Verifications

Verification of the Collision Identification and Collision Characterization phases is now presented using two methods: a Monte Carlo simulation, and experimental results. The phases are studied individually, with focus on the wall normal estimation $\hat{\mathbf{e}}_N$ and collision characterization CRI that are used by the final Re-orientation Control pipeline phase.

5.5.1 Monte Carlo Simulation Setup for Pipeline Phase Verification

The Monte Carlo simulation consists of 1000 trials directing Navi into a collision with a wall, not using recovery control. Only the low-level attitude controller is used before and after the collision, as described in Section 3.1.2. The Euler angles and incoming velocity are randomized to be within the ranges in Table 5–2. The upper velocity limit of 2.5 m/s was chosen since velocities greater than this may damage Navi's bumpers. Among the 1000 trials, 33 trials with prescribed low incoming velocities and initial inclinations away from the wall do not actually collide with the wall, and are not displayed in the results.

Table 5–2: Monte Carlo Simulation Initial Condition Ranges

	Range
Roll	$-15^\circ \leq \phi \leq 15^\circ$
Pitch	$-45^\circ \leq \theta \leq 45^\circ$
Yaw	$-45^\circ \leq \psi \leq 45^\circ$
Incoming Velocity	$0.5\text{ m/s} \leq \dot{X}_C \leq 2.5\text{ m/s}$

The accelerometer measurement $\mathbf{a}_{acc}$ used in the Collision Identification (for Equations 5.1 and 5.4) and Collision Characterization (for response indicator 2) phases is simulated for the sensor located at $\mathbf{r}_S = [19,\ \ 8.1,\ \ -48]^T \times 10^{-3}$ m from the CM using rigid body kinematics:

$$\mathbf{a}_S = \mathbf{a} + \dot{\mathbf{\Omega}}^{\times}(\mathbf{q} \odot \mathbf{r}_S) + \mathbf{\Omega}^{\times}\Big(\mathbf{\Omega}^{\times}(\mathbf{q} \odot \mathbf{r}_S)\Big) \tag{5.7}$$

$$\mathbf{a}_{acc} = \mathbf{q}^{-1} \odot (\mathbf{a}_S - \mathbf{g}) \tag{5.8}$$

where $\mathbf{a}_S$ is the acceleration experienced at the sensor location in $\mathcal{F}_I$, and all variables in (5.7) and (5.8) are taken to be their true values. The remaining estimated values used in the first two CRP phases are taken to be their true values as well.

5.5.2 Experimental Setup for Pipeline Phase Verification

The accelerometer and state estimation data from the 22 experiments in Chapter 4 are post-processed to obtain the Collision Identification and Collision Characterization results that would be generated were the algorithms implemented on Navi, for verifying the respective phases in Sections 5.5.3 and 5.5.4. Recall in these experiments, the quadrotor is still unaware of the collision, and no recovery control is used. The estimated quaternion $\hat{\mathbf{q}}$ and angular velocity $\hat{\boldsymbol{\omega}}$ are both provided by the PX4 state estimator.

5.5.3 Collision Identification Verification

The distribution of Monte Carlo simulation and experimental results for time to detection, $t_D - t_C$, are shown in Figure 5–6. In simulation, t_C is simply provided by when a bumper deflection ($\delta > 0$) first occurs. In experiment, t_C is determined through visually inspecting the post-processed data plot, and is the time when $\left\| \left[\hat{a}_X,\ \hat{a}_Y\right]^T \right\|$ first begins to spike. The detection times seen for both verification methods are of the same order, and are well within the maximum collision response time $\Delta t_{R,MAX}$ of 50 ms for Navi. The median

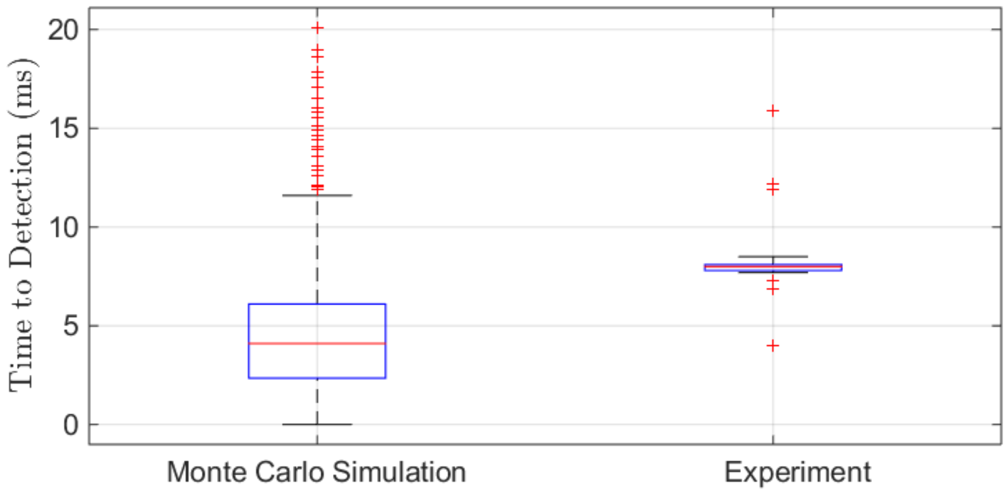

Figure 5–6: Time to detection distribution. Median value is at the red horizontal line. Values between the 25th and 75th percentiles are in the blue box. Values between the aforementioned percentiles, and the lower adjacent value and upper adjacent value respectively are on the whiskers (i.e., dashed lines). Outliers are marked with red + markers.

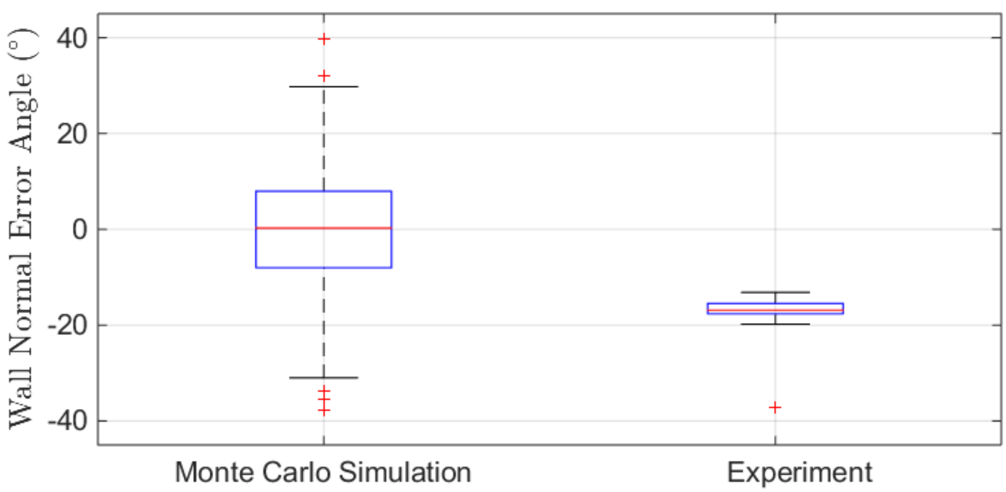

Figure 5–7: Wall normal error angle distribution. Distribution is marked according to description for Figure 5–6.

values are 4.1 ms and 8.0 ms for the Monte Carlo simulation and experimental results respectively. The spread seen in experiment is much lower because the number of trials and the range of initial conditions is lower.

Distribution of the wall normal error angle (i.e., $\cos^{-1}(\mathbf{e}_N^T \hat{\mathbf{e}}_N)$) is in Figure 5–7, for both verification methods. The median error angle of 0.27° for the Monte Carlo simulation is close to zero, as expected. The median experiment error angle of −17° is a result of collisions occurring at $\psi =$ 10° on average (shown in Table 4–3), which introduces a $-Y$ component CM acceleration at t_D, and error into $\hat{\mathbf{e}}_N$. The heading standard deviation about the mean $\psi =$ 10° is low, so the experimental data spread is lower. Given the angle errors observed in Monte Carlo simulation and experiment, confidence is gained that the wall normal estimation method generates a $\hat{\mathbf{e}}_N$ directed *away* from the wall.

5.5.4 Collision Characterization Verification

Distribution of the four FLP input values, calculated according to Section 5.3.1, is shown in Figure 5–8 for the Monte Carlo simulation. The estimated pre-collision inclination angle is within −45° to 45°, in accordance with the simulation initial attitude ranges in Table 5–2. Comparing the FLP input distributions to the membership functions in Figure 5–4, the collision responses are estimated to be mainly flipping away or towards the wall, with very few flipping sideways. Also, the magnitudes of inputs 2 and 4 stay within the ranges specified by the membership functions.

The average FLP inputs and corresponding CRI are presented in Table 5–3 for the same two experimental trial sets as defined in Chapter 4, Table 4–3. Recall that in the first set of collisions (N-1 to N-7), the vehicle experienced negative initial inclination angles, and in the second set (N-8 to N-22), Navi experienced positive initial inclination angles. As expected for the first trial set, the FLP estimates negative pre-collision inclination values (mean FLP input 1 is −4.3°), a response flipping away from the wall (mean FLP input 3 is $63° \leq 90°$),

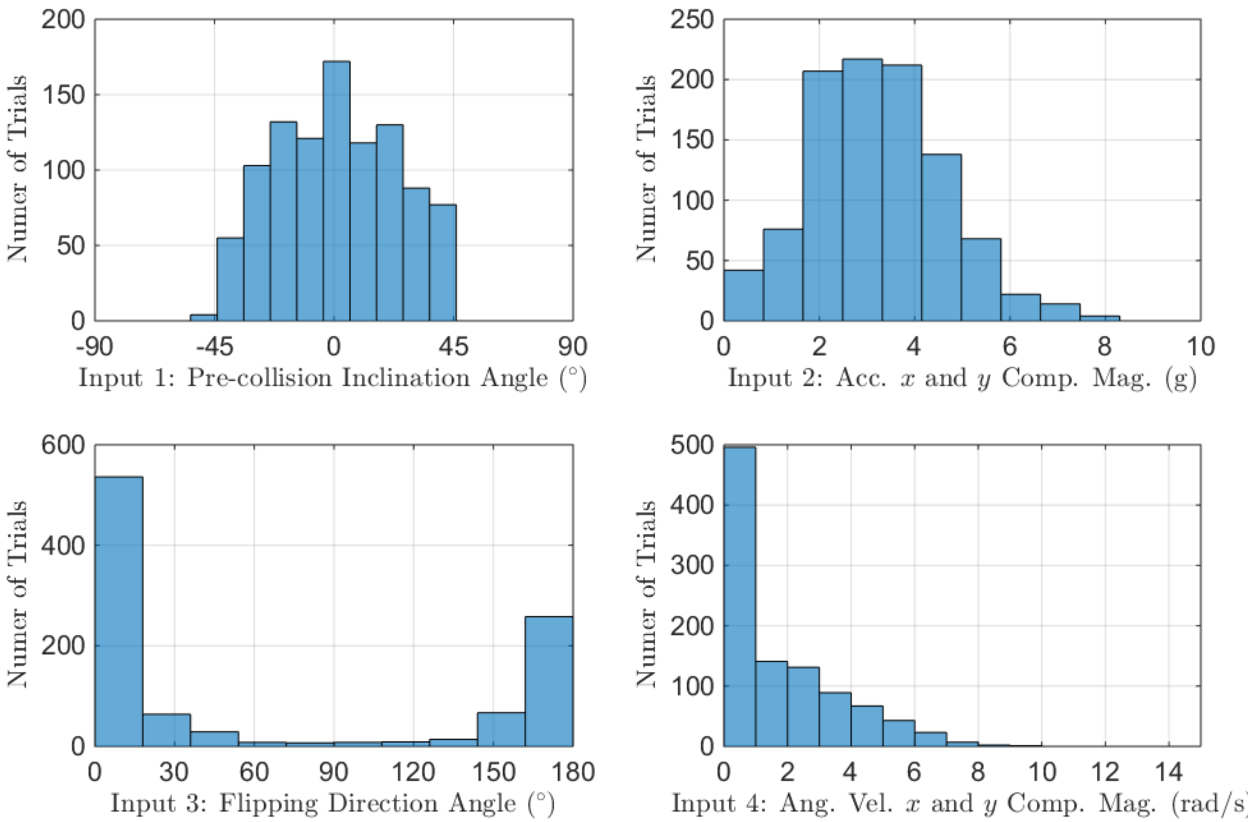

Figure 5–8: Fuzzy Logic Process 'crisp' inputs in Monte Carlo simulation

Table 5–3: Collision Characterization Experimental Results

Trial Set	Value	FLP input 1 (°)	FLP input 2 (g)	FLP input 3 (°)	FLP input 4 (rad/s)	CRI
N-1 to N-7	Mean	-4.3	5.2	63	0.55	-0.23
	Std. Dev.	2.5	1.1	54	0.25	0.11
N-8 to N-22	Mean	5.7	6.2	102	0.79	0.29
	Std. Dev.	2.6	0.90	55	0.48	0.12

and a negative CRI value (mean is -0.23). Also as expected for the second trial set, the collision characterization method estimates positive pre-collision inclination angles (mean FLP input 1 is 5.7°), a response flipping towards the wall (mean FLP input 3 is $102° > 90°$), and a positive CRI value (mean is 0.29). FLP inputs 2 and 4 with mean values of 5.2 g and 0.55 rad/s respectively are slightly lower for the first set, compared to 6.2 g and 0.79 rad/s respectively for the second set, as the second set experienced slightly higher average collision speeds and inclination angle magnitudes.

Figure 5–9 plots the CRI against $||\boldsymbol{\omega}_{xy}||_{PEAK}$, introduced in Section 3.3. Monte Carlo simulation results are presented for the FLP using three different combinations of the inference mechanism rule sets in Table 5–1: both rule sets, only rule set 1, and only rule set 2. Using both rule sets, larger horizontal body angular velocities are measured for collisions with a higher CRI magnitude. This trend is much weaker when only one rule set is used; thus, the final FLP inference mechanism makes use of both rule sets, weighted equally. Figure 5–9a shows that the CRI output from the Collision Characterization phase is a suitable measure of post-collision quadrotor response that can be used by the re-orientation controller.

The $||\boldsymbol{\omega}_{xy}||_{PEAK}$ versus CRI are plotted in Figure 5–10 for the experimental results, using the corresponding rule set combinations in the FLP inference mechanism as plotted in Figure 5–9. Using both rule sets, the Monte Carlo simulation trend is followed with the exception of two trials, as seen by comparing Figures 5–9a and 5–10a. The two outlying trials have relatively high $||\boldsymbol{\omega}_{xy}||_{PEAK}$ values, despite the zero CRI characterization, because the high level PX4 position controller on the experimental platform redirects the vehicle into the wall after the initial mild collision. Using rule set 1 only, shown in Figure 5–10b, the Monte Carlo simulation trend is also followed with the exception of three trials with near zero CRIs and non-zero $||\boldsymbol{\omega}_{xy}||_{PEAK}$ values, for the reasoning already stated for Figure 5–10a. Using rule set 2 only, all trials follow the Monte Carlo simulation trend, as seen in Figure 5–10c. While the quantity and range of experimental trials does not provide enough evidence

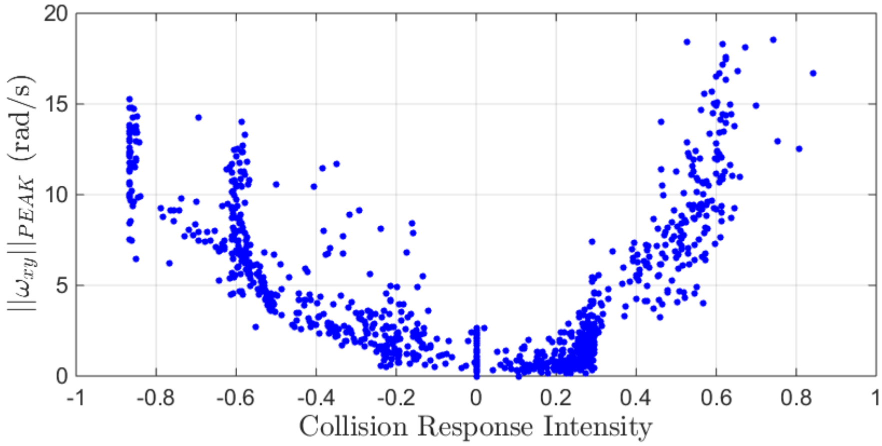

(a) Both rule sets

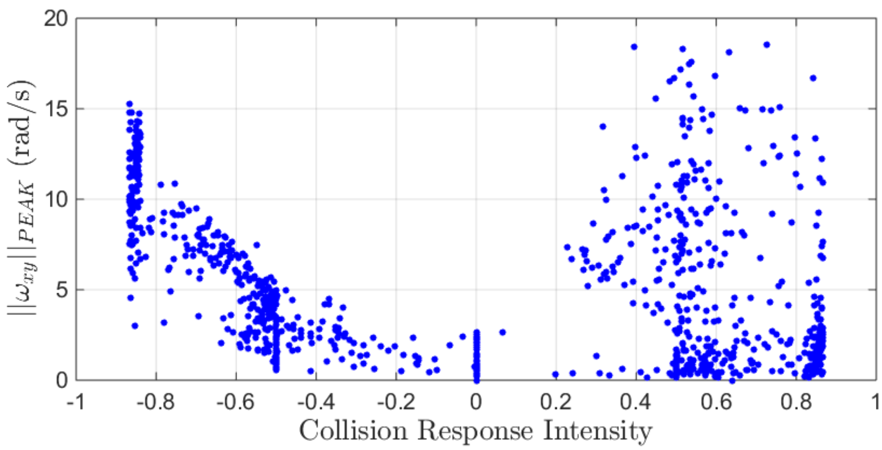

(b) Rule set 1 only

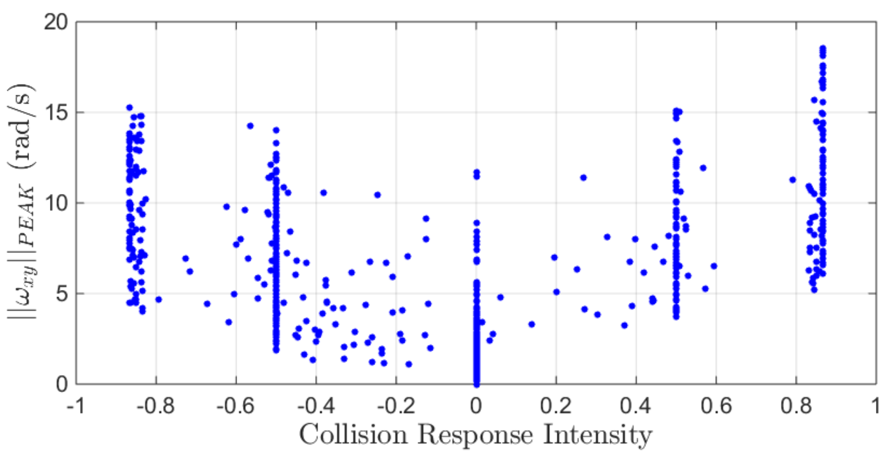

(c) Rule set 2 only

Figure 5–9: $||\boldsymbol{\omega}_{xy}||_{PEAK}$ versus Fuzzy Logic Process 'crisp' output: *Collision Response Intensity* (CRI) in Monte Carlo simulation, for three different inference mechanism rule set combinations, as labelled in subfigure captions.

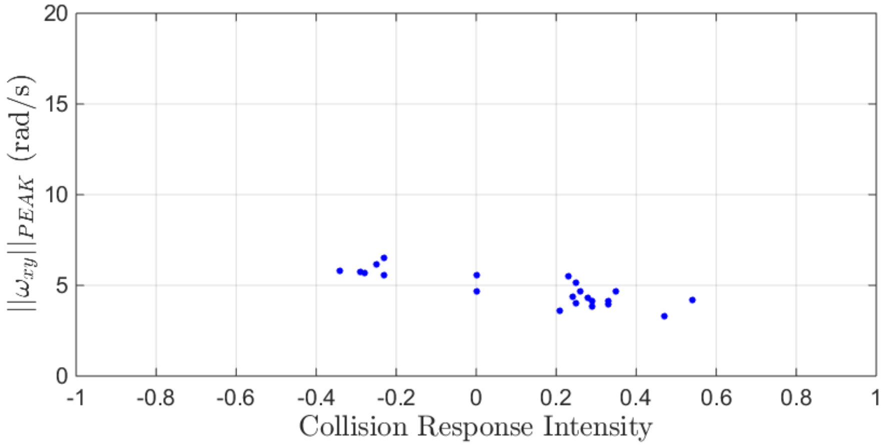

(a) Both rule sets

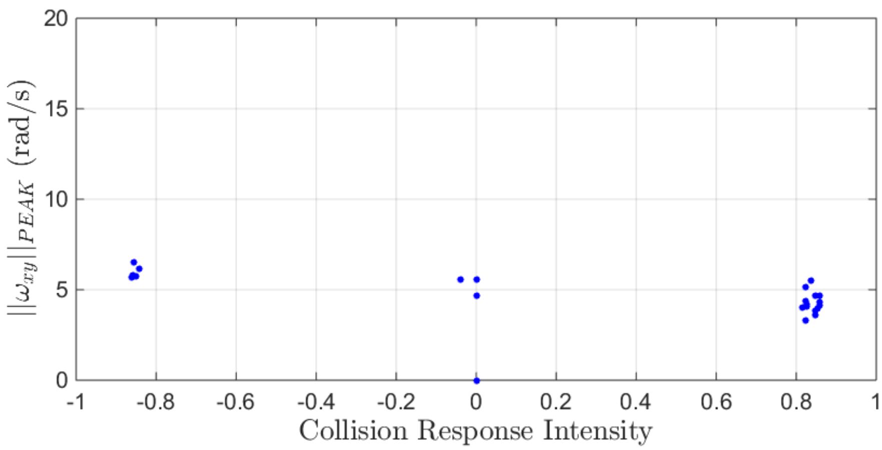

(b) Rule set 1 only

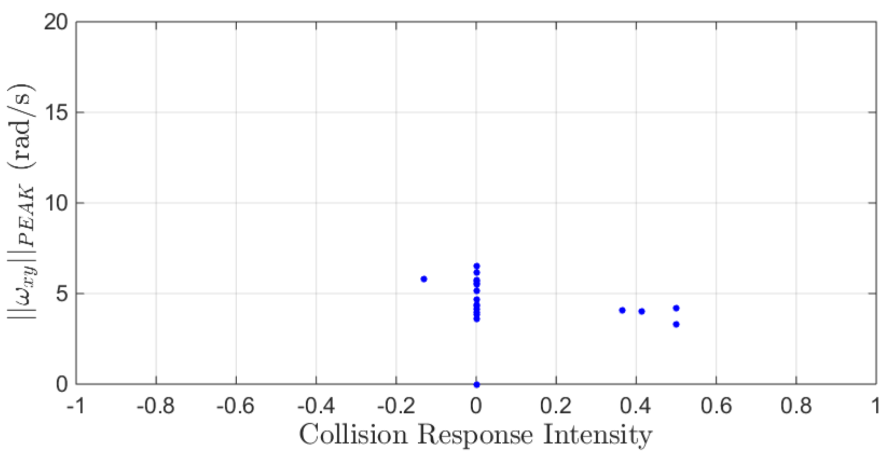

(c) Rule set 2 only

Figure 5–10: $||\boldsymbol{\omega}_{xy}||_{PEAK}$ versus Fuzzy Logic Process ‘crisp’ output: *Collision Response Intensity* (CRI) in experiment, for three different inference mechanism rule set combinations, as labelled in subfigure captions.

to validate the CRI computation experimentally, the comparison of measured $||\boldsymbol{\omega}_{xy}||_{PEAK}$ values to generated CRI outputs is able to confirm using both rule sets in the inference mechanism provides the best collision characterization for use in the CRP.

5.5.5 Collision Recovery Pipeline Response Time

Experiments show the FLP calculation only takes one controller time step ($\sim$ 4 ms) on Navi's Pixhawk hardware, making the total duration of the Collision Characterization phase 16 ms (recall the longest FLP input calculation duration is 12 ms). Combined with the median experimental Collision Identification phase duration of 8 ms shown in Figure 5–6, and the negligible time between the CRI being generated to the recovery controller engaging, the experimental CRP total response time for Navi is on average $\sim$ 24 ms, well under $\Delta t_{R,MAX} = 50$ ms.

5.6 Full Collision Recovery Pipeline Verification

Now, the impact of the Collision Identification and Collision Characterization phases on the full CRP of Section 5.1 is studied with additional Monte Carlo simulations and experiments. The CRP in both simulation and experiment use the Re-orientation Control phase by Dicker [47, 54].

5.6.1 Collision Recovery Pipeline Parameters

For both the Monte Carlo simulations and experiments, two trial sets are performed using two variations of the CRP after t_C. The first trial set includes the FLP-based Collision Characterization Phase in the CRP, as presented in Section 5.3, and the second trial set omits this phase. This is done to study the importance of the characterization on quadrotor recovery control. Collision detection from the Collision Identification Phase is still used in both simulations, as it is required for any type of quadrotor recovery. By omitting the Collision Characterization phase, the second simulation leaves out the first recovery stage described in Section 5.4, skipping to the second recovery stage that prescribes an upright orientation, independent of the CRI value.

The simulated and experimental trial sets with characterization use the following CRI-to-$\mathbf{a}_{ref}$ mapping in the first recovery stage [47]:

$$\mathbf{a}_{ref} = \begin{cases} 0.75 \cdot g \cdot CRI \cdot \hat{\mathbf{e}}_N & , \text{ if } CRI \geq 0 \\ \mathbf{0} & , \text{ otherwise} \end{cases} \tag{5.9}$$

where the control input $\mathbf{a}_{ref}$ is the desired quadrotor CM acceleration. A higher $\mathbf{a}_{ref}$ magnitude generates an attitude setpoint deviating more from the upright orientation, and a zero $\mathbf{a}_{ref}$ magnitude corresponds to the upright orientation.

5.6.2 Monte Carlo Simulation Setup for Full Pipeline Verification

Two Monte Carlo simulations are performed, each consisting of 1000 trials. Sections 5.6.4 to 5.6.6 present results for the trials that provide initial conditions resulting in collisions: 957 of 1000 trials for the simulation with Collision Characterization, and 966 of 1000 trials for the simulation without Collision Characterization. The same simulation conditions as the Monte Carlo simulation performed in Section 5.5 for the individual CRP phase verifications (listed in Table 5–2) are used. The sensor measurements are also simulated according to the Monte Carlo simulation setup in Section 5.5.1, using (5.8) for the accelerometer measurement, and all estimated values taken to be their true values. In these recovery simulations, the quadrotor is allowed to stabilize itself using infinite height (i.e., the quadrotor cannot crash), and the recovery is considered to be a failed case if the CRP does not complete within 3 seconds.

5.6.3 Experimental Setup for Full Pipeline Verification

For the full CRP verification, two additional experimental sets were performed with the pipeline implemented and operating on Navi. The pre-collision experimental setup for these verifications is similar to that for the contact dynamics model verification trials with the Navi quadrotor, as described in Section 4.2.2. Navi is directed into the wall with starting and target setpoints fed into the PX4 position controller. After the CRP completes, manual control is returned to the pilot, who lands the vehicle. Aside from the top-view high-speed camera, all other data with their associated recording rates from column two of Table 4–1 were recorded.

To improve the position control performance over the trials in Section 4.2, the complementary filter gains for Vicon motion capture were set to the maximum recommended value. Additional deviations from Section 4.2.2 include removing use of the barometer data for the altitude estimate, and using Vicon motion capture attitude data instead of magnetometer data in the attitude estimate, which enabled more reliable heading control when directing Navi into the wall. The attitude estimate is used by both the PX4 attitude controller before the collision and the CRP. This means that the CRP was not completed using strictly on-board sensing. However, the CRP was completed with strictly on-board sensing in a previous trial set with different PX4 position controller parameters that resulted in less exact position control. For the trials presented in the thesis, it was therefore decided that repeatability over the two trial sets was more important than using strictly on-board sensing, which was already demonstrated.

The CRP is implemented on the PX4 firmware such that each phase runs on a separate node/thread, and inter-node communication is achieved through messages, which are recorded at 250 Hz. The collision detection time, t_D, and CRP completion time from these recorded messages, in conjunction with the PX4 position, linear velocity, and attitude estimation data at 250 Hz, are used to generate the results in Sections 5.6.4 to 5.6.6.

Trials were ordered such that the same trial number between the two experimental sets had the same starting and target position setpoints, generating similar initial collision conditions for comparison. Half the trials were performed with a collision heading of $\psi = 0°$, and the remaining had a collision heading of $\psi = 45°$. For the first set with Collision Characterization, 51 trials were completed, while only 42 trials were completed for the second set without Collision Characterization before all bumpers were damaged by the repeated collisions. For the purposes of comparing the two experimental sets, only results for the 42 trials with the similar initial conditions are presented below. On average, the quadrotor was given 0.7 m in height to complete the CRP. If the quadrotor crashed into the net during recovery, it was considered to be a failed case.

Video frames of successful experimental recovery examples using the CRP with Collision Characterization are in Figure 5–11, and without it in Figure 5–12. The vehicle body and bumper outside edges are approximately outlined for clarity. As these examples have the same trial number, their initial collision conditions are similar: the experiment with Collision Characterization occurs at initial $\zeta = 9.4°$, velocity 2.0 m/s, and $\psi = 0°$, and the experiment without characterization occurs at initial $\zeta = 10.6°$, velocity 2.1 m/s, and $\psi = 0°$.

5.6.4 Recovery Success

The initial collision inclinations and X direction velocities for successful and failed recoveries using the CRP are shown in Figures 5–13a and 5–13b for the Monte Carlo simulations, with and without Collision Characterization. Both variations of the CRP have difficulty recovering the quadrotor within 3 s when the initial collision inclination is greater than 28°, creating a situation where the quadrotor is 'stuck' against the wall, and is unable to re-orient itself. There is no significant difference in the Monte Carlo simulation recovery success results using the two CRP variations, with the total recovery success rate being 93 % with characterization, and 91 % without. Successful recoveries that require more than 2 m height below the collision altitude to successfully recover are marked with a ▲ for comparison of these figures to Figures 3–3a and 3–3b, which show the same information for collisions without recovery control, where the quadrotor is only allowed 2 m to stabilize before the trial is considered to be a crash. This comparison shows that use of the CRP prevents a crash for collisions with negative initial inclinations and initial collision velocities up to 2 m/s, and generally do not prevent crashes for collisions with positive inclinations.

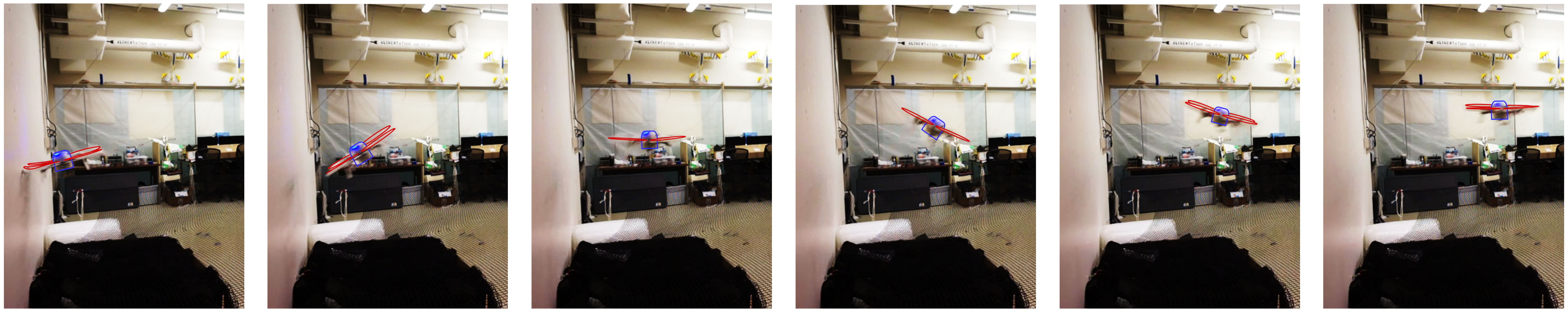

(a) $t = 0.0$ s (b) $t = 0.133$ s (c) $t = 0.267$ s (d) $t = 0.4$ s (e) $t = 0.5$ s (f) $t = 0.567$ s

Figure 5–11: Video frames of successful recovery using the CRP with Collision Characterization phase. Time after first contact is indicated in the subfigure captions. The initial collision conditions are in (a), after which the collision is detected, characterized, and $\mathbf{a}_{ref}$ is generated based on the CRI. The impact force rotates Navi to its maximum inclination in (b) before the Re-orientation Control phase takes effect. Image (c) shows Navi re-orienting towards the desired first recovery stage attitude, which is reached in (d). Images (e) to (f) show Navi re-orienting to an upright attitude during the second recovery stage, until the CRP completion in (f).

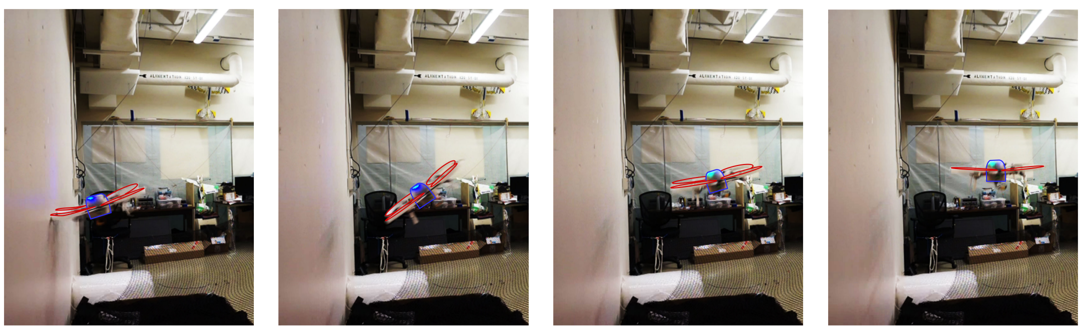

(a) $t = 0.0$ s (b) $t = 0.167$ s (c) $t = 0.3$ s (d) $t = 0.4$ s

Figure 5–12: Video frames of successful recovery using the CRP without Collision Characterization phase. Time after first contact is indicated in the subfigure captions. The initial collision conditions are in (a), after which the collision is detected. The impact force rotates Navi to its maximum inclination in (b) before the Re-orientation Control phase takes effect. Image (c) shows Navi re-orienting to an upright attitude, which is achieved in (d), and completing the CRP.

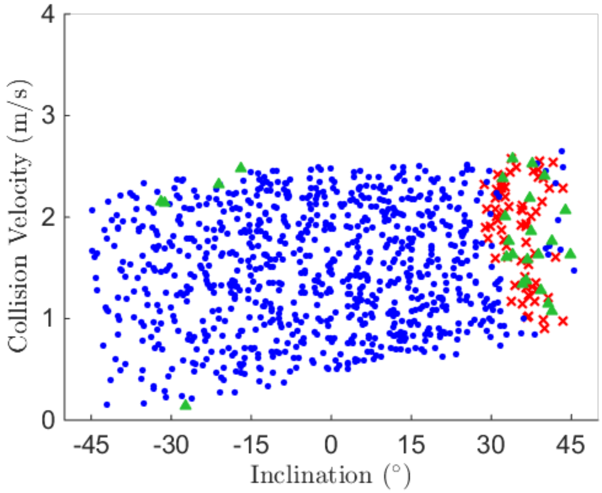

(a) Monte Carlo simulation, with Collision Characterization

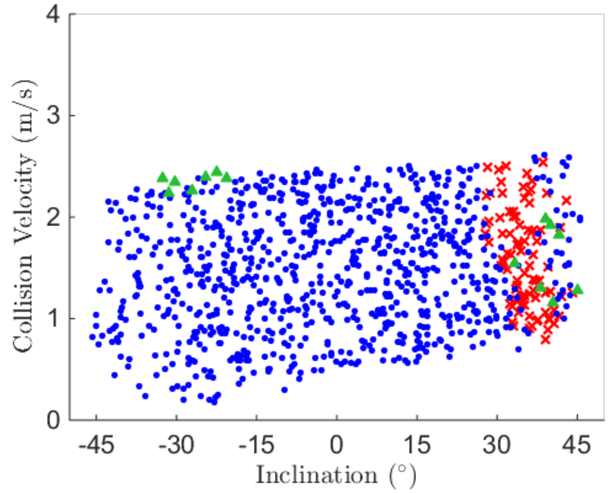

(b) Monte Carlo simulation, without Collision Characterization

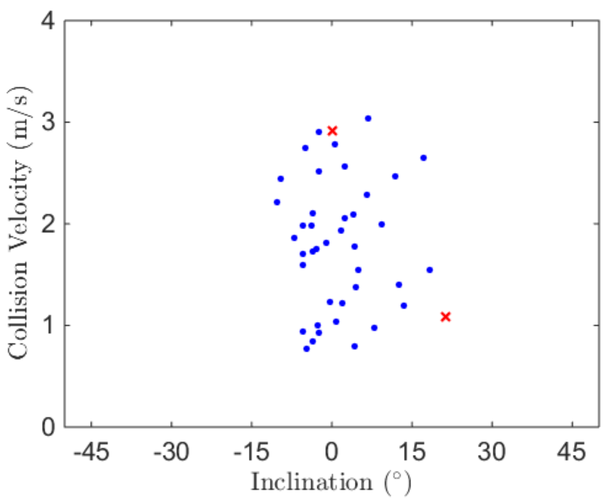

(c) Experiment, with Collision Characterization

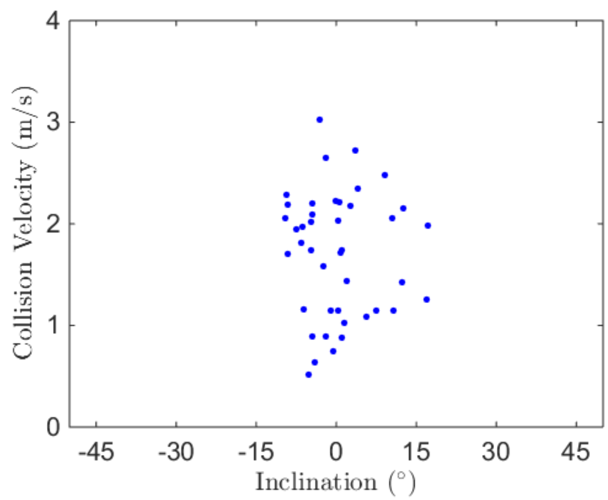

(d) Experiment, without Collision Characterization

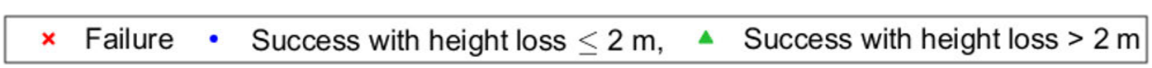

Figure 5–13: Initial collision inclinations and velocities for success and failure recovery cases. Monte Carlo simulation results are in (a-b), and experimental results are in (c-d). Collision characterization is included in the CRP for (a) and (c), and omitted for (b) and (d). Height loss is defined in Section 5.6.6.

The initial collision conditions for successful and failed experimental CRP recoveries are in Figure 5–13c and 5–13d. The range of inclinations that could be achieved under PX4 position control is much smaller than in simulation. Collision speeds greater than 2.5 m/s were achieved, and successfully recovered from, although these trials probably contributed significantly to the eventual bumper failures through fatigue and crack propagation. Out of the 42 trials, two trials failed to recover using Collision Characterization, and all trials without Collision Characterization successfully recovered. However, for both failure cases the motion capture data stopped streaming during recovery, corrupting the attitude estimate used by the Re-orientation Control phase, making these failures a result of the CRP implementation, and not its formulation. Therefore, these experimental trials show that the CRP, with or without Collision Characterization, is capable of recovering the quadrotor, with no difference in recovery percentage. In order to experimentally validate a higher range of collision inclinations, less deformable bumpers that protect the propellers from above and below would need to be used. This would remove the dependency of the experimental recovery success on bumper deformation, which is not present in the simulation trials, as the contact dynamics model does not capture propeller interference due to bumper deformation.

5.6.5 Recovery Time

The collision start time t_C is estimated to be 8 ms before t_D, recorded from the PX4 messages. The duration between t_C and the completion time of the Re-orientation Control second recovery stage is the recovery time. Distributions of recovery time for successful trials within the four validation sets are illustrated in Figure 5–14.

Median recovery times are slightly lower without Collision Characterization, as the time required to complete the first recovery stage is removed. Specifically, the median values without characterization are 0.30 s and 0.07 s for the Monte Carlo simulation and experimental results respectively, compared to 0.35 s and 0.08 s with characterization. Desired attitudes generated by (5.9) that deviate more from the hover orientation require more time to be tracked, which is reflected in the higher spread in the trial sets with Collision Characterization. Lower median values are seen in experiment, as the collision inclinations deviated less from $\zeta = 0°$, and less time is needed to achieve upright orientation. Overall, the recovery times are reasonably fast, which is important to minimize the distance travelled by the quadrotor CM during recovery.

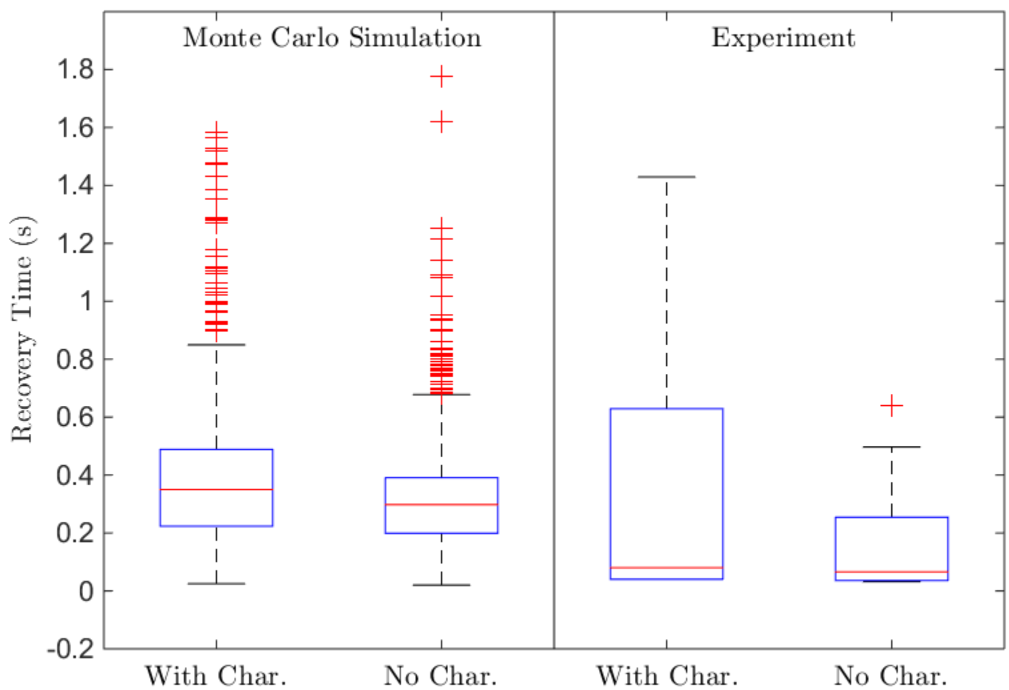

Figure 5–14: Recovery time distribution. Distribution is marked according to description for Figure 5–6.

5.6.6 Recovery Position Response

Horizontal drift is the distance the quadrotor CM moves in the XY plane from t_C to the end of recovery. Distributions of horizontal drift for successful trials within the four validation sets are in Figure 5–15. Small horizontal drift is desired if the CRP were to be used in an environment with multiple obstacles, to avoid a second collision with another obstacle (e.g., the opposite wall in a hallway). However, zero horizontal drift is also not desirable, as the quadrotor should recover a safe distance away from the wall to avoid a second collision with the same wall.

The horizontal drift values all remain within the 3.5 m × 3.5 m of open recovery area that is assumed to be available in Section 1.3. The median simulation horizontal drift values of 0.24 m and 0.16 m with and without characterization respectively are similar, as are the experimental horizontal drift medians of 0.015 m and 0.054 m with and without characterization respectively. Higher spread between the lower adjacent and upper adjacent values (i.e., non-outlier values) is seen in simulation with Collision Characterization, which is expected for the same reason higher spread is seen for recovery time values with Collision Characterization, as discussed in Section 5.6.5. However, this higher spread is not seen in the experimental results, which are very similar among the CRP variations. While the quadrotor is still recovering, there is horizontal acceleration, which increases the horizontal drift. Therefore, the drift observed in the experiments is lower than in simulation, because of smaller initial collision inclination angles, which require less time to recover. Both the simulation and experimental lower adjacent horizontal drift values are 0 m, which is undesirable, as mentioned above. Future iterations of the CRP should increase the minimum horizontal drift value to at least 0.10 m, to recover the quadrotor a safe distance away from the wall.

Height loss is the difference in quadrotor CM altitude from t_C to the end of recovery, with positive values if the quadrotor CM has fallen, and negative values if it has risen. Distributions of height loss for successful trials within the four validation sets are shown in Figure 5–16. Low height loss magnitudes are desired, to have a small recovery envelope, and to allow for successful recoveries from low-altitude collisions.

The height loss distributions are very similar between the CRP with Collision Characterization and without, for both simulation and experiment. The median height loss values are 0.075 m and 0.079 m for the Monte Carlo simulation with and without Collision Characterization respectively, and the corresponding experimental medians are -0.013 m and -0.010 m

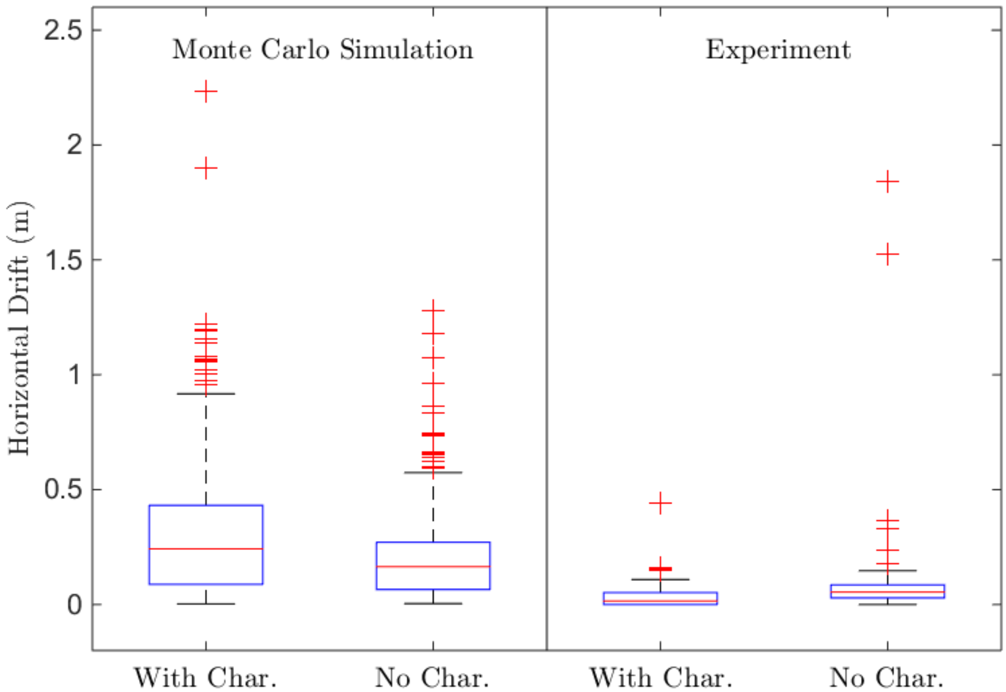

Figure 5–15: Horizontal drift distribution. Distribution is marked according to description for Figure 5–6.

respectively. Similarly to the response time and horizontal drift distributions, the height loss values are much lower in experiment, as the quadrotor loses height with increasing recovery time. Thus, lower recovery times in Figure 5–14 correspond to lower height loss in Figure 5–16. Also, the height loss in experiment was limited to ~ 0.7 m, as beyond this height, the quadrotor would hit the safety net, and the trial would be considered a failed recovery.

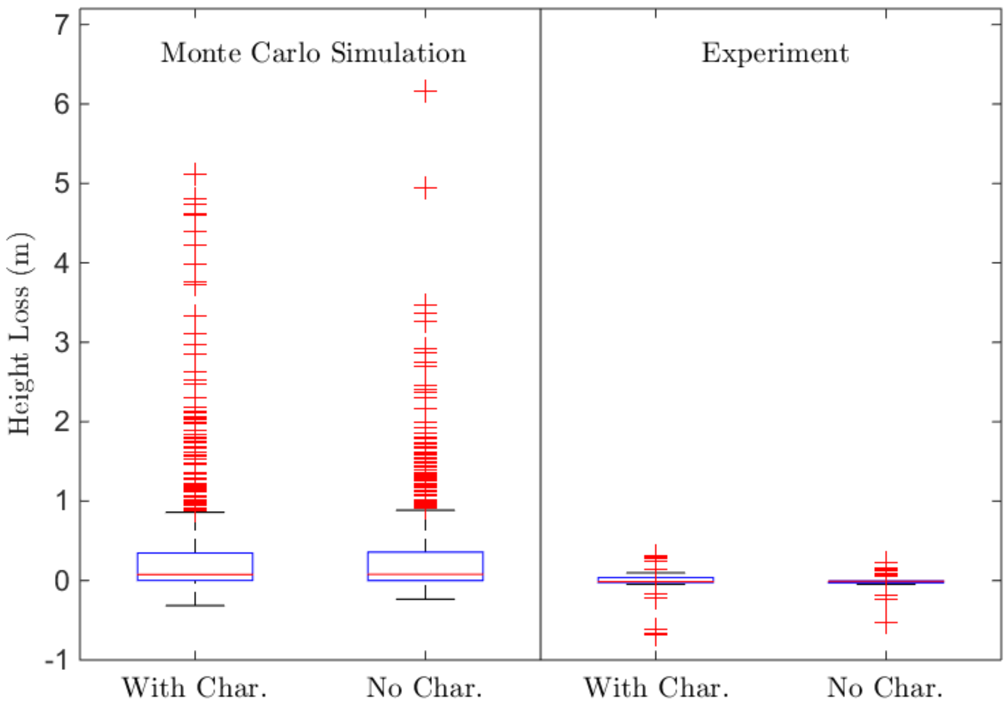

Figure 5–16: Height loss distribution. Distribution is marked according to description for Figure 5–6.

CHAPTER 6
Conclusions

6.1 Summary of Work

Significant strides have be made toward developing a recovery strategy for collisions between a quadrotor with propeller protection and a wall, to regain stable flight-control at a safe distance away from the wall. A model has been developed for a propeller-protected quadrotor that captures its dynamic response due to a non-destructive collision with a stationary, vertical wall. The standard quadrotor dynamics model was augmented with a nonlinear compliant normal contact force model and a classical friction force model variation, using contact geometry derived from representative geometry of the experimental platforms' bumpers.

The model was evaluated in simulation, showing logical responses under different initial collision conditions, and providing confidence in the ability of the simulator to be a tool for collision recovery. From the array of simulations, an in depth study of collision response has been performed that can be used in future recovery control work. From the results of this study, the general collision response was classified into five categories: Away Big, Away Small, Level, Toward Small, and Toward Big. The analysis also identified potential indicators of quadrotor response if no recovery control is present, for use in a collision recovery strategy.

The model was then validated by comparing the response of experimental collisions without recovery, to their simulated reconstructions. This was done for two experimental platforms. Good qualitative (visual) correspondence was seen for at least 0.3 s after first contact for the seven experiments with viable data using the Spiri quadrotor. The duration of qualitative correspondence for the 22 experiments using the Navi quadrotor was on average ten times greater than the first bumper contact duration captured by a top-view high-speed camera. These correspondence durations are well beyond the necessary time needed for the simulator to be a suitable tool for collision recovery — this time measured between the collision beginning to recovery control engaging.

Using the findings of the simulated and experimental vehicle responses to collisions, an overall control strategy was developed: the Collision Recovery Pipeline, comprising of the Collision Identification, Collision Characterization, and Re-orientation Control phases. The Collision Identification phase was developed to detect the collision and estimate the wall normal. A Monte Carlo simulation shows the median detection time is 4.1 ms, and 50% of the wall normal estimations are within $\pm 12°$ of the actual wall normal. The Collision Characterization phase generates four indicators of collision response, which are used in a Fuzzy Logic Process to compute the *Collision Response Intensity.* The FLP parameters were presented, specific to collision recovery for the Navi quadrotor, and parameters that must be tuned for other platforms were specified. The Collision Characterization phase was verified with Monte Carlo simulation and experiment, showing more intense rotational response for higher CRI absolute values.

The full CRP using the two phases presented in this thesis, and the Re-orientation Control phase by Dicker [47] has been experimentally validated to successfully recover the Navi quadrotor from initial collision inclinations in the range $-15° < \zeta < 20°$, velocities from 0.8 m/s to 3.0 m/s, and headings $\psi = \{0°,\ 45°\}$. In over 93 experimental trials, there was no damage to the electronics, but four of Navi's bumpers were damaged. As the bumpers were able to protect the propellers for a majority of the trials without damage, and the core vehicle components remained functional, the notion of a 'non-destructive' collision is valid. The experimental validations for both the contact dynamics model and the CRP show that bumper design is integral to maintaining functionality of all four thrusters. To match the CRP experimental performance to that seen in Monte Carlo simulation, bumpers that do not allow the propellers to contact the wall at inclinations greater than 30° are needed.

While the Collision Identification phase is necessary for engaging the CRP, using the Collision Characterization phase, and CRI-to-$\mathbf{a}_{ref}$ mapping from [47] does not have a discernible effect on the Navi quadrotor recovery control performance, specifically, the initial collision conditions that allow for successful recovery, or height loss. The phase also has no effect on median recovery times or horizontal drift, but does result in higher distribution of these values when used.

The failed experimental recoveries using the CRP show the collision recovery strategy does not address the full scope of collisions between those that are trivial to recover from, and those that damage the quadrotor, which was one of the objectives in Section 1.3. However, the observations on collision response from this thesis, and the demonstration of successful recovery for less extreme collisions provides an excellent basis for furthering recovery control to address all current collision recovery objectives.

6.2 Recommendation for Future Work

To increase the contact dynamics model accuracy, additional phenomena can be incorporated. The non-linear effect of air speed variations on the vehicle dynamics can be captured by the aerodynamic effects: the free stream velocity and angle of attack with respect to the free stream affect the total thrust [14]. Another aerodynamic effect is known as 'blade flapping', where the different inflow velocities experienced by the propeller blades deflect the thrust vector, creating additional roll and pitch moments [14]. Just as quadrotor thrust is affected by the ground effect when the propellers are in close proximity to the ground [13], it is similarly influenced by the propeller proximity to the wall. As collisions occur right beside the wall, a 'wall effect' can be added to the model. Lastly, the bumper deflections transverse to the bumper plane that were observed in experiment can be modelled as well.

The Collision Identification phase of the CRP can be improved by addressing the issue of inexact wall normal estimation described in Section 5.2.2. By improving the estimation of $\mathbf{e}_N$, the quadrotor will recover more directly away from the wall.

The utility of the Collision Characterization phase can be expanded beyond what was demonstrated in this thesis. This phase in conjunction with a different CRI-to-$\mathbf{a}_{ref}$ mapping than presented in (5.9) will be necessary to increase the minimum horizontal drift value from 0 m to at least 0.10 m. This would recover the quadrotor a greater and safer distance away from the wall, a task which the CRP without Collision Characterization cannot achieve. The CRI output of the Collision Characterization could also be used to predict if the collision damaged the bumpers, warranting a return-to-home or landing command after successful recovery.

The collision recovery strategy needs to demonstrate successful recovery for all collisions that do not damage the quadrotor. This will require modifying the bumper design to remove any possibility of recovery failure due to the propellers hitting the wall/bumper. After removing this physical impediment, the CRI-to-$\mathbf{a}_{ref}$ mapping can be further investigated to study the effect of the Collision Characterization phase on recovery response. Expanding the CRP to address all non-destructive collisions may also require modifying the overall collision strategy itself.

After addressing all the objectives from this thesis, the recovery problem scope can be expanded to include quadrotor collisions with solid obstacles of different geometry and smoothness (e.g., poles, tree trunks, windows), and eventually deformable obstacles as well (e.g., wires, tree branches). The recovery controller can also be augmented to detect motor/propeller failure, and adapt to these changes. Lastly, demonstration of the robust collision recovery strategy on other propeller protected platforms will show the algorithm is general, and can be implemented on any quadrotor with bumpers.

Appendix A —
Full Contact Dynamics Model Experimental Validation Results using Navi quadrotor

Impact Conditions and Response Comparison between Navi Experiments and Simulations

Trial	Initial Conditions			Experiment			Simulation			Qualitative Correspondence Duration (s)
	ζ (°) ± 1.0	$\dot{X}_C$ (m/s) ± 0.05	ψ (°) ± 1.0	Response Category	δ_{init} (m)	1st Contact Duration (s)	Response Category	δ_{init} (m)	1st Contact Duration (s)	
N-1	-6.5	1.3	9.2	TS	0.0155	0.048	TS	0.0258	0.074	0.4
N-2	-5.4	1.3	11	TS	0.0182	0.050	TS	0.0263	0.076	0.4
N-3	-5.0	1.3	9.2	TS	0.0158	0.048	TS	0.0263	0.075	0.4
N-4	-5.9	1.3	16	TS	0.0156	0.046	TS	0.0288	0.084	0.4
N-5	-0.2	0.9	12	TS	0.0072	0.050	TS	0.0190	0.081	0.2
N-6	-1.7	1.5	14	TS	0.0271	0.052	TS	0.0384	0.089	0.5
N-7	-2.7	1.5	8.9	TS	0.0157	0.046	TS	0.0344	0.082	0.4
N-8	4.4	1.4	21	TS	0.0241	0.058	TS	0.0359	0.090	0.6
N-9	0.4	1.5	16	TS	0.0244	0.054	TS	0.0371	0.092	0.5
N-10	5.2	1.5	15	TS	0.0229	0.056	TS	0.0403	0.092	0.4
N-11	5.1	1.5	13	TS	0.0242	0.054	TS	0.0409	0.095	0.5
N-12	5.6	1.5	8.8	TS	0.0218	0.054	TS	0.0386	0.085	0.5
N-13	4.2	1.7	9.9	TS	0.0272	0.056	TS	0.0427	0.088	0.5
N-14	7.3	1.6	8.2	TS	0.0307	0.056	TS	0.0404	0.085	0.6
N-15	8.8	1.6	5.7	TS	0.0250	0.052	TS	0.0373	0.081	0.4
N-16	5.8	1.7	9.2	TS	0.0320	0.054	TS	0.0434	0.088	0.6
N-17	8.4	1.6	5.5	TS	0.0287	0.052	TS	0.0373	0.076	0.9
N-18	6.8	1.5	4.8	TS	0.0282	0.054	TS	0.0355	0.076	0.3
N-19	4.5	1.4	15	TS	0.0274	0.058	TS	0.0356	0.090	0.5
N-20	4.8	1.4	10	TS	0.0252	0.056	TS	0.0356	0.090	0.3
N-21	6.8	1.4	11	TS	0.0269	0.056	TS	0.0357	0.091	0.2
N-22	10.7	1.3	0.5	TS	0.0137	0.032	TS	0.0271	0.070	0.2

REFERENCES

[1] M. Meeker, "Kleiner perkins caufield byers internet trends 2015." `http://www.kpcb.com/blog/2015-internet-trends`, 2015. Accessed: 2016-11-14.

[2] P. AS, "Parrot ar.drone 2.0 gps edition." `https://www.parrot.com/ca/drones/parrot-ardrone-20-gps-edition`. Accessed: 2016-11-14.

[3] Amazon.ca, "Udi rc u818a." `https://www.amazon.ca/UDI-RC-U818A-2-4GHz-Quadcopter/dp/B00D3IN11Q`. Accessed: 2016-11-14.

[4] D. Mellinger, N. Michael, and V. Kumar, "Trajectory generation and control for precise aggressive maneuvers with quadrotors," *Int. J. of Robotics Research*, vol. 31, no. 5, pp. 664–674, 2012.

[5] D. Mellinger and V. Kumar, "Minimum snap trajectory generation and control for quadrotors," in *IEEE Int. Conf. on Robotics & Automation (ICRA)*, (Shanghai, China), pp. 2520–2525, May 2011.

[6] M. Faessler, F. Fontana, C. Forster, and D. Scaramuzza, "Automatic re-initialization and failure recovery for aggressive flight with a monocular vision-based quadrotor," in *IEEE Int. Conf. on Robotics & Automation (ICRA)*, (Seattle, Washington, United States), May 2015.

[7] Federal Aviation Administration, "Fact sheet – small unmanned aircraft regulations (part 107)." `https://www.faa.gov/news/fact_sheets/news_story.cfm?newsId=20516`, June 2016. Accessed: 2016-11-14.

[8] European Aviation Safety Agency, "Introduction of a regulatory framework for the operation of drones." `https://www.easa.europa.eu/system/files/dfu/A-NPA%202015-10.pdf`, July 2015. Accessed: 2016-11-14.

[9] G. Olivares, "Uas airborne collision severity evaluation," tech. rep., Federal Aviation Administration Alliance for System Safety of UAS through Research Excellence, July 2015.

[10] European Aviation Safety Agency, "Drone collision task force final report." `https://www.easa.europa.eu/system/files/dfu/TF%20Drone%20Collision_Report%20for%20Publication%20%28005%29.pdf`, April 2016. Accessed: 2016-11-14.

[11] B. Erginer and E. Altuğ, "Modeling and pd control of a quadrotor vtol vehicle," in *IEEE Intelligent Vehicles Symp.*, (Istanbul, Turkey), pp. 894–899, June 2007.

[12] F. Tauro, C. Pagano, P. Phamduy, S. Grimaldi, and M. Porfiri, "Large-scale particle image velocimetry from an unmanned aerial vehicle," *IEEE/ASME Transactions on Mechatronics*, vol. 20, no. 6, pp. 3269–3275, 2015.

[13] S. Bouabdallah and R. Siegwart, "Full control of a quadrotor," in *IEEE/RSJ Int. Conf. on Intelligent Robots & Systems (IROS)*, (San Diego, California, United States), pp. 153–158, Oct 2007.

[14] G. M. Hoffmann, H. Huang, S. L. Waslander, and C. J. Tomlin, "Quadrotor helicopter flight dynamics and control: Theory and experiment," in *AIAA Guidance, Navigation, & Control Conf.*, vol. 2, (Hilton Head, South Carolina, United States), Aug 2007.

[15] T. Lee, M. Leoky, and N. H. McClamroch, "Geometric tracking control of a quadrotor uav on se (3)," in *49th IEEE conference on decision and control (CDC)*, (Atlanta, Georgia, United States), pp. 5420–5425, Dec 2010.

[16] "Px4 autopilot." `http://px4.io`. Accessed: 2016-11-15.

[17] "Ardupilot." `http://ardupilot.org`. Accessed: 2016-11-15.

[18] H. Bouadi, M. Bouchoucha, and M. Tadjine, "Sliding mode control based on backstepping approach for an uav type-quadrotor," *World Academy of Science, Engineering and Technology*, vol. 26, no. 5, pp. 22–27, 2007.

[19] L. Gentili, R. Naldi, and L. Marconi, "Modeling and control of vtol uavs interacting with the environment," in *47th IEEE Conf. on Decision & Control (CDC)*, (Cancun, Mexico), pp. 1231–1236, Dec 2008.

[20] L. Marconi, R. Naldi, and L. Gentili, "Modelling and control of a flying robot interacting with the environment," *Automatica*, vol. 47, no. 12, pp. 2571–2583, 2011.

[21] K. Alexis, G. Darivianakis, M. Burri, and R. Siegwart, "Aerial robotic contact-based inspection: planning and control," *Autonomous Robots*, vol. 40, no. 4, pp. 631–655, 2015.

[22] T. Tomić and S. Haddadin, "A unified framework for external wrench estimation, interaction control and collision reflexes for flying robots," in *IEEE/RSJ Int. Conf. on Intelligent Robots and Systems (IROS)*, (Chicago, Illinois, United States), pp. 4197–4204, Sept 2014.

[23] G. Gilardi and I. Sharf, "Literature survey of contact dynamics modelling," *Mechanism & Machine theory*, vol. 37, no. 10, pp. 1213–1239, 2002.

[24] K. Hunt and F. Crossley, "Coefficient of restitution interpreted as damping in vibroimpact," *J. of Appl. Mechanics*, vol. 42, no. 2, pp. 440–445, 1975.

[25] Y. Zhang and I. Sharf, "Compliant force modelling for impact analysis," in *ASME Int. Design Engineering Tech. Conf. & Computers & Information in Engineering Conf.*, (Salt Lake City, Utah, United States), pp. 595–601, Sept 2004.

[26] R. Herbert and D. McWhannell, "Shape and frequency composition of pulses from an impact pair," *J. of Manufacturing Sci. & Eng.*, vol. 99, no. 3, pp. 513–518, 1977.

[27] B. Armstrong-Hélouvry, P. Dupont, and C. C. De Wit, "A survey of models, analysis tools and compensation methods for the control of machines with friction," *Automatica*, vol. 30, no. 7, pp. 1083–1138, 1994.

[28] H. Olsson, K. J. Åström, C. C. De Wit, M. Gäfvert, and P. Lischinsky, "Friction models and friction compensation," *European J. of Control*, vol. 4, no. 3, pp. 176–195, 1998.

[29] A. Lin, "Friction identification from robotic insertion tasks," Master's thesis, University of Victoria, 2001.

[30] A. K. Silverman and R. R. Neptune, "Three-dimensional knee joint contact forces during walking in unilateral transtibial amputees," *J. of Biomechanics*, vol. 47, no. 11, pp. 2556–2562, 2014.

[31] R. Pàmies-Vilà, J. M. Font-Llagunes, U. Lugrís, and J. Cuadrado, "Parameter identification method for a three-dimensional foot–ground contact model," *Mechanism & Machine Theory*, vol. 75, pp. 107–116, 2014.

[32] L. Manin, M.-A. Andrianoely, G. Ferraris, R. Dufour, and T. Nouri-Baranger, "Nonlinear dynamic interactions between a cable and its casing. application to automotive gearshift command systems," in *Int. Conf. on Noise & Vibration Engineering*, (Leuven, Belgium), Sept 2014.

[33] P. Fietkau, A. Baumann, and B. Bertsche, "Transient ehl gear contact simulation," in *FISITA 2012 World Automotive Congr.*, (Beijing, China), pp. 107–118, Nov 2013.

[34] M. Nikolic, B. Borovac, and M. Rakovic, "Simulation of foot-ground contact for bipedal robots," in *IEEE Int. Conf. on Robotics in Alpe-Adria-Danube Region (RAAD)*, (Smolenice Castle, Slovakia), pp. 1–6, Sept 2014.

[35] Y. Huang, P. Soueres, and J. Li, "Contact dynamics of massage compliant robotic arm and its coupled stability," in *IEEE Int. Conf. on Robotics & Automation (ICRA)*, (Hong Kong, China), pp. 1499–1504, May 2014.

[36] L. A. Zadeh, "Fuzzy sets," *Information and Control*, vol. 8, no. 3, pp. 338–353, 1965.

[37] E. H. Mamdani and S. Assilian, "An experiment in linguistic synthesis with a fuzzy logic controller," *Int. J. of man-machine studies*, vol. 7, no. 1, pp. 1–13, 1975.

[38] C.-C. Lee, "Fuzzy logic in control systems: fuzzy logic controller. ii," *IEEE Trans. on Systems, Man, and Cybernetics*, vol. 20, no. 2, pp. 419–435, 1990.

[39] N. N. Karnik and J. M. Mendel, "Introduction to type-2 fuzzy logic systems," in *1998 IEEE Int. Conf. on Fuzzy Systems*, vol. 2, (Anchorage, Alaska, United States), pp. 915–920, May 1998.

[40] G. Chen and T. T. Pham, *Introduction to fuzzy sets, fuzzy logic, and fuzzy control systems*. CRC press, 2000.

[41] M. Sugeno, "An introductory survey of fuzzy control," *Information sciences*, vol. 36, no. 1, pp. 59–83, 1985.

[42] C. M. Lim and T. Hiyama, "Application of fuzzy logic control to a manipulator," *IEEE Trans. on Robotics and Automation*, vol. 7, no. 5, pp. 688–691, 1991.

[43] T. Das and I. N. Kar, "Design and implementation of an adaptive fuzzy logic-based controller for wheeled mobile robots," *IEEE Trans. on Control Systems Technology*, vol. 14, no. 3, pp. 501–510, 2006.

[44] B. Erginer and E. Altuğ, "Design and implementation of a hybrid fuzzy logic controller for a quadrotor vtol vehicle," *Int. J. of Control, Automation and Systems*, vol. 10, no. 1, pp. 61–70, 2012.

[45] M. Santos, V. Lopez, and F. Morata, "Intelligent fuzzy controller of a quadrotor," in *Int. Conf. on Intelligent Systems and Knowledge Engineering (ISKE)*, (Hangzhou, China), pp. 141–146, Nov 2010.

[46] C. Coza and C. Macnab, "A new robust adaptive-fuzzy control method applied to quadrotor helicopter stabilization," in *NAFIPS Annual Meeting of the North American Fuzzy Information Processing Society*, (Montreal, Canada), pp. 454–458, June 2006.

[47] G. Dicker, "Quadrotor reorientation control for collision recovery," Master's thesis, McGill University, 2016.

[48] P. R. Inc., "Spiri 360°." `http://pleiades.ca/rotate`. Accessed: 2015-08-26.

[49] P. R. Dahl, "A solid friction model," tech. rep., DTIC Document, 1968.

[50] D. Karnopp, "Computer simulation of stick-slip friction in mechanical dynamic systems," *Journal of dynamic systems, measurement, and control*, vol. 107, no. 1, pp. 100–103, 1985.

[51] M. Zhang, A. Harmat, and I. Sharf, "Autonomous flight of a quadrotor using multi-camera visual slam," in *Int. Conf. on Intelligent Unmanned Systems*, vol. 10, (Montreal, Canada), Sept 2014.

[52] K. Alexis, C. Huerzeler, and R. Siegwart, "Hybrid modeling and control of a coaxial unmanned rotorcraft interacting with its environment through contact," in *IEEE Int. Conf. on Robotics & Automation (ICRA)*, (Karlsruhe, Germany), pp. 5417–5424, May 2013.

[53] L. Meier, D. Honegger, and M. Pollefeys, "Px4: A node-based multithreaded open source robotics framework for deeply embedded platforms," in *IEEE Int. Conf. on Robotics & Automation (ICRA)*, (Seattle, Washington, United States), pp. 6235–6240, May 2015.

[54] G. Dicker, F. Chui, and I. Sharf, "Quadrotor collision characterization and recovery control." Submitted to *2017 IEEE Int. Conf. on Robotics & Automation (ICRA).*